On Dynamic and Stability Analysis of the Nonlinear Vehicle Models Using the Concept of Lyapunov Stability

by

Sobhan Sadri

A thesis submitted to
The Faculty of Graduate Studies of
The University of Manitoba
in partial fulfillment of the requirements
of the degree of

Doctor of Philosophy

Department of Mechanical Engineering
The University of Manitoba
Winnipeg, Manitoba, Canada
August 2015

August 27, 2015

This thesis is dedicated to my lovely wife, Navin, and my family.

Thesis advisor

Christine Q. Wu

Author

Sobhan Sadri

On Dynamic and Stability Analysis of the Nonlinear Vehicle Models Using the Concept of Lyapunov Stability

Abstract

The "on-road untripped rollover" is a dangerous accident, which kills thousands of vehicle occupants every year. This type of rollover accident occurs in high-speed emergency maneuvers without hitting any external objects. In fact, in this incident, the vehicle is driven through the edges or beyond its yaw and roll stability limits. Therefore, by analyzing the Lyapunov stability of accurate vehicle models, there will be a chance to prevent this type of incidents. The problem is that accurate models have complex dynamics and include nonlinear terms, which make the stability analysis difficult. On the other hand, the available theoretical approaches for nonlinear stability analysis are either not constructive or not effective.

The aim of this thesis is four-fold: a) to define a new measure of dynamics called "modified Lyapunov exponents" to provide more insight into stability analysis of nonlinear systems, b) to introduce the concept of Lyapunov exponents as a constructive method for stability analysis of nonlinear vehicle models, c) to develop a proper nonlinear vehicle roll model in sense of Lyapunov stability analysis, and d) to develop a Scale Experimental Test Vehicle (SETV) with unique features as a vehicle test bed for rollover experiments.

New modified Lyapunov exponents can measure the exponential convergent/divergent rate of the perturbation vector in a specific direction driven by the dynamics in the same direction. Their existence and invariant property are mathematically proven and their indications are discussed.

The concept of Lyapunov exponents has been applied effectively to analyze the system and structure stability of a nonlinear two degrees of freedom (2-DOF) bicycle vehicle model and further to estimate its Lyapunov stability regions.

In the absence of a proper nonlinear vehicle model for Lyapunov stability analysis, a new nonlinear 4-DOF vehicle roll model is developed that can predict the roll motion of a conventional full vehicle model, however, it has simpler dynamics. The Lyapunov stability of the model has been analyzed by Lyapunov linearization and Lyapunov exponents methods. Moreover, the accuracy of the model in predicting the roll behaviour of a real vehicle is justified by experiments on the SETV.

Acknowledgments

I would like to begin by thanking my supervisor Dr. Wu for her support and enthusiasm towards my research. She always gives me confidence and inspiration. I also want to use this opportunity and thank my internal committee members, Dr. Telichev and Dr. Sherif. I had the advantage of their comments, which helped me a lot during this research. I would like to thanks my external examiner Dr. B. Minaker from the University of Windsor for his comments that improved my work.

I want to thank NSERC, MITACS Canada, and Motor Coach Industries for providing in part the funding for this study. Great thanks to the Faculty of Graduate Studies in University of Manitoba for offering me the IGSS, IGSES, and UMGF scholarships.

I would like to thank Paul White, and Rhyse Maryniuk, who contributed to build the experimental setup for this research. I also want to thank all the people who have supported me along the way.

I sincerely appreciate the government of Canada for giving me the opportunity to continue my study in great Canada.

Finally, thanks to my family for their emotional and financial support during all these tough years living overseas.

Contents

List of Tables

List of Figures

Nomenclature

α	tire sideslip angle
β	family of subsets (measure theory)
β	vehicle side slip angle (bicycle vehicle model)
$\boldsymbol{\psi}$	state transient matrix
δ	road wheel steer angle (steering angle)
δ_f	front tire steer angle
$\delta\mathbf{x_i}$	i-th ellipsoidal principal axis
$\lambda^{(i)}$	i-th one-dimensional Lyapunov exponent
λ_{Su}	modified Lyapunov exponent along u direction
$\mathbb{R}^m$	M-dimensional Euclidean state space
$\mathbf{\Gamma}$	closed orbit
EP	stable fixed point

$\mathbf{f}$	vector function
$\mathbf{P}$	projection matrix
$\mathbf{x}$	state vector
$\mathbf{x}_e$	equilibrium point
μ	coefficient of the friction
μ	measure (measure theory)
ω	angular velocity of the wheel rotation (14-DOF model)
ω_f	angular velocity of the front wheel (bicycle vehicle model)
$\omega_x/\ \omega_y/\ \omega_z$	roll rate/ pitch rate/ yaw rate of CG in the body-fixed coordinate
ϕ	roll angle
ψ	yaw angle
ρ	probability measure
ρ_a	density of air
τ	step size
θ	pitch angle
a	distance of CG from front axle (14-DOF model)
A_f	frontal area of the vehicle

a_y lateral acceleration of CG in coordinate frame (X, Y, Z) (4-DOF model)

B stiffness factor

b distance of CG from rear axle (14-DOF model)

b_s suspension damping coefficient

C shape factor

c track width

C_α cornering stiffness

C_d aerodynamic drag coefficient

D peak factor

E curvature factor

F_{tf}/F_{tr} tractive forces in front and rear tires (bicycle vehicle model)

$F_{x'g}/\ F_{y'g}/\ F_{z'g}$ longitudinal/ lateral/ vertical forces at tire contact patch in the $(x',\ y'\ z')$ coordinate (14-DOF model)

$F_{x't}/\ F_{y't}/\ F_{z't}$ tire longitudinal/ lateral/ vertical forces in the $(x',\ y'\ z')$ coordinate (14-DOF model)

$F_{xgs}/\ F_{ygs}/\ F_{zgs}$ longitudinal/ lateral/ vertical forces at tire contact patch in the body-fixed coordinate (14-DOF model)

$F_{xs}/\ F_{ys}/\ F_{zs}$ longitudinal/ lateral/ vertical forces transferred to the body in the body-fixed coordinate

F_y tire lateral force (bicycle vehicle model)

F_{Zr}/F_{Yr} vertical/lateral forces at tire contact patch in coordinate frame (X, Y, Z) (4-DOF model)

h CG height

h_{cf} front roll centre distance below sprung mass CG

h_{cr} rear roll centre distance below sprung mass CG

I_z vehicle moment of inertia about the z-axis (bicycle vehicle model)

J_t tire/wheel rotational inertia (14-DOF model)

J_w wheel rotational inertia (bicycle vehicle model)

J_x roll inertia

J_y pitch inertia

J_z yaw inertia

k_s suspension spring stiffness

k_t tire stiffness

l_f/l_r distance of the CG from the front/rear axles (bicycle vehicle model)

l_{si} initial length of the strut

l_s instantaneous length of the strut

m total mass (bicycle vehicle model)

m vehicle sprung mass (14-DOF model)

m_s sprung mass (4-DOF model)

m_u unsprung mass

M_x/ M_y/ M_z longitudinal/ lateral/ vertical moments transmitted to the sprung mass

N normal load

n_s Steering ratio

r yaw rate (bicycle vehicle model)

r instantaneous tire radius (4-DOF and 14-DOF models)

r_0 nominal radius of tire

s tire longitudinal skid

S_h horizontal shift

S_v vertical shift

T_f applied torque to the front wheel (bicycle vehicle model)

v_t velocity of CG in body-fixed coordinate (bicycle vehicle model)

$v_{x'g}$/ $v_{y'g}$/ $v_{z'g}$ longitudinal/ lateral/ vertical velocities at tire contact patch in the (x', y' z') coordinate (14-DOF model)

v_{xs}/ v_{ys}/ v_{zs} longitudinal/ lateral/ vertical velocities at the suspension corner in the body-fixed coordinate

v_{xu}/ v_{yu}/ v_{zu} unsprung mass longitudinal/ lateral/ vertical velocities in the body-fixed coordinate

v_x/ v_y/ v_z longitudinal/ lateral/ vertical velocities of CG in the body-fixed coordinate

v_{Zur} unsprung vertical velocity on the right hand side of the vehicle in coordinate frame (X, Y, Z) (4-DOF model)

W_s sprung mass weight (4-DOF model)

W_{ur} unsprung mass weight on the right side of the vehicle (4-DOF model)

x_{si} initial suspension spring deflection

x_s suspension spring deflection

x_{ti} initial tire spring deflection

x_t tire spring deflection

RC roll centre

Chapter 1

Introduction

Vehicle safety is one important issue followed by the road traffic safety administrations around the world. According to the National Highway Traffic Safety Administration of the USA (NHTSA), rollover is one of the most dangerous accidents that jeopardizes vehicle occupant lives [1]. The NHTSA statistics, given in Figure 1.1, show that occupant fatalities of rollover crashes increase from 22% of all types of accidents in passenger cars to 61% in Sport Utility Vehicles (SUV) [2]. One type of rollover that happens due to vehicle manoeuvres is known as the "on-road untripped rollover". Although this type of rollover is a small part of all rollover accidents (less than 10%), much attention is given to this problem by NHTSA [3]. The reason is that this type of rollover is caused by vehicle-related factors and it can be prevented by enforcing better vehicle safety standards.

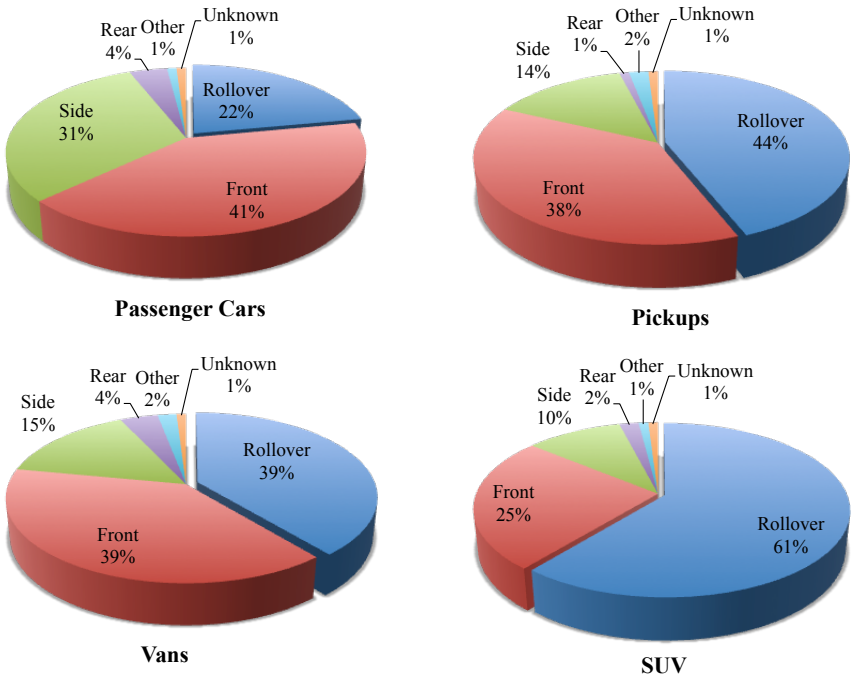

Figure 1.1: Occupant fatalities by type of crash in different type of vehicles

To satisfy those standards, vehicle manufactures strive to improve the dynamic behaviour of their products. They perform different tests in controlled situations to collect information in order to improve their products before sending them to the competitive market. Since those tests are expensive and formidable, it is desirable to analyze the vehicle behaviour theoretically before any tests. It helps reduce the cost by cutting the unnecessary tests.

Literature shows that nonlinear vehicle models are adequate for studies of vehicle dynamics. The untripped on-road rollover can occur due to both roll and yaw instability. Hence, knowing the stability boundaries, in which the vehicle's roll and yaw motions are stable, is quite important.

Different techniques are available for stability analysis of nonlinear systems; however, they suffer from applicability or reliably or both. Therefore, constructive and reliable techniques to find the stability properties of nonlinear vehicle models are in demand.

This thesis targets the deficiency and difficulty of nonlinear stability analysis and its application in the vehicle area, and it has four objectives as follows:

The first objective of this thesis is to suggest the concept of Lyapunov exponents to the vehicle society as a powerful tool for stability analysis of vehicle models, since this concept is advantageous in two cases: a) available methods for computation of the Lyapunov exponents are constructive and do not depend on the size or shape of dynamic equations, and b) Lyapunov exponents benefit from the invariant property, which means their values do not depend on the selected initial conditions for the same basin of attraction. The effectiveness of the concept of Lyapunov exponents is investigated by employing the concept in both structure and system Lyapunov stability analysis of vehicle models representing yaw and roll motions.

In spite of the advantages of the concept of Lyapunov exponents, there are some limitations. For example, Lyapunov exponents are not associated with any specific directions, and the computational load for calculating the exponents of large dynamic systems is high.

The second objective of this thesis is to modify the Lyapunov exponents, which can characterize the exponential divergent or convergent rates of the nonlinear dynamics in specific directions and evolved by the dynamics in the same directions. The modified Lyapunov exponents are not only defined, but also their existence and invariance properties are proven mathematically. The proposed modified Lyapunov exponent

can provide additional insights of nonlinear dynamics compared to those from standard Lyapunov exponents. For example, it can identify the dominant sub-systems, which has the potential impact of reducing the computational load in calculation of the Lyapunov exponents [4].

Developing a proper nonlinear 4-DOF roll vehicle model for Lyapunov stability analysis without losing realistic behaviour is the third objective for this thesis. Unfortunately, available realistic models are large and full of complex dynamics that make them inappropriate for Lyapunov stability analysis. Therefore, considering the lack of a proper model, a nonlinear 4-DOF roll vehicle model is developed by simplifying a common nonlinear 14-DOF full vehicle [5] that can predict the roll motion of the original model precisely. This model is derived as minimum realization to make the Lyapunov stability analysis feasible. Moreover, this model can predict the roll motion, and the occurrence of tire lift-off by measuring only the lateral acceleration. This advantage makes it more suitable for real-world applications.

Finally, the fourth objective of this thesis is to develop a SETV as an automatic/user control vehicle with unique features suitable for rollover study. The goal for developing the SETV is to equip an off-the-shelf scale vehicle with sensors to use as a safe and economical test bed to verify the correlation between theoretical and real-world behaviour in roll motion studies. The SETV is the first scale vehicle test bed at the University of Manitoba, and it is designed and built by a team of three students.

This thesis contributes in the area of nonlinear dynamics analysis by developing the concept of the modified Lyapunov exponent. The contributions of this thesis in the vehicle dynamics area include: a) introducing the concept of Lyapunov exponents to

the vehicle dynamics field as a powerful tool for nonlinear Lyapunov stability analysis, b) developing a proper roll vehicle model for Lyapunov stability analysis with accurate prediction of the roll motion, and c) prototyping a unique scale experimental test vehicle for rollover study.

The evolved publications from this thesis are listed below.

Journals:

[1]. S. Sadri and C. Wu. Lyapunov stability analysis of a new nonlinear 4-DOF vehicle roll model. Manuscript submitted for publication, 2015.

[2]. S. Sadri and C.Q. Wu. Modified Lyapunov exponent, new measure of dynamics. Nonlinear Dynamics, 78(4):2731-2750, 2014.

[3]. S. Sadri and C. Wu. Stability analysis of a nonlinear vehicle model in plane motion using the concept of Lyapunov exponents. Vehicle System Dynamics, 51(6):906-924, 2013.

Conferences:

[1]. P. White, R. Maryniuk, S. Sadri, and C.Q. Wu. Scale experimental test vehicle for rollover study. In 25th Canadian Congress of Applied Mechanics, 2015.

[2]. S. Sadri and C.Q. Wu. Lateral stability analysis of on-road vehicles using Lyapunov's direct method. In Intelligent Vehicles Symposium (IV), 2012 IEEE, pages 821-826, June 2012.

[3]. S. Sadri and C.Q. Wu. Lateral stability analysis of on-road vehicles using the concept of Lyapunov exponents. In Intelligent Vehicles Symposium (IV), 2012 IEEE, pages 450-455, June 2012.

[4]. S. Sadri and C.Q. Wu. Largest Lyapunov exponent as a new indicator to investigate the effects of driving conditions on the vehicle stability properties. In CSME International Congress, CSME, 2012.

The remaining chapters are organized as follows. The theoretical preliminary of this thesis is given in Chapter 3. In Chapter 4, the concept of modified Lyapunov exponents is introduced. In Chapter 5, the concept of Lyapunov exponents is employed to investigate the system and structure stability of the disturbed bicycle vehicle model. Then, in Chapter 6 the nonlinear 4-DOF roll vehicle model is introduced, and the building process of the SETV is discussed. Finally, the thesis conclusions and possible future work are included in Chapter 7.

Chapter 2

Background

2.1 Overview

In this chapter, the previous related works are organized in four sections. The chapter starts by the overview of vehicle dynamics in Section 2.2, and is followed by a literature review about employing a scale vehicle for vehicle dynamic test bed in Section 2.3. In Section 2.4, the concept of Lyapunov stability analysis is reviewed and finally in Section 2.5, the works on Lyapunov stability analysis of vehicle models are reviewed.

2.2 Overview of Vehicle Dynamics

In order to understand vehicle dynamics and its stability problem, it is necessary to introduce the fundamental approach to modelling a vehicle. A vehicle consists of many components distributed within its entire volume. However, to make the

analysis feasible, all components are moved to a few units. The number of adequate units depends on the application. In many cases, all components are represented as one lumped mass (point mass) located at the Centre of Gravity (CG) of the vehicle. In more advanced studies (e.g., ride analysis) it is more accurate to consider the wheels as separate lumped masses. In this case, the lumped masses representing the wheels are called the *unsprung masses* and the lumped mass at the CG (representing the remaining components) is named the *sprung mass*.

The vehicle motions are defined with respect a coordinate system that originates at the CG (sprung mass) and moves with the vehicle (body fixed coordinate). In Figure 2.1, a body fixed coordinate is shown. As it can be seen, the x-axis of the body fixed coordinate system points forward. By the Society of Automotive Engineers (SAE) convention, the y-axis points to the right side of the vehicle while in the International Standard Organization (ISO) 8855, it points to the driver's left side. The z direction obeys the right-hand rule. In this thesis, both standards are used wherever appropriate. Vehicle motions are described by the velocities of the sprung mass with respect to the body fixed coordinate, including: longitudinal, lateral, and vertical translational velocities, and roll, pitch, and yaw angular velocities. However, these velocities are referenced to the earth fixed coordinate system (inertial coordinate system) (see Figure 2.1). The relationship of the body fixed coordinate system to the inertial coordinate system is defined by Euler angles (Cardan angles).

When a driver steers the vehicle to follow a curve shape path, the tires will slip laterally as they roll and develop lateral forces (cornering/sideslip forces). The yaw motion of the vehicle is generated as the result of these lateral forces. In Figure

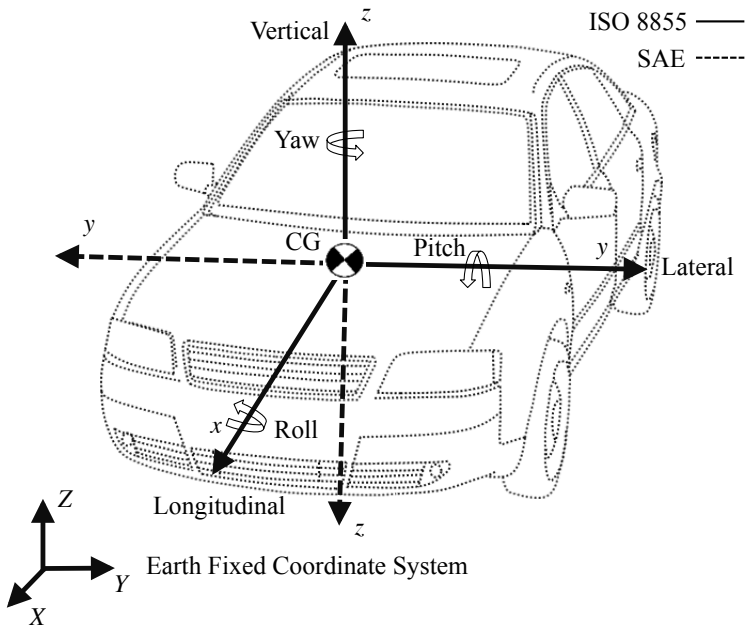

Figure 2.1: ISO and SAE vehicle axis systems

2.2, different behaviour of vehicles in cornering maneuvers are shown. As it can be seen, the vehicle response is one of the following: a) *neutral steer*, where the lateral acceleration of the CG causes identical slip in front and rear tires, b) *understeer*, where the front tires slip more than the rear tires, and c) *oversteer*, where the rear tires slip more than the front tires.

To make the investigation of the yaw motion (lateral dynamics) simpler, the left and right tires of the front and rear axles are concentrated at the centre line along the x-axis. In this way, the model is known as the *bicycle vehicle model* (single-track) [6].

The roll motion of the vehicle results from the interaction of forces acting on and within the vehicle. Both the vehicle parameters and road conditions are involved in roll dynamics. In some very aggressive maneuvers, the roll angle along the longitu-

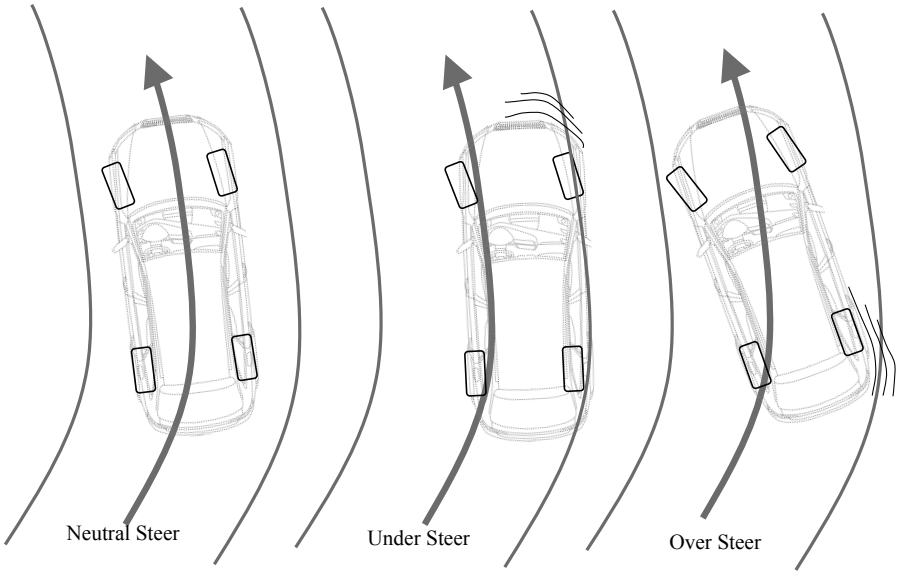

Figure 2.2: Different cornering behaviour of vehicles

dinal axis of the vehicle exceeds 90 degrees, and the side body contacts the ground. This situation is known as *rollover* [7]. Depending on the sources, the rollovers can be classified in two types; a) tripped rollover, and b) untripped rollover [8]. In tripped rollovers, high tripping forces are applied to the tires that cause the vehicle to rollover. This type of rollover mostly happens when the vehicle leaves the road and hits the guardrail or curb, or slides sideways and digs its tires into soft soil. Another possible tripped rollover occurs in off-road environments, for example, in downhill driving. On the other hand, in untripped rollover, there is no object that applies forces to the tires, and rollover happens due to high centrifugal force (internal force), for example, as the result of high-speed collision avoidance maneuvers.

To study vehicle roll motion, researchers employ the available vehicle models [7, 9–12] or develop their own models [5, 13–17]. Depending on the consideration of the roll

acceleration, these models can be classified into two groups [7]: a) those representing quasi-static roll motion [7, 12] and b) those including transient roll motion [5, 9, 11, 13–17]. Choosing a model depends on the applications. For example, in vehicle ride comfort analysis, a vehicle model that includes the relative roll motion of the sprung mass with respect to the unsprung mass is adequate [6]. In the case of developing rollover warning or control systems, a model which is able to detect tire lift-off is highly demanded. Existing models with this property can be classified into two types: a) those that can simulate vehicle roll behaviour up to the tire lift-off [12–15, 17] and b) those that simulate the roll motion even after the tire lift-off occurs [5, 16, 18]. Tire lift-off is unacceptable behaviour; however, all tire lift-off maneuvers do not terminate by rollover crash. Moreover, sometimes it is possible to regain roll stability even after tire lift-off occurs [18]. This fact makes models from the second group more interesting. The nonlinear 14-DOF full vehicle model in [5, 18] is an appropriate for roll motion study even after tire lift-off occurs, but it has a large set of complex dynamic equations, which makes it inappropriate for stability analysis. The model in [16] considers two different models for before and after tire lift-off occurrence. However, the corresponding model for after tire lift-off occurrence, does not model the suspension. Therefore, the need for a proper realistic model for Lyapunov stability analysis that can predict roll motion even after tire lift-off occurs leads to the proposed nonlinear 4-DOF vehicle roll model.

2.3 Overview of Scale Test Vehicles

Research on vehicle roll dynamics and driver assistant systems is required, but conducting research on a full-size vehicle is expensive and potentially dangerous. Moreover, the number of facilities that perform rollover tests on full-size vehicles is limited. Fortunately, literature demonstrates that scale-model testing is a suitable alternative for full-size testing [19]. Furthermore, there are some advantages for testing scale vehicles rather than full-size ones. For example, scale size vehicles are more durable and their maintenance is cheaper. Additionally, testing on a scale vehicle is more repeatable and less dangerous.

There is other research interested in using scale vehicles as experimental test beds. Sampei, et al. [20] used an articulated scale vehicle to examine a proposed path tracking control. Naoki, et al. [21] developed a four-wheel steering and four-wheel drive laboratory scale model vehicle as an experimental setup for testing their controller. Brennan and Alleyne presented the Illinois Roadway Simulator (IRS) in [22] as a scaled test bed to study vehicle dynamics and control. O'Brien, et al. [23] developed the Scale-Model Testing Apparatus, the simplified IRS, as a platform for their vehicle control projects. Travis, et al. [24] employed a scale vehicle in their study on rollover propensity. Verma, et al. [25] developed a scale vehicle to capture the longitudinal and powertrain dynamics of a full-size high-mobility multipurpose wheeled vehicle. Phanomchoeng and Rajamani used a $1/8^{th}$ scale vehicle in [26] to evaluate a newly proposed rollover index. Considering the necessity of the experimental tests for verification theoretical results, the unique SETV has been built in this research to verify the roll motion study of the nonlinear 4-DOF vehicle roll model.

2.4 Overview of Stability Analysis

The nonlinear analysis of vehicle models is important because of a number of reasons. First, theoretical study is always a low-cost way for exploring vehicle behaviour. Second, theoretical study makes it possible to avoid blind simulations and misunderstanding. This advantage becomes more important knowing that nonlinear models can exhibit changing behaviour that depends on the initial conditions. Thirdly, the theoretical analysis provides a basis for designing controllers, and sometimes it can also suggest directions for modifying them [27].

Stability analysis is one of the central tools for nonlinear analysis of dynamical systems. There are different kinds of stability problems. The stability analysis conducted in this thesis emphasizes Lyapunov's method (Lyapunov stability). To understand the concept of Lyapunov stability, consider the two cones shown in Figure 2.3. In Figure 2.3.a, the blue cone is resting on its bottom while the red cone is balanced on its tip. Then, both cones are identically disturbed as shown in Figure 2.3.b. From Figure 2.3.c, it can be seen that the blue cone returned to its previous position and the red cone fell down. Therefore, one can say that the blue cone was in a stable equilibrium while the red cone was in an unstable equilibrium. It is worth mentioning that instability of equilibrium is typically undesirable since it often leads to damage to the involved mechanical or electrical components. Stability analysis can be categorized into two groups: the system stability and the structural stability. In the system stability analysis, the disturbance is imposed to the initial states, and the stability of the solutions of the dynamic systems is discussed. For example, in the case of a vehicle model, the system stability analysis indicates whether the vehicle model returns to

its stable fixed point when its initial states are disturbed. Also, this type of stability analysis can determine the stability region in the state space where the stability of the dynamic system is guaranteed. For example, the ranges of the disturbed states in which the vehicle model is still stable. This type of stability analysis makes it possible to investigate how vehicle model parameters or driving conditions affect the shape and size of the lateral stability region corresponding to the vehicle model. On the other hand, the structural stability analysis investigates the perturbations to the system structure. It determines in which range of parameters the system is stable. Applying the structural stability analysis to a vehicle model, one can define the ranges of the vehicle parameters or driving conditions in which the vehicle remains stable.

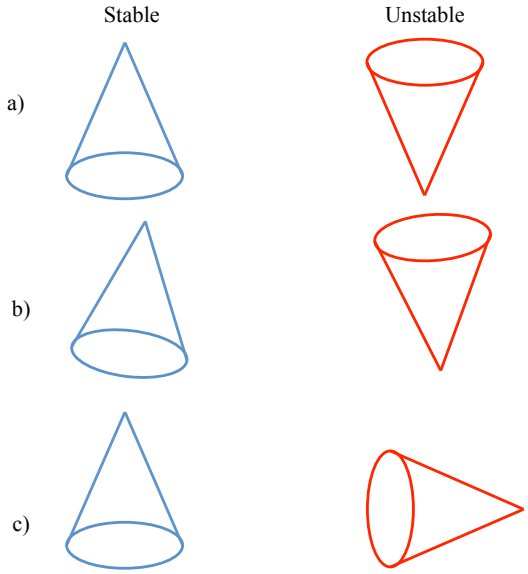

Figure 2.3: Demonstration of the concept of Lyapunov stability

Lyapunov, a Russian mathematician and engineer, formulated this concept as Lyapunov stability: "An equilibrium point is stable if all solutions starting at nearby points stay nearby; otherwise, it is unstable" [28]. His theory includes two meth-

ods: the so-called linearization method and the direct method [27]. The linearization method uses linear approximation around the system equilibriums and provides information about system stability as far as system states are close to equilibrium points. The direct method is not limited to local stability investigation. This method, instead of explicitly solving the dynamic system of equations, determines the stability based on shrinking of a constructed scalar "energy-like" function known as a Lyapunov function [27]. However, the difficulty in finding a Lyapunov function for complex systems is the main restriction to applying this powerful method for stability analysis.

A more constructive technique for stability analysis is the concept of Lyapunov exponents. Lyapunov exponents are *invariant measures* of a dynamic system; that is, they are independent of the initial conditions [29]. They are defined as the average exponential rates of converging or diverging of nearby orbits in the state space [30, 31]. The concept of Lyapunov exponents was first introduced by Lyapunov to study the stability of non-stationary solutions of ordinary differential equations [32]. It is a powerful tool to categorize the steady-state behaviour of dynamic systems. The method for calculating the Lyapunov exponents is constructive for any dynamic systems. This constructive nature makes it more advantageous over Lyapunov's direct method. The Lyapunov exponents of a dynamic system can be calculated numerically using either the system mathematical model or a time series. Some methods for calculating Lyapunov exponents based on a mathematical model have already been developed [30, 33]. Although Lyapunov exponents have mainly been used for diagnosing chaotic systems, there are studies that used them for the stability analysis of nonlinear systems. For example, Wu et al. [34] proved the system stability of their

developed feedback control law for an inverted pendulum system by its Lyapunov exponents. Sekhavat et al. [35] analyzed the stability of hydraulic actuators with an impact controller using the concept of Lyapunov exponents. Some other work in this area has been reviewed in [32].

In spite of the advantages of the concept of Lyapunov exponents, there are several limitations. For examples, although the number of exponents is the same as the dimension of the state space, Lyapunov exponents are not associated with any specific directions. Furthermore, the exponential divergent or convergent rates are dictated by the dynamics in all directions in the state space. In many applications, it is highly desirable to obtain the information about the asymptotic performance in specific directions, and equally important, about the dynamics, which drives such asymptotic behaviours in the specific directions. Such information can be crucial for performance monitoring and control design.

It is not uncommon that dynamic systems can be viewed as consisting of sub-systems, and the dynamic effects of each sub-system on the asymptotic performance of the overall system can be fundamentally different. Thus, identifying the dominant sub-systems, which dictate the asymptotic behaviours, is important. Some research has been conducted on analyzing and regulating the entire system asymptotic behaviours using the sub-systems. Pecora and Carroll [36], for the purpose of synchronization of chaotic systems, divided the dynamic system into two sub-systems, the master subsystem and the slave subsystem. They named the Lyapunov exponents of the slave subsystem as conditional Lyapunov exponents, and claimed that if all Lyapunov exponents of the slave subsystem were negative, then the behaviour of the entire

dynamic system dominated by the master subsystem, and synchronization is possible. Later, Mendes [37] proved that conditional Lyapunov exponents exist. In another independent study, Gonzalez et al. [4] have shown that for certain types of chaotic systems, it is possible to compute the spectrum of Lyapunov exponents approximately by only the portion of the information or the sub systems of the entire dynamic system. The above work is inspiring in terms of diagnosing chaotic systems and chaos control using the dynamics of the sub systems. The methodologies can also contribute to identification of the sub systems, which dominate the asymptotic behaviours of entire nonlinear systems. However, the above research was limited to chaotic systems, and its applications to stable systems are questionable. Furthermore, the sub systems were restricted to be in the same state space, i.e., for some rare chaotic systems, the above research might be able to provide the information about the asymptotic behaviours along certain state axes. In some applications, the asymptotic behaviours in the directions other than the state space axes are needed.

Another limitation of determining Lyapunov exponents is the high computational load for calculating the exponents, which prohibits the applications of the exponents for large dynamic systems. As pointed out in [4], it is possible to compute the spectrum of Lyapunov exponents using the sub systems. Thus, the idea of identifying dominant sub-systems can have potential impact in reducing the computational load for large systems. This idea inspires the concept of modified Lyapunov exponents in this thesis.

2.5 Overview of Lyapunov Stability Analysis of Vehicle Models

The causes of on-road untripped rollover are not well understood; however, some literature suggests that it can occur due to both roll and yaw instability [14]. Roll instability may cause a vehicle to rollover during critical maneuver such as a "J-turn" maneuver at high speeds.

On the other hand, in certain movements such as a sine wave shape maneuver, the vehicle experiences yaw instability that is followed by rollover [14]. Thus, yaw stability in plane motion (lateral stability) is another important factor in vehicle dynamics since it has a strong influence on the overall vehicle safety.

In fact, by improving the lateral stability of the vehicle, it is possible to reduce the risk that a driver loses control of the vehicle [38]. The lateral stability analysis can be carried out using either linear or nonlinear vehicle models. There is a limitation on the information provided by linear models since these models are only valid in the case of maneuvers with low levels of the lateral acceleration. In the case of high-g maneuvers, the tire force saturates, and the linear model is no longer valid [39]. Therefore, for more reliable information, the nonlinearity of the tires must be considered, and the vehicle model must be analyzed as a nonlinear system. Much of the work done in the vehicle stability analysis and control design areas considers a simple nonlinear vehicle model. The main advantage of such a model is the clear relation among vehicle states. In general, for lateral stability analysis, the well-known bicycle vehicle model is adequate. Such a simple nonlinear model makes it possible to follow the effects of

the vehicle states and parameters on the overall vehicle dynamics [38].

A vehicle model as a nonlinear system has its own stability region that its size and shape are indicators of vehicle stability during critical maneuvers [40]. If the states of a vehicle during critical maneuvers still remain in the stable region, it will move towards a stable equilibrium point along the specific trajectory. A few studies to estimate the lateral stability region of a vehicle have been conducted in the literature. Work on finding the roll stability region of the vehicle is even more distinct. Methods applied in these studies can be generally divided into two groups: Lyapunov-function-based methods and non-Lyapunov-function-based methods [40]. Most of the existing studies on the non-Lyapunov-function-based methods rely on topological methods, in which the stability region is estimated due to the number of system trajectories derived by numerical integrations of the system equations, such as the trajectory reversal method proposed by Genesio et al. [41]. Intagaki et al. [42], by plotting a large number of trajectories and using an applicable understanding, approximated the stability boundary. Samsundar and Huston [43] applied the trajectory reversal method to estimate the lateral stability region for a 2-DOF nonlinear vehicle model. Ko and Lee [40] proposed an algorithm, including the trajectory reversal technique, to determine a lateral stability region for a 3-DOF nonlinear vehicle for the case of a constant vehicle speed. The dependence of trajectory-based methods on appropriate selections of the initial conditions is the most important limitation in their application to stability analysis.

On the other hand, investigation of the stability region based on the Lyapunov-function-based method relies on Lyapunov's direct method. For examples, Johnson

and Huston [44] applied this method to the lateral stability analysis of a vehicle in straight-line motion at a constant longitudinal velocity. Samsundar and Huston [43] proposed another quadratic Lyapunov function for the same vehicle model and the parameters in [44] and by using the tangency point technique, found the largest possible lateral stability region associated with their proposed Lyapunov functions. Applying Lyapunov's direct method to investigate the effects of driving conditions on vehicle stability is extremely challenging since there are no constructive techniques to find a Lyapunov function. This technique is also infeasible to demonstrate how the vehicle parameters such as vehicle inertial properties or tire characteristics affect the lateral vehicle stability. The main limitations on applying Lyapunov's direct method to estimate the lateral stability region can be summarized as limitations on the vehicle model due to difficulties in finding a Lyapunov function, and dependence of the size and shape of the stability region on the selected Lyapunov functions.

The effects of vehicle parameters and driving conditions on lateral vehicle stability have been discussed in the literature. The fundamental work on this subject has been done by Pacejka [10]. An excellent review of related studies in this topic can also be found in [45]. Shen et al. [46] proposed the so-called joint-point locus approach to investigate vehicle system handling. This method geometrically determined the equilibria of the system and then their associated stability properties have been discussed based on system trajectories. Ko and Lee [40] by using their proposed topological approach, which is based on the trajectory reversal technique, found that the variation of the driving conditions such as the vehicle velocity, road friction coefficient, and steering input lead to more significant changes in vehicle yaw lateral stability in

comparison with the variation of vehicle parameters such as weight distribution and tire characteristics. As mentioned earlier, in the trajectory-based method, the system trajectories are solved for certain initial conditions. This means that the conclusion of system behaviour for other initial conditions is not guaranteed.

Considering the drawbacks of the Lyapunov's direct method, and non-Lyapunov-function-based methods, a constructive and reliable technique for Lyapunov stability analysis of the vehicle model is crucial. This raises the opportunity to suggest the concept of Lyapunov exponents to the vehicle design community as a powerful stability analysis tool.

Liu et al. [47] investigated the chaotic behaviour of the vehicle/driver system using the concept of Lyapunov exponents. To the best of the author's knowledge, this concept has not been applied in vehicle stability analysis yet. However, the previous success of using this concept in other areas [32, 34, 35] promises its effectiveness in the vehicle stability analysis.

Chapter 3

Theoretical Preliminary

3.1 Overview

The theoretical preliminary of this thesis is divided into two parts. In the first part, stability theory, basic definitions, and stability related analysis tools are presented, and in the second part, the vehicle models are discussed.

The first part is organized as follows. In Section 3.2.1, the theory of Lyapunov stability is presented. The concept of Lyapunov exponents is introduced in Section 3.2.2. In Section 3.2.3, the standard algorithm for calculating the spectrum of Lyapunov exponents is discussed. Section 3.2.4 presents some basic definitions on measure theory. Finally, in Section 3.2.5, the multiplicity ergodic theorem of Oseledec is given.

The second part covers the following topics. In Section 3.3.1, tire models including: the linear, third order polynomial, and Magic Formula are introduced. The bicycle

vehicle model is discussed in Section 3.3.2. In Section 3.3.3, the 14-DOF full vehicle model is presented.

3.2 Stability Theory

3.2.1 Lyapunov Stability

To understand the theory of Lyapunov stability, it is necessary to define the equilibrium point (fixed point). Suppose an autonomous (time-invariant) nonlinear dynamic system is represented by a set of nonlinear equations in the form of

$$\dot{\mathbf{x}} = \mathbf{f}(\mathbf{x}) \tag{3.1}$$

where $\mathbf{f}$ is a $m \times 1$ vector function, and $\mathbf{x}$ is the $m \times 1$ state vector. The number of states, m, is called the order of system (dimension of the system).

Equilibrium point [27]: A state $\mathbf{x}_e$ is an equilibrium point of the system if once $\mathbf{x}(t)$ is equal to $\mathbf{x}_e$, it remains equal to $\mathbf{x}_e$ for all future time. Mathematically, in this definition $\mathbf{x}_e$ satisfies

$$\mathbf{f}(\mathbf{x}_e) = \mathbf{0} \tag{3.2}$$

Now suppose that above equilibrium $\mathbf{x}_e$ is transferred to the origin $\mathbf{0}$. The definition of the stability in the sense of Lyapunov is:

Lyapunov stable [27]: The equilibrium point $\mathbf{x} = \mathbf{0}$ is said to be stable if, for any $R > 0$, there exist $r > 0$, such that if $\|\mathbf{x}(0)\| < r$, then $\|\mathbf{x}(t)\| < R$ for all $t \geq 0$. Otherwise, the equilibrium point is unstable.

This definition can be written as

$$\forall R > 0,\ \exists r > 0,\ \|\mathbf{x}(0)\| < r \Rightarrow\ \forall t \geq 0,\ \|\mathbf{x}(t)\| < R$$

The geometrical demonstration of the Lyapunov stability is given in Figure3.1. It can be seen that the stability of an equilibrium point can be marginal or asymptotical. These two types of stability can be distinguished by following definition:

Asymptotic stablility [27]: An equilibirum point $\mathbf{0}$ is asymptotically stable if it is stable, and if in addition there exists some $r > 0$ such that $\|\mathbf{x}(0)\|$ implies that $\mathbf{x} \to \mathbf{0}$ as $t \to \infty$.

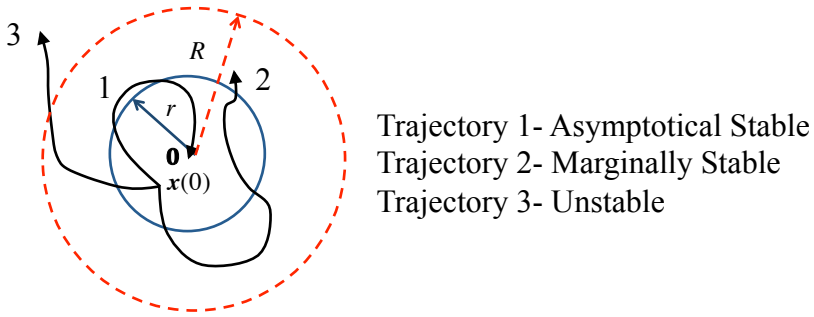

Figure 3.1: Concept of Lyapunov stability

Another type of Lyapunov stability is exponentially stable, in which the state vectors converge to the equilibrium point faster than an exponential function. The concept of exponentially stability can be defined as:

Exponential stability [27]: An equilibrium point $\mathbf{0}$ is exponentially stable if there exist two strictly positive numbers α and λ such that $\forall t > 0,\ \|\mathbf{x}(0)\| \leq \alpha\|\mathbf{x}(0)\|e^{-\lambda t}$ is some ball $\mathbf{B}_r$ around the origin.

Finally, the domain of attraction is defined as:

Domain of attraction [27]: The domain of attraction of the equilibrium point is the largest set of all points such that the trajectories initiated at these points finally converge to the equilibrium point.

3.2.2 Lyapunov Exponents

The concept of Lyapunov exponents has been introduced to identify the asymptotic behaviour of nonlinear systems. Considering a continuous dynamic system in an m-dimensional state space, this concept monitors the long-term evolution of an infinitesimal m-sphere of initial conditions. Due to the dynamic flow, the m-sphere may deform to an m-ellipsoid as graphically shown in Figure 3.2 when $m = 2$. The average exponential rates of the length expanding or contracting of the ellipsoid principal axes over an infinite time period are called Lyapunov exponents [30]. The i-th one-dimensional Lyapunov exponent, $\lambda^{(i)}$, can be calculated as

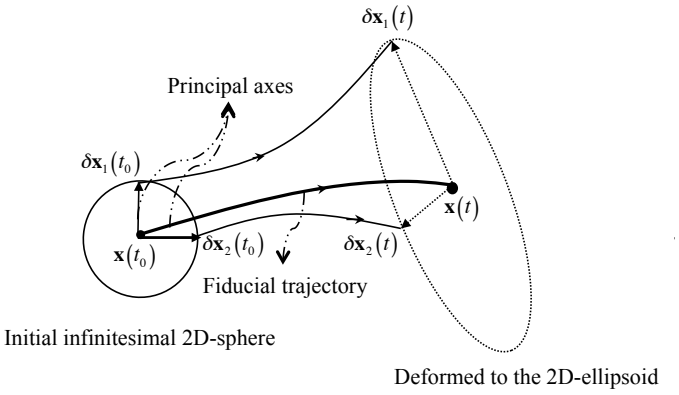

Figure 3.2: Evolution of an infinitesimal two-dimensional (2D) sphere of initial conditions

$$\lambda^{(i)} = \lim_{t\to\infty} \frac{1}{t} \ln \frac{\|\delta \mathbf{x}_i(t)\|}{\|\delta \mathbf{x}_i(0)\|}, \quad i = 1, \cdots, m \tag{3.3}$$

where $\|\delta \mathbf{x_i}(t)\|$ is the length of the i-th ellipsoidal principal axis at time t.

The existence of the limit in the above definition is guaranteed by Oseledec's multiplicative ergodic theorem [29]. Although in the calculation of Lyapunov exponents choosing a trajectory (the "fiducial" trajectory) is needed, the consequence of a theorem of Oseledec [29] proves that Lyapunov exponents are global properties of dynamic systems and are independent of the chosen trajectory ("invariant measure" of the dynamic system) if the probability measure ρ is ergodic[1]. Since for each principal axis one Lyapunov exponent can be defined, the total number of system Lyapunov exponents is equal to the dimension of the state space of the dynamic system. It is important to note that the orientation of the ellipsoid changes continuously as it evolves. Therefore, it is not possible to define the direction associated with a given exponent. Both the signs and the values of a system Lyapunov exponent have information about its exponential behaviour.

The signs of Lyapunov exponents reveal the stability property of the system's dynamics. Negative exponents correspond to those principal axes of the ellipsoid that shrink in average. If all the exponents are negative, the dynamic system is exponentially stable and the attractor is a fixed point (equilibrium point). Zero exponents indicate the slow change in magnitudes of principal axes. A system with one zero exponent while others are negative has a one-dimensional attractor. For systems with order three or more, the positive Lyapunov exponents indicate a chaotic behaviour. In a

[1] see Section 3.2.5

chaotic system, the long-term behaviour of an initial condition that is specified with any uncertainty cannot be predicted [30].

The sum of all Lyapunov exponents indicates the time averaging divergence of the phase space volume. Therefore, for any dissipative dynamic systems, the sum of all exponents is negative [30]. This implies that dissipative systems have at least one negative exponent. Moreover, dissipative systems with no fixed point must have at least one zero exponent [48].

In general, there is no feasible analytical way to determine the Lyapunov exponents for a complicated system [49]. Therefore, the Lyapunov exponents are often calculated numerically. They can be calculated using either the system mathematical model or a time series. In practical applications, the finite-time Lyapunov exponents are frequently used in the following form

$$\lambda^{(i)} = \frac{1}{t} \ln \frac{\|\delta \mathbf{x}_i(t)\|}{\|\delta \mathbf{x}_i(0)\|}, \quad i = 1, \cdots, m \tag{3.4}$$

in the limit as $t \to \infty$, the finite-time Lyapunov exponents converge to the true Lyapunov exponents [50].

Lyapunov Exponents in System of Differential Equations

Consider the system that its time evolution is described by a set of continuous differential equations in M-dimensional Euclidean state space $\mathbb{R}^m$ as

$$\dot{\mathbf{x}} = \mathbf{f}(\mathbf{x}) \tag{3.5}$$

where $\mathbf{f}$ is a smooth $m \times 1$ nonlinear vector function and $\mathbf{x}$ is a $m \times 1$ state vector.

Let the $\mathbf{T}^t_{\mathbf{x}(0)}$ be the solution of the initial condition $\mathbf{x}(0)$ at time t

$$\mathbf{x}(t) = \mathbf{T}^t_{\mathbf{x}(0)} \tag{3.6}$$

therefore, $\mathbf{T}^t$ is a smooth nonlinear flow that gives the evolution of all points in the phase space at time t.

The time evolution of the perturbation vector, $\delta\mathbf{x}$, which is defined in the tangent space, can be extracted by the following linear differential equation

$$\delta\dot{\mathbf{x}} = \mathbf{J}(\mathbf{x})\,\delta\mathbf{x} \tag{3.7}$$

where $\mathbf{J}(\mathbf{x})$ is the Jacobian matrix calculated at the point $\mathbf{x}(t)$

$$\mathbf{J}(\mathbf{x}) = \frac{\partial \mathbf{f}}{\partial \mathbf{x}^{\mathrm{T}}}(\mathbf{x}) \tag{3.8}$$

The evolution of the perturbation vector at time t can be found by the map $d\mathbf{T}^t_{\mathbf{x}(0)}$ (fundamental matrix) which is the linear part of the nonlinear map $\mathbf{T}^t_{\mathbf{x}(0)}$ [51].

$$\delta\mathbf{x} = d\mathbf{T}^t_{\mathbf{x}(0)}\delta\mathbf{x}(0) \tag{3.9}$$

This linear map obeys the following chain rule

$$d\mathbf{T}^{t+s}_{\mathbf{x}(0)} = d\mathbf{T}^t_{\mathbf{T}^s_{\mathbf{x}(0)}}\, d\mathbf{T}^s_{\mathbf{x}(0)} \tag{3.10}$$

Suppose that m perturbation vectors are defined, $\delta\mathbf{x}_i(0)$ for $i = 1, \cdots, m$, along the principal axes of an infinitesimal volume of initial conditions, m-dimensional sphere, around the orbit $\mathbf{x}(0)$. Then the Lyapunov exponents can be defined in terms of the length of these principal axes as

$$\lambda^{(i)} = \lim_{t\to\infty} \frac{1}{t} \ln \frac{\|\delta \mathbf{x_i}(t)\|}{\|\delta \mathbf{x_i}(0)\|}, \quad i = 1, \cdots, m \tag{3.11}$$

where $\|\delta \mathbf{x_i}(t)\|$ represents the length of the ith principal axis of the traversed initial infinitesimal volume at time t.

The $\lambda^{(i)}$, $i = 1, \cdots, m$, are called the spectrum of Lyapunov exponents for the nonlinear system in Eq. 3.5. In fact, as mentioned before, the Lyapunov exponents indicate the long-term behaviour of a dynamic system by monitoring the evolution of the initially arbitrarily infinitesimal volume element. Figure 3.3 illustrates this concept for the case of the 2-dimensional system.

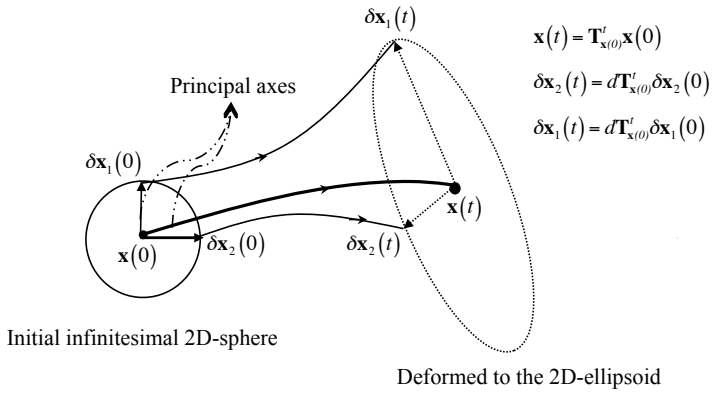

Figure 3.3: Concept of Lyapunov exponents in a 2D- state space

The length changes of most perturbation vectors[2], $\delta \mathbf{x}(0)$ in the tangent space after sufficient long time can be found by [52]

$$\|\delta \mathbf{x}(t)\| \approx e^{\lambda^{(1)} t} \|\delta \mathbf{x}(0)\| \tag{3.12}$$

where $\lambda^{(1)}$ is the largest Lyapunov exponent of the nonlinear system in Eq. 3.5. The

[2]As long as $\delta \mathbf{x}(0) \notin V^{(2)}_{\mathbf{x}(0)}$ (see Section 3.2.5)

area spanned by the first two principal axes changes as $e^{\left(\lambda^{(1)}+\lambda^{(2)}\right)t}$, and the volume spanned by the first three principal axes changes as $e^{\left(\lambda^{(1)}+\lambda^{(2)}+\lambda^{(3)}\right)t}$, and so on.

The existences of the Lyapunov exponents, limits in Eq. 3.11, are guaranteed by the multiplicative ergodic theorem of Oseledec [29]. Moreover, under a condition (see Section 3.2.5) , Lyapunov exponents are independent of the selected initial condition, and they will have constant values for all initial points inside the same basin of attraction.

Lyapunov Exponents in System of Difference Equations

It is possible to discretize the differential equation given in 3.5 as

$$\mathbf{x}\left[n+1\right] = \mathbf{f}\left[\mathbf{x}\left[n\right]\right] \tag{3.13}$$

where $\mathbf{f} : \mathbb{R}^m \rightarrow \mathbb{R}^m$ is a differentiable vector function. The difference equation, governing the discrete-time evolution of the perturbation vector, is

$$\delta\mathbf{x}\left[n+1\right] = \mathbf{J}\left[\mathbf{x}\left[n\right]\right]\delta\mathbf{x}\left[n\right] \tag{3.14}$$

where $\mathbf{J}\left[\mathbf{x}\left[n\right]\right]$ is the Jacobian matrix of the nonlinear vector function $\mathbf{f}$ calculated for the point $\mathbf{x}\left[n\right]$.

$$\mathbf{J}\left[\mathbf{x}\left[n\right]\right] = \left.\frac{\partial\mathbf{f}}{\partial\mathbf{x}^{\mathrm{T}}}\right|_{\mathbf{x}=\mathbf{x}[n]} \tag{3.15}$$

The Lyapunov exponents for the difference equation of Eq. 3.13 are defined by

$$\lambda^{(i)} = \lim_{n\rightarrow\infty}\frac{1}{n}\ln\frac{\left\|\delta\mathbf{x}_i\left[n\right]\right\|}{\left\|\delta\mathbf{x}_i\left[0\right]\right\|} \quad where \;\; i = 1,\cdots,m \tag{3.16}$$

After some manipulations, the limit in Eq. 3.16 can be express as

$$\lambda^{(i)} = \lim_{n\rightarrow+\infty}\frac{1}{n}\sum_{m=1}^{n}\ln\frac{\left\|\delta\mathbf{x}_i\left[m\right]\right\|}{\left\|\delta\mathbf{x}_i\left[m-1\right]\right\|} \quad where \;\; i = 1,\cdots,m \tag{3.17}$$

3.2.3 Standard Algorithm to Calculate Lyapunov Exponents

The standard algorithm [53] calculates all Lyapunov exponents (spectrum of the Lyapunov Exponents) of a system defined in the form of a mathematical model. This algorithm starts by selecting an arbitrary initial condition for the nonlinear differential equations given in Eq. 3.5.

The initial m-sphere principal axes are constructed on the selected initial condition. The evolution of the initial condition known as the 'fiducial' trajectory can be found by the action of nonlinear Eq. 3.7. To find the evolution of principal axes, another set of equations given in Eq. 3.18 is needed.

$$\delta\dot{\mathbf{x}}_i = \mathbf{J}(\mathbf{x}(t))\,\delta\mathbf{x}_i,\ \ i = 1, \cdots, n \tag{3.18}$$

where $\mathbf{J}(\mathbf{x}(t))$ is defined in Eq. 3.8.

Equation 3.18 can be rewritten in the form of state transient matrix, $\boldsymbol{\psi}$, as

$$\dot{\boldsymbol{\psi}} = \mathbf{J}(\mathbf{x}(t))\,\boldsymbol{\psi} \tag{3.19}$$

where

$$\boldsymbol{\psi} = \begin{bmatrix} \delta\mathbf{x}_1 & \cdots & \delta\mathbf{x}_m \end{bmatrix}_{m\times m} \tag{3.20}$$

To solve Eq. 3.7 and Eq. 3.20 simultaneously, they are represented in one set of equation given as

$$\begin{cases} \dot{\mathbf{x}} = \mathbf{f}(\mathbf{x}(t)) \\ \dot{\boldsymbol{\psi}} = \mathbf{J}(\mathbf{x}(t))\,\boldsymbol{\psi} \end{cases} \tag{3.21}$$

The initial conditions can be any arbitrary initial conditions, as long as they are located on the same basin of attraction. However, in the case of initial principal axes, they must span the infinitesimal volume.

$$\begin{Bmatrix} \mathbf{x}(0) \\ \boldsymbol{\psi}(0) \end{Bmatrix} = \begin{Bmatrix} \mathbf{x}_0 \\ \boldsymbol{\psi}_0 \end{Bmatrix} \tag{3.22}$$

The standard choice for initial principal axes is orthonormal vectors define as $\boldsymbol{e}_1(0) = (1, 0, ..., 0)$, $\boldsymbol{e}_2(0) = (0, 1, 0, ..., 0), ...,$ $\boldsymbol{e}_m(0) = (0, ..., 0, 1)$.

$$\boldsymbol{\psi}_0 = \begin{bmatrix} \boldsymbol{e}_1^T(0) & ... & \boldsymbol{e}_m^T(0) \end{bmatrix}_{m \times m} \tag{3.23}$$

Integrating the nonlinear Eq. 3.21 for the given initial conditions in Eq. 3.22 until a single time step, τ, yields to next set of vectors $\delta\mathbf{x}_1(\tau), \cdots, \delta\mathbf{x}_m(\tau)$.

In numerical calculation of the Lyapunov exponents, there are two main concerns [30]: the divergence of each principal axis, and the singularity due to the collapse of all principal axes along the direction of the most rapidly growth. To solve the above problems, the Gram-Shmidt Reorthonormalization (GSR) technique will be applied in each integration period,τ as

$$\mathbf{v}_1(\tau) = \frac{\delta\mathbf{x}_1(\tau)}{\|\delta\mathbf{x}_1(\tau)\|},\ \mathbf{v}_2(\tau) = \frac{\delta\mathbf{x}_2(\tau) - <\delta\mathbf{x}_2(\tau), \mathbf{v}_1(\tau)>\mathbf{v}_1(\tau)}{\|\delta\mathbf{x}_2(\tau) - <\delta\mathbf{x}_2(\tau), \mathbf{v}_1(\tau)>\mathbf{v}_1(\tau)\|}, \cdots, \tag{3.24}$$

$$\mathbf{v}_m(\tau) = \frac{\delta\mathbf{x}_m(\tau) - <\delta\mathbf{x}_m(\tau), \mathbf{v}_1(\tau)>\mathbf{v}_1(\tau) - \ldots - <\delta\mathbf{x}_m(\tau), \mathbf{v}_{m-1}(\tau)>\mathbf{v}_{m-1}(\tau)}{\|\delta\mathbf{x}_m(\tau) - <\delta\mathbf{x}_m(\tau), \mathbf{v}_1(\tau)>\mathbf{v}_1(\tau) - \ldots - <\delta\mathbf{x}_m(\tau), \mathbf{v}_{m-1}(\tau)>\mathbf{v}_{m-1}(\tau)\|}$$

The main idea behind this scheme, shown in Figure 3.4 for the 2D case, is to find the orthonormalized basis,$\{\mathbf{v}_1, \cdots, \mathbf{v}_m\}$, such that it defines the same subspace which has already defined by $\{\delta\mathbf{x}_1, \cdots, \delta\mathbf{x}_m\}$.

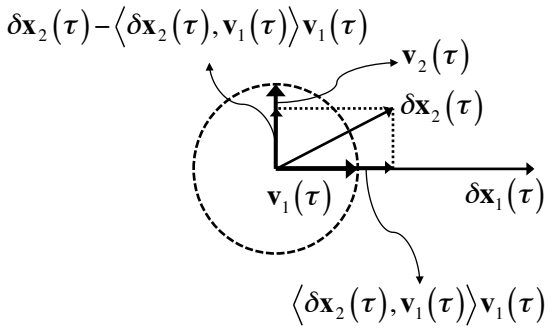

Figure 3.4: Geometrical interpretation of GSA procedure for a 2D case, the component of the second vector along the first vector has been removed

The GSR procedure never changes the direction of the first principal axes, $\delta\mathbf{x}_1$, so this vector is free to seek out the direction of the most rapidly growing in the tangent space [30]. The length of this vector is proportional to $e^{\lambda^{(1)}t}$ for large t. The length of the second vector, which has no component along the direction of the first vector due to the GSR, is proportional to $e^{\lambda^{(2)}t}$ and so on.

3.2.4 Basic Definitions on Measure Theory

To understand the multiplicity ergodic theorem of Oseledec, which will be used in the extension of Lyapunov exponents in Chapter 4, some definitions in Measure Theory

must be given. Those necessary ones have been briefly discussed here; however, interested readers can refer to [54, 55] for more details.

σ-algebra: Let β be a family of subsets of a set X, β is a *σ-algebra* if:

1. ϕ, $X \in \beta$
2. $B \in \beta$ whenever $X \setminus B \in \beta$
3. $\cup_{k=1}^{\infty} B_k \in \beta$ whenever $B_k \in \beta$ for every $k \in \mathbb{N}$

Given a family β of subsets of X, the smallest σ-algebra containing β, that is, the intersection of all σ-algebra containing β, is called the *σ-algebra of X generated by β.*

β-Measurable set: Each element of a σ-algebra β is called a *β-measurable set.*

Borel σ-algebra: Let X be a topological space, and let β be the family of all open subsets of X. The σ-algebra of X generated by β is called the *Borel σ-algebra* of X.

Borel-measurable sets: Elements of a Borel σ-algebra β are called *Borel-measurable sets.*

Measure, μ: Let β be a σ-algebra of X, a function $\mu : \beta \to [0, +\infty]$ is a *measure* in X with respect to β provided that:

1. $\mu(\phi) = 0$

2. If $B_k \in \beta$ for every $k \in \mathbb{N}$ and $B_k \cap B_l = \phi$ whenever $k \neq l$, then

$$\mu\left(\cup_{k=1}^{\infty} B_k\right) = \sum_{k=1}^{\infty} \mu\left(B_k\right) \tag{3.25}$$

Measure space: The triple (X, β, μ) is called a *measure space.*

Probability space: Measure space (X, β, μ) is a *probability space* if $\mu(X) = 1$. In this case μ is called probability measure and denoted by ρ.

β-measurable transformation: Let X be a set and let β be a σ-algebra of X. A transformation $T : X \to X$ is a *β-measurable* if $T^{-1}B \in \beta$, preimage[3]of B under T is in β, whenever $B \in \beta$.

β-measurable function: A function $\varphi : X \to \mathbb{R}$ is said to be β-measurable if $\varphi^{-1}B \in \beta$, preimage of B under φ is in β, whenever B is a Borel-measurable set.

Lebesgue integrable: Given a measure μ in X with respect to β, a β-measurable signed function φ is *Lebesgue integrable* , $\varphi \in L^{-1}(X, \beta, \mu)$, if at least one of $\int_X \varphi^+ \, d\mu$ and $\int_X \varphi^- \, d\mu$ is finite

$$\min\left(\int_X \varphi^+ \, d\mu, \int_X \varphi^- \, d\mu\right) < \infty \tag{3.26}$$

where

$$\varphi^+(x) = \begin{cases} \varphi(x) & \text{if } \varphi(x) > 0 \\ 0 & \text{otherwise} \end{cases} \tag{3.27}$$

[3]Given $f : X \to Y$, for each $y \in Y$, the preimage of y is the set: $f^{-1}(y) = \{x \in X \mid f(x) = y\}$

and

$$\varphi^{-}(x) = \begin{cases} -\varphi(x) & \text{if } \varphi(x) < 0 \\ 0 & \text{otherwise} \end{cases} \tag{3.28}$$

in this case

$$\int_X \varphi \, d\mu = \int_X \varphi^{+} \, d\mu - \int_X \varphi^{-} d\mu \tag{3.29}$$

and one can conclude that φ is μ-integrable if and only if

$$\int_X |\varphi| \; d\mu < \infty \tag{3.30}$$

Measure-preserving transformation: A transformation $T : X \to X$ is *measure-preserving* if it is measurable and if for all measurable sets

$$\mu\left(T^{-1}(B)\right) = \mu(B), \quad \forall B \in \beta. \tag{3.31}$$

It is equivalent to say that the transformation T preserves the measure μ.

Ergodic transformation: The transformation $T : X \to X$ is called *ergodic* if

$$\forall B \in \beta, \; T^{-1}(B) = B \Longrightarrow \mu(B) = 0 \text{ or } 1. \tag{3.32}$$

Invariance: $\rho(\varphi) = \rho(\varphi \circ f)$, where $\varphi : M \to R$ is a continuous function and operator $\circ$ is the Koopman operator [56]. This means that the measure ρ is invariant under time evolution, i.e., invariant under the dynamical system [57].

Ergodicity: An invariant probability measure ρ is ergodic or indecomposable if it does not have a nontrivial convex decomposition:

$$\rho = \alpha\rho_1 + (1 - \alpha)\rho_2 \tag{3.33}$$

where ρ_1 and ρ_2 are again invariant probability measure and $\rho_1 \neq \rho_2$ [58].

3.2.5 The Multiplicity Ergodic Theorem of Oseledec

The multiplicity ergodic theorem of Oseledec is the matrix version of the Birkhoff Ergodic Theorem [59]. It says that for ρ-almost every $\mathbf{x}(0) \in X$, if $\mathbf{f}$ preserves a probability measure ρ, the asymptotic behaviour of $\mathbf{T}^n_{\mathbf{x}[0]}$ is similar to iterating a single linear map [55].

Theorem- (multiplicity ergodic theorem of Oseledec) [29, 52, 57, 58]

Let ρ be a probability measure on a space M, and $\mathbf{f} : M \to M$ a measure preserving map such that ρ is ergodic. Let also $\mathbf{T} : M \to$ the $m \times m$ matrices be a measurable map such that

$$\int_M \log^+ \|\mathbf{T}(\mathbf{x})\| \ \rho(d\mathbf{x}) < \infty^4 \tag{3.34}$$

where $\log^+ u = \max(0, \log u)$.

Define the matrix $\mathbf{T}^n_{\mathbf{x}(0)} = \mathbf{T}(\mathbf{f}^{n-1}(\mathbf{x}(0))) \cdots \mathbf{T}(\mathbf{f}^1(\mathbf{x}(0)))\mathbf{T}(\mathbf{x}(0))$. Then, for ρ-almost all $\mathbf{x}(0)$, the following limit exists:

$$\lim_{n\to\infty} \left(\mathbf{T}^{n*}_{\mathbf{x}(0)} \mathbf{T}^n_{\mathbf{x}(0)}\right)^{\frac{1}{2n}} = \mathbf{\Lambda}_{\mathbf{x}(0)} \tag{3.35}$$

where $*$ denotes the matrix transposition.

The logarithms of the eigenvalues of $\mathbf{\Lambda}_{\mathbf{x}(0)}$ are called characteristic exponents, or Lyapunov exponents. They can be denoted by $\lambda_{1\,\mathbf{x}(0)} \geq \lambda_{2\,\mathbf{x}(0)} \geq \cdots$ or $\lambda^{(1)}_{\mathbf{x}(0)} \geq \lambda^{(2)}_{\mathbf{x}(0)} \geq \cdots$.

They are ρ-almost everywhere constant if ρ is ergodic. Therefore, they are independent of $\mathbf{x}(0)$, and they can be denoted by $\lambda^{(1)} \geq \lambda^{(2)} \geq \cdots$.

[4]The norm of the matrix is the operator norm in Euclidean space (identical in value to the spectral norm) with submultiplicative property $\|\mathbf{AB}\| \leq \|\mathbf{A}\| \|\mathbf{B}\|$

Let $\lambda^{(1)}_{\mathbf{x}(0)} > \lambda^{(2)}_{\mathbf{x}(0)} > \cdots$ be the characteristic exponents again, but no longer repeated by multiplicity ($m^{(i)}$ is called the multiplicity of $\lambda^{(i)}$). Let $E^{(i)}_{\mathbf{x}(0)}$ be the subspace of $\mathbb{R}^m$ corresponding to the eigenvalues $\leq e^{\lambda^{(i)}}$ of $\mathbf{\Lambda}_{\mathbf{x}(0)}$. Then $\mathbb{R}^m = E^{(1)}_{\mathbf{x}(0)} \supset E^{(2)}_{\mathbf{x}(0)} \supset \cdots$ and the following holds

For ρ-almost all $\mathbf{x}\,(0)$

$$\lim_{n\to\infty} \frac{1}{n} \ln \left\| \mathbf{T}^n_{\mathbf{x}(0)} \mathbf{u} \right\| = \lambda^{(i)}_{\mathbf{x}(0)} \quad if \quad \mathbf{u} \in E^{(i)}_{\mathbf{x}(0)} \setminus E^{(i+1)}_{\mathbf{x}(0)}. \tag{3.36}$$

Remark: In particular, for all vectors $\mathbf{u}$ that are not in the subspace $E^{(2)}_{\mathbf{x}(0)}$, the limit in Eq. 3.36 is the largest Lyapunov exponent $\lambda^{(1)}$ [57].

3.3 Vehicle Models

3.3.1 Pneumatic Tire Models

The tire behaviour plays an important role in vehicle dynamics. Under a cornering maneuver, the tire produces lateral force, also known as "cornering force", which results in lateral motion of the vehicle. For low slip angles (less than approx. 5^o), the lateral force produced by a pneumatic tire has a linear relationship with the slip angle α. Therefore, the lateral force can be described as

$$F_y = C_\alpha \alpha \tag{3.37}$$

where C_α is known as "cornering stiffness". In high speed maneuvers, where lateral acceleration is over approx. 0.3 g, the tire slip angle is usually more than 5^o and the above equation is no longer valid.

A more accurate model is the third-order polynomial tire model [43, 44]. In this model, the tire lateral force is related to slip angle as given in Eq. 3.38.

$$F_y = C_\alpha \left(\alpha - k\alpha^3\right) \tag{3.38}$$

where the k parameter is associated with the nonlinear dependence of the lateral force on the sideslip angle [43, 44].

One of the most accurate models of the pneumatic tire is known as the "Magic Formula" [10]. The Magic Formula model is found by an empirical method that fits experimental data to describe the relationship between the cornering force and the slip angle, or the longitudinal force and the longitudinal slip ratio [60]. In general, the Magic Formula is expressed as:

$$f\left(x\right) = \ D \sin \ \{ \ C \ \arctan \left[B \ x \ - \ E \left(B \ x \ - \ \arctan \ Bx\right)\right]\} \tag{3.39}$$

where B is called the stiffness factor, C is the shape factor, D is the peak factor, and E is the curvature factor. The values of these parameters depend on the vertical load on the tire and can be found by experiment. Considering the horizontal shift S_h and vertical shift S_v the cornering force or longitudinal force, $F\left(X\right)$ will be

$$\begin{gathered} F\left(X\right) = \ f\left(x\right) \ + \ S_v \\ \\ x = \ X \ + \ S_h \end{gathered} \tag{3.40}$$

This formula produces a curve as a function of x which is shown in Figure 3.5 In order to find the cornering force, the variable x in the Magic Formula must be replaced by the slip angle α. In this thesis, the nonlinear models (third-order polynomial tire model and Magic Formula) are employed to produce tire lateral forces.

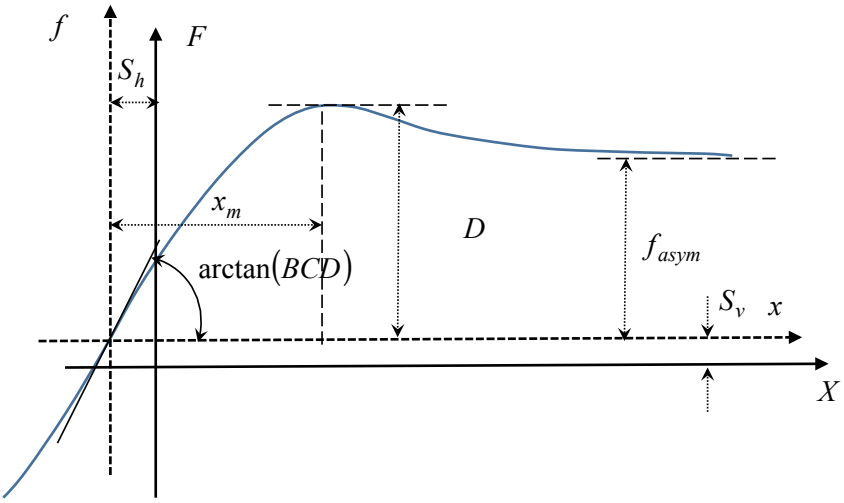

Figure 3.5: Magic Formula

3.3.2 Bicycle Vehicle Model

The $x-y$ plane motion of a vehicle is adequate to model its yaw and lateral motions. The schematic view of the well-known "bicycle vehicle model" [10] that has long been employed for the analysis of the yaw motion is given in Figure 3.6. As it can be seen, the track width has been neglected; this simplification is valid when the radius of the cornering motion is much larger than the width of the vehicle which; it is, in almost all normal operation. This model does not represent the load transfer and body roll; therefore, it is restricted to the cases where the roll moment is small. Small

roll moment is reasonable when the height of centre of gravity is low in comparison to the track width or when the coefficient of the friction between tire and road is small [10].

Three differential equations [61] for the vehicle model in Figure 3.6 using a to the fixed coordinate system on the centre of gravity (CG) of the vehicle can be derived as

$$\begin{cases} \dot{v}_x = \frac{1}{m}\left(2\ F_{tf}\cos\delta_f + 2\ F_{tr} - 2\ F_{yf}\sin\delta_f - \frac{1}{2}C_d A_f \rho_a v_x^2\right) + v_y r \\ \dot{v}_y = \frac{1}{m}\left(2\ F_{tf}\sin\delta_f + 2\ F_{tr} + 2\ F_{yf}\cos\delta_f + 2\ F_{yr}\right) - v_x r \\ \dot{r} = \frac{1}{I_z}\left(2\ l_f F_{tf}\sin\delta_f + 2\ l_f F_{yf}\cos\delta_f - 2\ l_r F_{yr}\right) \end{cases} \tag{3.41}$$

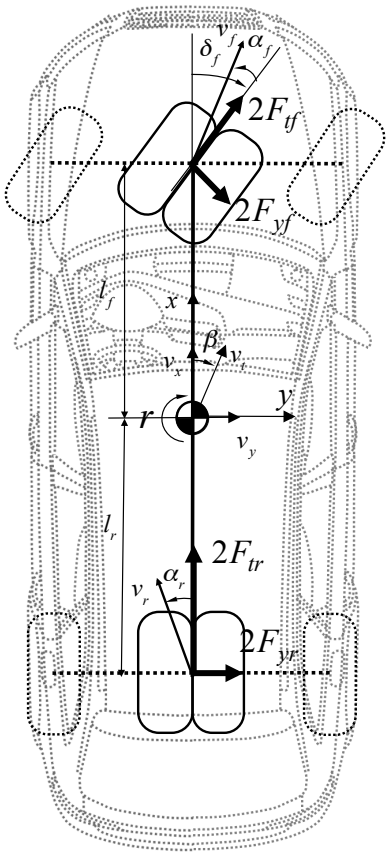

Figure 3.6: Simple vehicle model to study the lateral motions

where m is the total mass of the vehicle, I_z is the vehicle moment of inertia about the z-axis, and l_f and l_r are the distance of the centre of gravity from the front and the rear axles, respectively. The tire lateral forces (side forces) F_{yf} and F_{yr} are for the front and the rear tiers. The front tire steer angle is δ_f. The longitudinal speed (speed of traveling) v_x is of the vehicle and v_y denotes the lateral speed of the vehicle. Finally, r stands for the yaw rate of the vehicle around the z-axis. The last term inside the parenthesis in Eq. 3.41 represents the longitudinal aerodynamic drag forces where C_d is the aerodynamic drag coefficient, A_f is the frontal area of

the vehicle, and finally ρ_a is the density of air. The lateral aerodynamic forces and moments have been neglected, as they are small relative to the tire side forces.

Tractive forces F_{tf} and F_{tr} that are produced by the applied torque to the wheels. The governing equation of motion for the wheels at front axles, shown in Figure 3.7, is

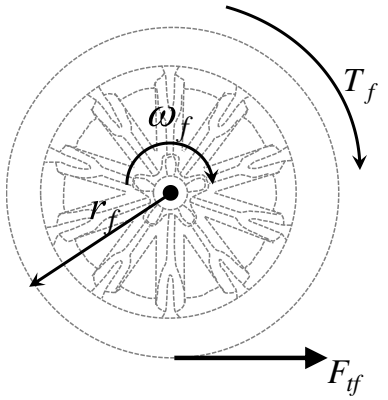

Figure 3.7: Front wheel rotation dynamics

$$\dot{\omega}_f = \frac{1}{J_w}\left(T_f - r_f F_{tf}\right) \tag{3.42}$$

where J_w is the wheel roll inertia. The angular velocity of the front wheel is ω_f. T_f stands for the applied torque to the wheel and it can be produced by the powertrain or the braking system. A similar equation can be written for each rear wheel. To neglect the dynamics of the traction forces, it is always assumed that the vehicle is driven with a constant longitudinal velocity. Moreover, for simplicity, the drag force is also neglected. Therefore, Eq. 3.41 is reduced to

$$\begin{cases} \dot{v}_y = \frac{1}{m}\left(2\ F_{yf}\cos\delta_f + 2\ F_{yr}\right) - v_x r \\ \\ \dot{r} = \frac{1}{I_z}\left(2\ l_f F_{yf}\cos\delta_f - 2\ l_r F_{yr}\right) \end{cases} \tag{3.43}$$

The angle between the vehicle's traveling direction and its longitudinal direction, see Figure 3.6, is called the vehicle side slip angle [7], β, which can be formulated as

$$\beta = \tan^{-1}\left(\frac{v_y}{v_x}\right) \tag{3.44}$$

The speed of the vehicle at the centre of gravity, v_t, can be calculated by

$$v_t = \sqrt{v_x^2 + v_y^2} \tag{3.45}$$

To formulate the tractive forces, two more differential equations must be added to represent the wheel rotations at the front and the rear axles.

Equation 3.46 gives another representation of the vehicle plane motion by considering the vehicle sideslip angle, β, and the yaw rate, r as the states.

$$\begin{cases} \dot{\beta} = \frac{1}{m v_t}\left[2\ F_{yf}\cos\left(\delta_f - \beta\right) + 2\ F_{yr}\cos\left(\beta\right)\right] - r \\ \\ \dot{r} = \frac{1}{I_z}\left(2\ l_f F_{yf}\cos\delta_f - 2\ l_r F_{yr}\right) \end{cases} \tag{3.46}$$

Selecting between these two different representations depends on the application, e.g. in practical cases, depends on the availability of the sensors.

3.3.3 14-DOF Full Vehicle Model

The schematic view of the 14-DOF full vehicle model [5] is given in Figure 3.8. As it can be seen, this vehicle model has four wheels and separated sprung mass and unsprung masses. This model includes 6-DOF representing the longitudinal, lateral, vertical, roll, pitch, and yaw velocities of the sprung mass concentrated at the CG of the vehicle. Each wheel has 2-DOF representing the vertical velocity of the suspension travel and wheel rotational speed. This vehicle model can predict the roll, yaw, and pitch motions of an actual vehicle. The main advantage of the 14-DOF full vehicle model over other models is its ability to predict vehicle roll behaviour even after wheel lift-off. Therefore, this model can be used in developing or testing the rollover prediction/prevention strategies. An interested reader is referred to Appendix B to find more about vehicle models that include roll motion.

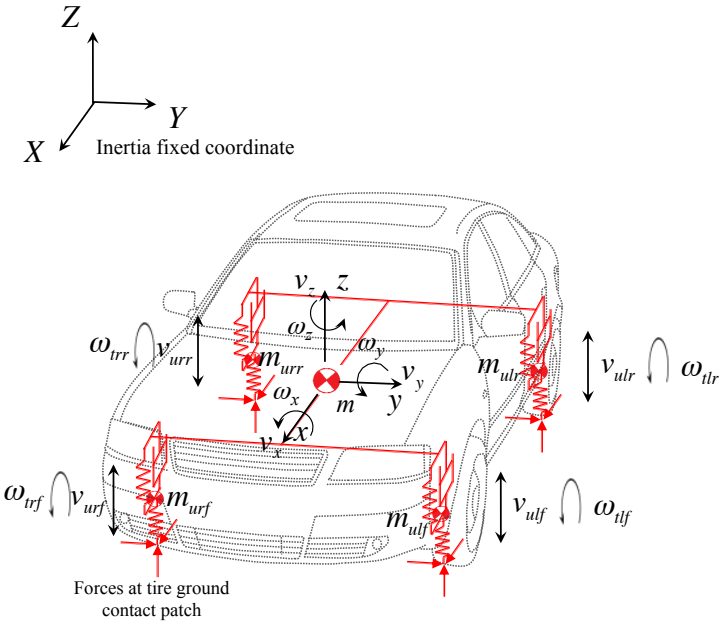

Figure 3.8: Schematic view of the 14-DOF full vehicle model

The set of differential equations governing the dynamics of the 14-DOF vehicle model is given in equation Eq. 3.47. The subscript "ij" in this equation denotes right front (rf), left front (lf), right rear (rr), and left rear (lr). It should be noted that the dynamic equations for the four wheel spins are excluded; however, these equations can be written similarly to Eq. 3.42. The details on deriving 14-DOF full vehicle model equations are provided in Appendix B.

$$
\begin{cases}
\dot{v}_x = \frac{\sum F_{xij}}{m_s} + g\sin\theta - \omega_x v_z + \omega_z v_y \\
\dot{v}_y = \frac{\sum F_{yij}}{m_s} - g\sin\phi\cos\theta - \omega_z v_x + \omega_x v_z \\
\dot{v}_z = \frac{\sum F_{zij}}{m_s} - g\cos(\phi)\cos\theta - \omega_x v_y + \omega_y v_x \\
\dot{\omega}_x = \frac{\sum M_{xij}}{J_x} + \frac{(F_{zslf}+F_{zslr}-F_{zsrf}-F_{zsrr})c}{2J_x} - \omega_y\frac{J_z}{J_x}\omega_z + \omega_z\frac{J_y}{J_x}\omega_y \\
\dot{\omega}_y = \frac{\sum M_{yij}}{J_y} + \frac{(F_{zslr}+F_{zsrr})b}{J_y} - \frac{(F_{zslf}+F_{zsrf})a}{J_y} - \omega_z\frac{J_x}{J_y}\omega_x + \omega_x\frac{J_z}{J_y}\omega_z \\
\dot{\omega}_z = \frac{\sum M_{zij}}{J_z} + \frac{(F_{yslf}+F_{ysrf})a}{J_z} - \frac{(F_{yslr}+F_{ysrt})b}{J_z} + \frac{(-F_{xslf}+F_{xsrf}-F_{xslr}+F_{xsrr})c}{2J_z} \\
\qquad -\omega_x\frac{J_y}{J_z}\omega_y + \omega_y\frac{J_x}{J_z}\omega_x \\
\dot{\theta} = \omega_y\cos\phi - \omega_z\sin\phi \\
\dot{\psi} = \frac{\omega_y\sin\phi}{\cos\theta} + \frac{\omega_z\cos\phi}{\cos\theta} \\
\dot{\phi} = \omega_x + \omega_y\sin\phi\tan\theta + \omega_z\cos\phi\tan\theta \\
\dot{v}_{zuij} = \frac{\cos\phi(\cos\theta(F_{z'gij}-m_{uij}g)+\sin\theta F_{x'gij})-\sin\phi F_{y'gij}-F_{dzij}-x_{sij}k_{sij}-(-v_{zsij}+v_{zuij})b_{sij}}{m_{uij}} \\
\qquad -(v_{yuij}\omega_x - v_{xuij}\omega_y) \\
\dot{x}_{sij} = -v_{zsij} + v_{zuij} \\
\dot{x}_{tij} = v_{z'ij} - (\cos\theta(v_{zuij}\cos\phi + v_{yuij}\sin\phi) - v_{xuij}\sin\theta)
\end{cases}
\tag{3.47}
$$

Chapter 4

Modified Lyapunov Exponent, New Measure of Dynamics

4.1 Overview

The objective of this chapter[1] is to modify the Lyapunov exponents, which can characterize the exponential divergent or convergent rates of the nonlinear dynamics in specific directions and driven by the dynamics in the same directions. Like other measures of the asymptotic behaviors of the nonlinear systems, the modified Lyapunov exponent must exist and be invariant with respect to the initial conditions, which are proven mathematically here.

This chapter is organized as follows. The concept of the modified Lyapunov exponent is developed in Section 4.2. Some indications of the modified exponent are discussed,

[1]This chapter is published in [62].

and without loss of generality; the theorem of the existence and the invariance of the modified Lyapunov exponent for dynamic systems with an asymptotically stable fixed point or an attracting limit cycle is given. Section 4.3 presents an algorithm for practical computation of the modified exponents. Such an algorithm is used in Section 4.4 to demonstrate the concept in some case studies. Finally, a discussion on limitations and further extension of modified Lyapunov exponents is made in Section 4.5.

4.2 Modified Lyapunov Exponent

In this section, the new exponent based on the concept of Lyapunov exponents is developed. The modified Lyapunov exponent is first defined, and its existence is proven. The sufficient condition guaranteeing the modified Lyapunov exponent to be independent of initial conditions (invariance) is then proposed and proven. The algorithm for calculation of the modified Lyapunov exponent is presented. Finally, the modified Lyapunov exponent is computed for various systems to demonstrate the proposed modified Lyapunov exponent.

4.2.1 Definition of the Modified Lyapunov Exponent

The definition of the modified Lyapunov exponent is based on the concept of Lyapunov exponents; however, instead of evolving the perturbation vector with the Jacobian matrix, such a vector is traversed by part of the Jacobian matrix. The aim is to define a measure that characterizes the evolution of the perturbation vector along

the specific direction $\mathbf{u}$ driven by the dynamics in the same direction $\mathbf{u}$.

To formulate the modified Lyapunov exponent, the following time evolution equations are defined:

$$\begin{cases} \dot{\mathbf{x}} = \mathbf{f}(\mathbf{x}) \\ \\ \delta\dot{\mathbf{x}}_u = \mathbf{S}(\mathbf{x})\,\delta\mathbf{x}_u \end{cases} \tag{4.1}$$

The matrix $\mathbf{S}(\mathbf{x})$ represents the flow components along the direction $\mathbf{u}$ and is defined by

$$\mathbf{S}(\mathbf{x}) = \mathbf{P}_u \frac{\partial \mathbf{f}}{\partial \mathbf{x}^{\mathrm{T}}}(\mathbf{x}) \tag{4.2}$$

where $\mathbf{P}_u$ is the orthogonal projection matrix onto $\mathbf{u}$ and is defined by

$$\mathbf{P}_u = \frac{\mathbf{u}\mathbf{u}^T}{\|\mathbf{u}\|^2} \tag{4.3}$$

For better understanding, the geometrical interpretation of Eq. 4.1 for the case of the 2-dimensional system is exhibited in Figure 4.1. As it can be seen, the trajectory $\mathbf{x}(t)$ corresponding to the initial condition $\mathbf{x}(0)$ has been generated by the nonlinear equations while the perturbation vector along the predefined vector $\mathbf{u}$ has been traversed in linear tangent space by Eq. 4.2.

The solution of Eq. 4.1 can be written as

$$\begin{cases} \mathbf{x}(t) = \mathbf{T}^t_{\mathbf{x}(0)} \\ \\ \delta\mathbf{x}_u(t) = d\mathbf{S}^t_{\mathbf{x}(0)}\delta\mathbf{x}_u(0) \end{cases} \tag{4.4}$$

The asymptotic behavior of the perturbation vector $\delta\mathbf{x}_u$ as $t \to +\infty$ is described by the asymptotic behavior of the linear map $d\mathbf{S}^t_{\mathbf{x}(0)}$. To characterize the asymptotic

behavior of this map, the modified Lyapunov exponent corresponded to the direction of $\mathbf{u}$ is defined in terms of the perturbation vector length along $\mathbf{u}$ as

$$\lambda_{Su} = \lim_{t \to +\infty} \frac{1}{t} \ln \frac{\|\delta \mathbf{x}_u(t)\|}{\|\delta \mathbf{x}_u(0)\|} \tag{4.5}$$

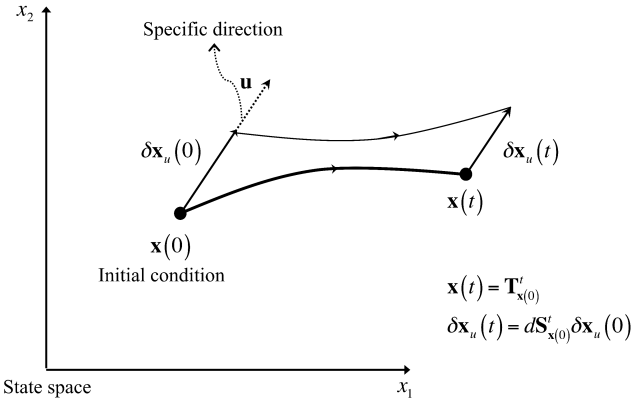

Figure 4.1: Geometrical interpretation of the modified Lyapunov exponent for a 2-dimensional system

In the case of discrete-time systems, the following set of difference equations are considered.

$$\begin{cases} \mathbf{x}[n+1] = \mathbf{f}[\mathbf{x}[n]] \\ \\ \delta \mathbf{x}_u[n+1] = \mathbf{S}[\mathbf{x}[n]] \, \delta \mathbf{x}_u[n] \end{cases} \tag{4.6}$$

Similar to the continuous-time case, $\mathbf{S}[\mathbf{x}[n]]$ is defined as

$$\mathbf{S}[\mathbf{x}[n]] = \mathbf{P}_u \left. \frac{\partial \mathbf{f}}{\partial \mathbf{x}^{\mathrm{T}}} \right|_{\mathbf{x}=\mathbf{x}[n]} \tag{4.7}$$

Then, the modified Lyapunov exponent for discrete-time systems is defined by

$$\lambda_{Su} = \lim_{n \to +\infty} \frac{1}{n} \ln \frac{\|\delta \mathbf{x}_u[n]\|}{\|\delta \mathbf{x}_u[0]\|} \tag{4.8}$$

or equivalently

$$\lambda_{Su} = \lim_{n \to +\infty} \frac{1}{n} \sum_{m=1}^{n} \ln \frac{\|\delta \mathbf{x}_u [m]\|}{\|\delta \mathbf{x}_u [m-1]\|} \tag{4.9}$$

In practical calculations, the infinite-time limit in Eq. 4.5 for continuous-time systems and in Eq. 4.9 for discrete-time systems will be approximated by the finite-time series in Eq. 4.10 and Eq. 4.11 respectively.

$$\lambda_{Su} \approx \frac{1}{t} \ln \frac{\|\delta \mathbf{x}_u (t)\|}{\|\delta \mathbf{x}_u (0)\|} \tag{4.10}$$

$$\lambda_{Su} \approx \frac{1}{n} \sum_{m=1}^{n} \ln \frac{\|\delta \mathbf{x}_u [m]\|}{\|\delta \mathbf{x}_u [m-1]\|} \tag{4.11}$$

In the limit as $t \to +\infty$ or $n \to +\infty$, the finite-time series in Eq. 4.10 and Eq. 4.11 converges to the infinite-time limits [50] in Eq. 4.5 and Eq. 4.9.

4.2.2 Indications of the Modified Lyapunov Exponent

The modified Lyapunov exponent can characterize different features of the dynamic systems depending on the predefined projection matrix. The indications of the modified Lyapunov exponent are given via various examples.

Example 1: The modified Lyapunov exponent can indicate which parts of the dynamics dominate the growth rate of the perturbation vector.

Consider a 2-dimensional discrete-time system with a stable fixed point as given in

Eq. 4.12

$$\begin{cases} x_1[n+1] = f[x_1[n], x_2[n]] \\ \\ x_2[n+1] = g[x_1[n], x_2[n]] \end{cases} \tag{4.12}$$

The dynamics of any perturbation vectors, $\delta\mathbf{x}$, in the tangent space is described by Eq. 4.13.

$$\begin{bmatrix} \delta x_1[n+1] \\ \\ \delta x_2[n+1] \end{bmatrix} = \begin{bmatrix} J_{11}[n] & J_{12}[n] \\ \\ J_{21}[n] & J_{22}[n] \end{bmatrix} \begin{bmatrix} \delta x_1[n] \\ \\ \delta x_2[n] \end{bmatrix} \tag{4.13}$$

where $J_{ij}[n]$ represents the ij-th element of the Jacobian matrix, $\mathbf{J}[n]$, corresponding to the dynamics in Eq. 4.12 at the instant n.

The growth of such a perturbation vector from the instant n to the instant $n+1$ is illustrated in Figure 4.2. As it can be seen the components of the perturbation vector at the instant $n+1$ ($\delta x_1[n+1]$ and $\delta x_2[n+1]$) consist of both the uncoupled dynamics J_{ii} and the coupled dynamics J_{ij} $(i \neq j)$.

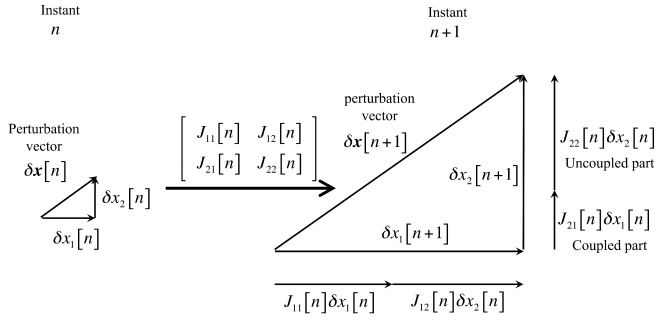

Figure 4.2: Evolution of a perturbation vector in the tangent space for a 2-dimensional discrete-time system

After a large number of n, the perturbation vector aligns itself along the direction of the eigenvector corresponding to the largest Lyapunov exponent, $\lambda^{(1)}$ [30]. For dynamic systems with a fixed point, the direction of this eigenvector is asymptotically constant. Therefore, the right triangles in the instant n and the instant $n+1$ are similar and the perturbation vector component along the direction of the state x_1 grows as $e^{\lambda^{(1)}n}$ (see Section 3.2.5). Now suppose that the projection matrix $\mathbf{P}_x$ is selected as

$$\mathbf{P}_x = \begin{bmatrix} 1 & 0 \\ \\ 0 & 0 \end{bmatrix} \tag{4.14}$$

In this case, $\mathbf{P}_x$ projects the dynamics, $\mathbf{J}[n]$, into the direction of the specific state x_1, namely $\mathbf{S}[n]$ as

$$\mathbf{S}[n] = \begin{bmatrix} J_{11}[n] & J_{12}[n] \\ \\ 0 & 0 \end{bmatrix} \tag{4.15}$$

Therefore, the evolution of a perturbation vector, $\delta\mathbf{x}'$, in the tangent space can be found by

$$\begin{bmatrix} \delta x_1'[n+1] \\ \\ \delta x_2'[n+1] \end{bmatrix} = \begin{bmatrix} J_{11}[n] & J_{12}[n] \\ \\ 0 & 0 \end{bmatrix} \begin{bmatrix} \delta x_1'[n] \\ \\ \delta x_2'[n] \end{bmatrix} \tag{4.16}$$

Since the perturbation vector belongs to the subspace along the state x_1, its second component $\delta x_2'$ is zero and Eq. 4.16 will be reduced to

$$\delta x_1'[n+1] = J_{11}[n]\ \ \delta x_1'[n] \tag{4.17}$$

The growth of the perturbation vector, $\delta\mathbf{x}'$, evolved by Eq. 4.17 from the instant n to the instant $n+1$ is plotted in Figure 4.3.

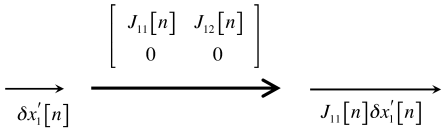

Figure 4.3: Evolution of a perturbation vector in the tangent space for the projected system into the direction of the state x_1

As the comparison between Figure 4.3 and Figure 4.2, Eq. 4.17 gives the growth ratio of the uncoupled part of the perturbation vector $\delta\mathbf{x}$ along the state x_1 in Eq. 4.13. Therefore, the modified Lyapunov exponent λ_{Sx} related to Eq. 4.17 indicates the growth rate of the uncoupled part of the perturbation vector $\delta\mathbf{x}$ component along the direction of the state x_1.

The comparison between $\lambda^{(1)}$ and λ_{Sx} can indicate which parts of the dynamics, the coupled part or the uncoupled part, has more effect on the growth rate of the perturbation vector. In Figure 4.4, suppose that the initial vector along x_1 direction has the length of l_0. If this vector is evolved in the tangent space by the Jacobian matrix $\mathbf{J}[n]$, after long time (large enough n), its x_1 direction component will have the length of l_{t_n} and

$$\frac{l_{t_n}}{l_0} \approx e^{\lambda^{(1)}n} \tag{4.18}$$

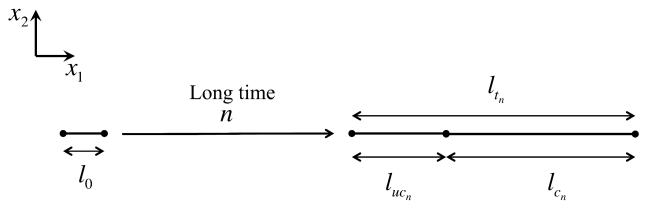

Figure 4.4: Geometric interpretation of the evolved perturbation vector along x_1 direction by the complete dynamics and its projected sub-dynamics

On the other hand, if the initial vector along the x_1 direction is evolved by the projected dynamics into x_1 direction, $\mathbf{S}[n]$, it will have the length of l_{uc_n} for the large n and

$$\frac{l_{uc_n}}{l_0} \approx e^{\lambda_{Sx} n} \tag{4.19}$$

Since $l_{t_n} = l_{uc_n} + l_{c_n}$, it can be concluded that

$$\frac{l_{c_n}}{l_0} \approx e^{\lambda^{(1)} n} - e^{\lambda_{Sx} n} \tag{4.20}$$

Therefore, the comparison between Eq. 4.19 and Eq. 4.20 can indicate which parts of the dynamics, the uncoupled part or the coupled part, has the most effect on the growth rate of the perturbation vector.

Example 2: The modified Lyapunov exponent can provide information about the sub-dynamic systems which dominate the growth rate of the perturbation vectors. With such information, the dynamic analysis in the tangent space can be conducted on the dominant sub-dynamics instead of the entire dynamics.

For a 3-dimensional discrete-time system with a stable fixed point, the perturbation

vectors in the instants n, $\delta\mathbf{x}[n]$, and $n+1$, $\delta\mathbf{x}[n+1]$, are shown by black vectors in Figure 4.5. The asymptotical average growth rate of this perturbation vector in the tangent space is understood by the largest Lyapunov exponent, $\lambda^{(1)}$. On the other hand, as discussed before, the asymptotical average growth rate of the x_1x_2 component of the perturbation vector (dashed black vectors in the gray planes) is also given by $\lambda^{(1)}$.

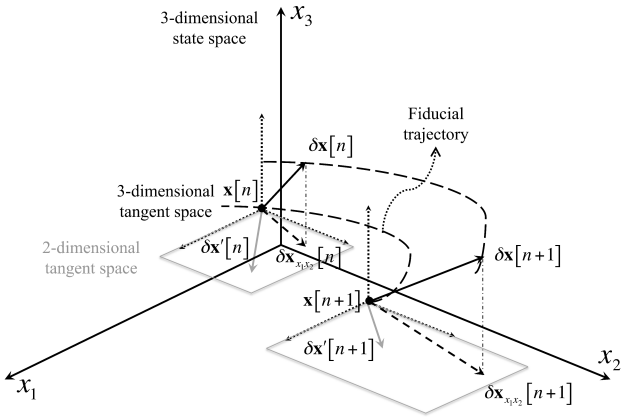

Figure 4.5: Projecting the dynamics of a 3-dimensional system in the tangent space into the x_1x_2 state space

Now suppose the projection matrix, $\mathbf{P}_{x_1x_2}$, projects the dynamics of the tangent space into the 2-dimensional sub state space (gray planes in Figure 4.5), and transforms the perturbation vector $\delta\mathbf{x}'[n]$ at the instant n to the perturbation vector $\delta\mathbf{x}'[n+1]$ at the instant $n+1$. The modified Lyapunov exponent, $\lambda_{Sx_1x_2}$, gives the asymptotical average growth rate of the perturbation vector $\delta\mathbf{x}'$ in the 2-dimensional tangent space driven by the x_1x_2 projected dynamics. The difference between $\lambda^{(1)}$ and $\lambda_{Sx_1x_2}$ is the result of the dynamics in direction of the third state x_3 in the tangent space. In Figure 4.6, the initial perturbation vector in the x_1x_2 plane has the length of l_0.

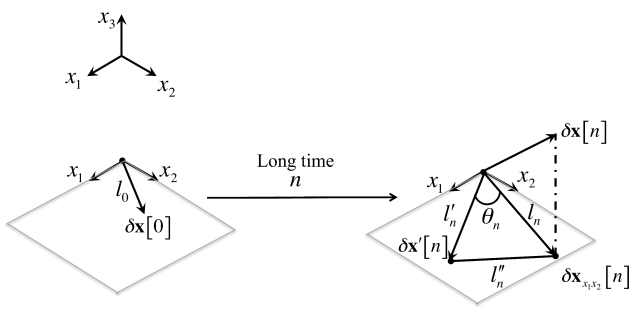

Figure 4.6: Geometric interpretation of the evolved perturbation vector in x_1x_2 direction by the complete dynamics and its projected sub-dynamics

When monitoring the evolution of the perturbation vector $\delta\mathbf{x}[0]$ in the tangent space by the entire dynamics, after a sufficiently long time n, it can be seen that the perturbation vector evolves to $\delta\mathbf{x}[n]$, which its projected component in the x_1x_2 plane, $\delta\mathbf{x}_{x_1x_2}[n]$, has the length of l_n and

$$\frac{l_n}{l_0} \approx e^{\lambda^{(1)}n} \tag{4.21}$$

On the other hand, when monitoring the evolution of the initial perturbation vector $\delta\mathbf{x}[0]$ by the x_1x_2 projected dynamics, at the instant n, the evolved perturbation vector is $\delta\mathbf{x}'[n]$, which has the length of l'_n and

$$\frac{l'_n}{l_0} \approx e^{\lambda_{Sx_1x_2}n} \tag{4.22}$$

The difference vector between the perturbation vector $\delta\mathbf{x}[n]$ and the perturbation vector $\delta\mathbf{x}'[n]$ is due to the dynamics along the state x_3, and it has the length of l''_n. Using the length relations in a triangle

$$l_n^{''2} = l_n^2 + l_n^{'2} - 2l_n l_n' \cos(\theta_n) \tag{4.23}$$

and therefore,

$$l_n^2 + l_n^{'2} - 2l_n l_n' \leq l_n^{''2} \leq l_n^2 + l_n^{'2} + 2l_n l_n' \tag{4.24}$$

Dividing Eq. 4.24 by l_0^2 results in

$$\left(\frac{l_n}{l_0}\right)^2 + \left(\frac{l_n'}{l_0}\right)^2 - 2\left(\frac{l_n}{l_0}\right)\left(\frac{l_n'}{l_0}\right) \leq$$

$$\left(\frac{l_n''}{l_0}\right)^2 \leq \tag{4.25}$$

$$\left(\frac{l_n}{l_0}\right)^2 + \left(\frac{l_n'}{l_0}\right)^2 + 2\left(\frac{l_n}{l_0}\right)\left(\frac{l_n'}{l_0}\right)$$

Now by substituting Eq. 4.21 and Eq. 4.22 into Eq. 4.25, it can be concluded that

$$e^{2\lambda^{(1)}n} + e^{2\lambda_{Sx_1x_2}n} - 2\left(e^{\left(\lambda^{(1)}+\lambda_{Sx_1x_2}\right)n}\right) \leq$$

$$\left(\frac{l_n''}{l_0}\right)^2 \leq \tag{4.26}$$

$$e^{2\lambda^{(1)}n} + e^{2\lambda_{Sx_1x_2}n} + 2\left(e^{\left(\lambda^{(1)}+\lambda_{Sx_1x_2}\right)n}\right)$$

which gives the lower bound and the upper bound for the effects of the neglected dynamics along the state x_3 direction on the growth rate of the perturbation vector in the tangent space.

4.2.3 Existence and Invariant Property of Modified Lyapunov Exponent

In the ergodic theory, there is no difference between discrete-time and continuous-time systems. In fact, discretization of a continuous-time system does not change the nature of attractors and so the Lyapunov exponents [57, 58]. Therefore, the theorem will be given only for the case of discrete-time systems and the proof is based on the multiplicity ergodic theorem of Oseledec (see Section 3.2.5). In addition, the theorem and the proof are given when the attractor is an asymptotically stable equilibrium point or an attracting limit cycle, but they can be extended to other attractors as discussed in the remarks.

4.2.4 Theorem of the Modified Lyapunov Exponent

Consider an autonomous discrete-time dynamic system of the form

$$\mathbf{x}\left[\mathbf{n}+\mathbf{1}\right]=\mathbf{f}\left[\mathbf{x}\left[\mathbf{n}\right]\right] \tag{4.27}$$

where $\mathbf{x}\left[\mathbf{n}\right]\in\mathbb{R}^{\mathbf{m}}$ and $\mathbf{f}$ is an $m\times 1$ vector function. Suppose the following situations:

a) $\mathbf{f}$ has an asymptotically stable fixed point $\mathbf{EP}$ at the origin so that $\mathbf{f}\left[\mathbf{EP}\right]=\mathbf{EP}$ for all n. There is a neighbourhood M of $\mathbf{EP}$ such that

$$\forall\mathbf{x}\in M:\lim_{n\to+\infty}\mathbf{f}\left[\mathbf{x}\right]=\mathbf{EP} \tag{4.28}$$

M is known as the stability region of the asymptotically stable fixed point $\mathbf{EP}$.

b) $\mathbf{f}$ has an attracting limit cycle and there exists some positive n_0 such that

$$\mathbf{x}\left[n+n_0\right]=\mathbf{x}\left[n\right] \tag{4.29}$$

Let denote the points $\mathbf{x}\in\mathbb{R}^m$ satisfy Eq. 4.29 by $\mathbf{Q}$ and define the closed orbit $\mathbf{\Gamma}$ as

$$\mathbf{\Gamma}=\left\{\mathbf{f}\left[\mathbf{Q}\left[n+i\right]\right]:i=0,\cdots,n_0\right\} \tag{4.30}$$

There is a neighbourhood M of the close orbit $\mathbf{\Gamma}$ such that

$$\forall\mathbf{x}\in M:\ \lim_{n\to+\infty}\mathbf{f}\left[\mathbf{x}\right]\to\mathbf{\Gamma} \tag{4.31}$$

M is called the domain of attraction for the closed orbit $\mathbf{\Gamma}$.

Theorem- Let ρ be an ergodic probability measure on the neighbourhood M, and let $\mathbf{f}:M\to M$ be a measure preserving map. Let $\mathbf{S}:M\to$ the $m\times m$ matrix be defined as

$$\mathbf{S}\left[\mathbf{x}\left[n\right]\right]=\mathbf{P}_u\left.\frac{\partial\mathbf{f}}{\partial\mathbf{x}^{\mathrm{T}}}\right|_{\mathbf{x}=\mathbf{x}[n]} \tag{4.32}$$

where $\mathbf{P}_u$ is the projection matrix into the direction of the vector $\mathbf{u}$, and $\frac{\partial\mathbf{f}}{\partial\mathbf{x}^T}$ is the Jacobian matrix.

1- $\mathbf{S}$ is a measurable function, and $\ln^+\left\|\mathbf{S}\left[\mathbf{x}\right]\right\|$ is Lebesgue integrable.

$$\ln^+\left\|\mathbf{S}\left[\mathbf{x}\right]\right\|\in L^{-1}\left(M,\beta,\rho\right) \tag{4.33}$$

2- Define the matrix

$\mathbf{S}^n_{\mathbf{x}[0]} = \mathbf{S}\left[\mathbf{f}^{n-1}\left[\mathbf{x}\left[0\right]\right]\right] \cdots \mathbf{S}\left[\mathbf{f}^1\left[\mathbf{x}\left[0\right]\right]\right]\mathbf{S}\left[\mathbf{x}\left[0\right]\right]$, then for ρ-almost all $\mathbf{x}\left[0\right]$, the following limit exists:

$$\lim_{n\to\infty}\left(\mathbf{S}^{n*}_{\mathbf{x}[0]}\mathbf{S}^{n}_{\mathbf{x}[0]}\right)^{\frac{1}{2n}} = \mathbf{\Lambda}_{Su\mathbf{x}[0]} \tag{4.34}$$

where $*$ denotes the matrix transposition. Furthermore, write the logarithm of the eigenvalues of $\mathbf{\Lambda}_{Su\mathbf{x}[0]}$ as $\lambda^{(i)}_{Su\mathbf{x}[0]}$ such that $\lambda^{(1)}_{Su\mathbf{x}[0]} \geq \lambda^{(2)}_{S\mathbf{x}[0]} \geq \cdots$. The largest one, $\lambda^{(1)}_{Su\mathbf{x}[0]}$, is the modified Lyapunov exponent in the direction of the vector $\mathbf{u}$.

3- $\lambda^{(1)}_{Su\mathbf{x}[0]}$ is ρ-almost everywhere constant (independent of $\mathbf{x}\left[0\right]$) since ρ is ergodic.

Proof:

a) asymptotically stable fixed point- Define the stability region M of the asymptotically stable fixed point **EP** at the origin of the state space as

$$M = \left\{\mathbf{x}\in\mathbb{R}^m : \lim_{n\to+\infty}\mathbf{f}\left[\mathbf{x}\right] = \mathbf{EP}\right\} \tag{4.35}$$

The Borel σ-algebra of M that includes set $\{\mathbf{EP}\}$ can be defined as

$$\beta := \left\{\{\mathbf{EP}\}, \left\{\mathbf{x}_{(1)}, \mathbf{x}_{(2)}, \cdots, \mathbf{x}_{(i)}, \cdots, \mathbf{x}_{(n)}\right\}, \phi, M\right\} \tag{4.36}$$

The graphic interpolation of M is given in Figure 4.7.

Define the measure ρ as

$$\rho = \delta_\beta\left(\mathbf{EP}\right) \tag{4.37}$$

where $\delta\left(\mathbf{EP}\right)$ is Dirac measure [57].

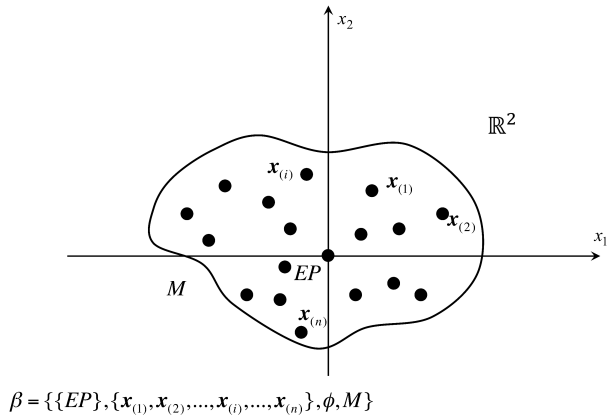

Figure 4.7: β Borel σ-algebra of sets that includes $\{\mathbf{EP}\}$

This Delta measure is a measure on the set β defined for a given $\mathbf{x} \in M$ and any measurable set $\mathbf{B} \subseteq \beta$ by

$$\delta_\beta(\mathbf{B}) = \begin{cases} 1, & \mathbf{x} \in \mathbf{B} \\ 0, & \mathbf{x} \notin \mathbf{B} \end{cases} \tag{4.38}$$

This definition for probability measure ρ is in complete agreement with the definition of the stable fixed point, considering that the ρ is the probability of staying in a visited point forever.

The triple (M, β, ρ) constructs a probability measure space. Measure ρ is invariant under the dynamical system (measure-preserving map) since

$$\rho\left(\mathbf{f}^{-1}(\mathbf{x})\right) = \rho(\mathbf{x}) \tag{4.39}$$

The invariant probability measure ρ is ergodic [57] (indecomposable) because it cannot be decomposed to others' invariant probability measure such that

$$\rho = \frac{1}{2}\rho_1 + \frac{1}{2}\rho_2 \quad where \;\; \rho_1 \neq \rho_2 \tag{4.40}$$

Since both $\mathbf{P}_u$ and $\frac{\partial \mathbf{f}}{\partial \mathbf{x}^T}$ in Eq. 4.32 are measurable maps, their composition, $\mathbf{S}[\mathbf{x}]$, is also measurable. In addition, due to the submultiplicative property (see Section 3.2.5) of the operator norm in Euclidean space

$$\begin{gathered} \textstyle\sum_M \ln^+ \|\mathbf{S}[\mathbf{x}]\| \ \rho(\mathbf{x}) \leq \\ \textstyle\sum_M \ln^+ \|\mathbf{P}_u\| \rho(\mathbf{x}) \ + \sum_M \ln^+ \left\| \frac{\partial \mathbf{f}}{\partial \mathbf{x}^{\mathrm{T}}} \right\| \ \rho(\mathbf{x}) < \infty \end{gathered} \tag{4.41}$$

Note that the orthogonal projection matrix is symmetric, and its spectral norm is always one. Therefore, the logarithm of the spectral norm for the projection matrix is zero.

By substituting the $\mathbf{T}$ function with the $\mathbf{S}$ function in Oseledec's theorem, according to his theorem, $\mathbf{\Lambda}_{Su\mathbf{x}[0]}$ shown in Eq. 4.34, exists and the logarithm of the largest eigenvalue of this matrix , $\lambda^{(1)}_{Su\mathbf{x}[0]}$, is the modified Lyapunov exponent.

Moreover, in consequence of the Oseledec's theorem the modified Lyapunov exponent is independent of $\mathbf{x}[0]$ since ρ is ergodic.

b) attracting limit cycle- The proof of the theorem when the attractor is a limit cycle is similar to the proof given above, however; in this situation the ergodic probability measure ρ is described by

$$\rho = \frac{1}{n_0} \sum_{j=1}^{n_0} \delta_\beta(\mathbf{\Gamma}) \tag{4.42}$$

where

$$\delta_\beta(\mathbf{\Gamma}) = \begin{cases} 1, & \mathbf{x}[n+j] \in \mathbf{\Gamma} \\ 0, & \mathbf{x}[n+j] \notin \mathbf{\Gamma} \end{cases} \tag{4.43}$$

Remark 1: Since $\lambda^{(1)}_{Su\mathbf{x}[0]}$ is independent of the initial conditions, the reference to a specific initial condition can be omitted, and it can be rewritten as $\lambda^{(1)}_{Su}$. This exponent is in fact the modified Lyapunov exponent, λ_{Su}, defined in Eq. 4.9 where the subscript $^{(1)}$ has been omitted.

Remark 2: Although the theorem is expressed for systems with an exponentially stable fixed point or an attracting limit cycle, it can be applied to the systems with quasiperiodic attractor by defining the invariant ergodic measure ρ as the Haar measure [58].

Remark 3: The existence of the modified Lyapunov exponent is not restricted to the type of the attractors; however, its independency from initial conditions depends on the ergodic property of the probability measure ρ. Therefore, when a system has strange attractors, a new ergodic probability measure ρ needs to be defined. The definition of the portability measure depends on the attractors. For chaotic systems the attractors may not have an open basin of attraction. Therefore, even a small uncertainty, e.g., noise in calculation, may force the system to jump among several attractors [57] which makes the definition of the probability measure a challenge [57, 58].

Remark 4: In stability control design, the aim of the controller is to force specific states to follow a desired trajectory by using an external energy source. Whenever the dynamics include coupled states, the effects of the controller on the robustness of other states need to be considered. If the effect of the controller on other states is considered as a perturbation, the Example 1 and the Example 2 can be extended to measure its effects on other states.

4.3 Computation of Modified Lyapunov Exponent

To compute the modified Lyapunov exponent numerically, the continuous-time limit in Eq. 4.5 needs to be discretized and expanded as

$$\lambda_{Su} = \lim_{n \to +\infty} \frac{1}{n\tau} \sum_{m=1}^{n} \ln \frac{\|\delta \mathbf{x}_u [m\tau]\|}{\|\delta \mathbf{x}_u [(m-1)\tau]\|} \tag{4.44}$$

where τ is the step size in seconds and n is the number of iterations. After a large number of iterations, the limit in Eq. 4.44 can be approximated by

$$\lambda_{Su} \approx \frac{1}{n\tau} \sum_{m=1}^{n} \ln \frac{\|\delta \mathbf{x}_u [m\tau]\|}{\|\delta \mathbf{x}_u [(m-1)\tau]\|} \tag{4.45}$$

The algorithm utilized to compute the modified Lyapunov exponent can be summarized as follows:

Step 1: Set the maximum number of iterations k and the convergence accuracy as the termination criteria, set the value of step-time τ for the continuous-time case, and set $n = 1$.

Step 2: Select the specific vector $\mathbf{u}$ to produce the corresponding projection matrix $\mathbf{P}_u$.

Step 3: Select an arbitrary initial condition, and an arbitrary initial vector along the predefined vector.

Step 4: Evolve Eq. 4.1 up to the next τ for the continuous time system, or Eq. 4.6 for the discrete-time system, and compute the corresponding new $\mathbf{x}_u ((n+1)\tau)$ and $\delta \mathbf{x}_u ((n+1)\tau)$, or $\mathbf{x}_u [n+1]$ and $\delta \mathbf{x}_u [n+1]$.

Step 5: Compute the modified Lyapunov exponent by the formula given in Eq. 4.10 or Eq. 4.11.

Step 6: Normalize the solution of the perturbation vector, dividing the vector by its magnitude, which will result in the unit vector and set $n = n + 1$.

Step 7: If the termination criterion is not satisfied, set up the next initial conditions as $\begin{cases} \mathbf{x}(n\tau) \\ \frac{\delta \mathbf{x}_u(n\tau)}{\|\delta \mathbf{x}_u(n\tau)\|} \end{cases}$ for the continuous-time case, or $\begin{cases} \mathbf{x}[n] \\ \frac{\delta \mathbf{x}_u[n]}{\|\delta \mathbf{x}_u[n]\|} \end{cases}$ for the discrete-time case and go to the step 4. Otherwise go to the step 8.

Step 8: Recall the last computed exponent from step 5 as the approximation of the modified Lyapunov exponent and go to the end.

As it can be seen, the solution of the perturbation vector is normalized to avoid overflow in the numerical calculation as a result of the possible large divergence. This normalization does not affect the value of the modified Lyapunov exponent because it has been defined based on the length ratio of the perturbation vector after and before evolving the linear transformation, and the linear transformation preserves this length ratio.

4.4 Numerical Case Studies

In this section, various discrete-time and continuous-time nonlinear systems will be considered, and their modified Lyapunov exponents for predefined projection matrices will be computed. The example of the discrete-time systems is the Henon map in a stable configuration. In the case of the continuous-time studies, the Lorenz sys-

tem in the stable configuration and the Van der Pol system with the limit cycle are considered. In addition to these well-known continuous nonlinear systems, the single-track vehicle model is also studied as an engineering example. The corresponding simulations in these case studies have been generated by MATLAB software, and the fourth-order Runge-Kutta method has been employed as the solving method.

4.4.1 Discrete-time Systems

Henon Map

Henon map is one of the most famous nonlinear chaotic systems. It has two states with coupling difference equations given in Eq. 4.46.

$$\begin{cases} x\left[n+1\right] = y\left[n\right] + 1 - a\, x^2\left[n\right] \\ y\left[n+1\right] = b\, x\left[n\right] \end{cases} \tag{4.46}$$

For constants $a = 0.1$ and $b = 0.1$, the Henon map converges to the fixed point $(1, 0.1)$ as shown in Figure 4.8.

In this case study, the orthogonal projection into the state x direction, given in Eq. 4.47, has been considered, and the corresponded modified Lyapunov exponent in this stable configuration has been computed.

$$\mathbf{P}_x = \begin{bmatrix} 1 & 0 \\ 0 & 0 \end{bmatrix} \tag{4.47}$$

By setting the initial condition as $(2, 2)$ and iterating the algorithm up to $1,000$ times, the modified Lyapunov exponent converges to the value of $\lambda_{Sx} = -1.6092$. The trend of the convergence has been illustrated in Figure 4.9.

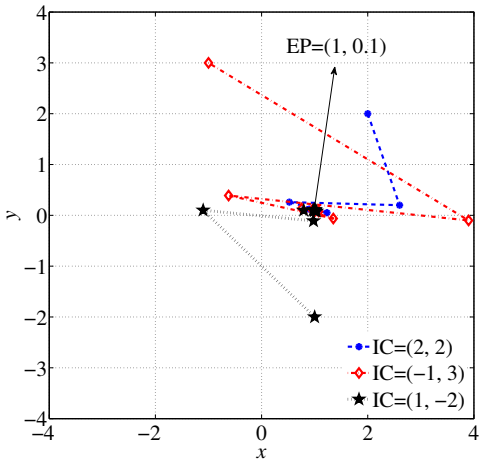

Figure 4.8: Phase portrait of Henon map in the stable configuration, $a = 0.1$ and $b = 0.1$, for three different initial conditions

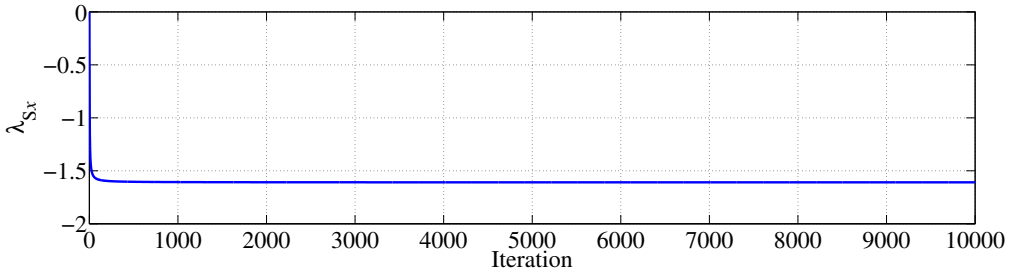

Figure 4.9: Evolution of the modified Lyapunov exponent, λ_{Sx}, for Henon map in the stable configuration

To exhibit the independence of the modified Lyapunov exponent from initial conditions, numerous simulations with different initial conditions have been conducted. The values of the modified Lyapunov exponent for some of those trials are reported in Table 4.1.

Table 4.1: Modified Lyapunov exponent computed for three different initial conditions for Henon map with stable configuration

Initial conditions, $(x(0), y(0))$	λ_{Sx}
$(2, 2)$	-1.609164
$(-1, 3)$	-1.609182
$(1, -2)$	-1.609291

To explore the indication of the modified Lyapunov exponent as discussed in Example 1 (see Section 4.2.2) in the Henon map, the largest Lyapunov exponent is computed. Figure 4.10 depicts the time evolution of the largest Lyapunov exponent for 10000 iterations.

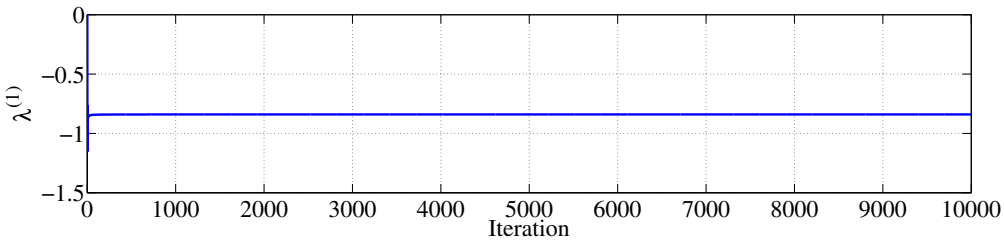

Figure 4.10: Evolution of the largest Lyapunov exponent, $\lambda^{(1)}$, for Henon map in the stable configuration

The largest Lyapunov exponent, $\lambda^{(1)}$, converges to the value of -0.840135. The comparison between $\lambda^{(1)} = -0.840135$ and $\lambda_{Sx} = -1.60929$ suggests that for the Henon map in the tangent space, the dynamics of the coupled dynamics in the direction of the state x must be against the dynamics of the uncoupled part in that direction. In addition, the effect of the uncoupled dynamics on the perturbation vector after the

large number of iterations can be found from Eq. 4.20 as

$$\frac{l_{cn}}{l_0} = e^{-0.840135n} - e^{-1.60929n} \tag{4.48}$$

Since both $\lambda^{(1)}$ and λ_{Sx} are negative, for large values of n Eq. 4.48 is equal to zero, which means the growth of the perturbation vector in the tangent space is dominated by the uncoupled dynamics in the direction of the state x.

To verify this claim, the Jacobian of the Henon map is given in Eq. 4.49.

$$\mathbf{J}_{Henon} = \begin{bmatrix} -2\ a\ x\,[n-1] & 1 \\ \\ b & 0 \end{bmatrix} \tag{4.49}$$

where $a = 0.1$ and $b = 0.1$. After a large number of iterations where the states are very close to the equilibrium point $(x = 1, y = 0.1)$, the Jacobian matrix will be

$$\mathbf{J}_{Henon} = \begin{bmatrix} -0.2 & 1 \\ \\ 0.1 & 0 \end{bmatrix} \tag{4.50}$$

The element J_{11} shrinks the x component of the perturbation vector at the instant $n-1$ and keeps it in x component of the perturbation vector at the instant x while the element J_{12} adds the exact value of the y component of the perturbation vector at the instant $n-1$ to the x component of the perturbation vector at the instant n. Therefore, the dynamics due to the J_{12} acts almost against the shrinking of the perturbation vector due to J_{11} as it was claimed by the comparison between $\lambda^{(1)}$ and λ_{Sx}. However, the negative largest Lyapunov exponent indicates that the

perturbation vector shrinks in the overall. Therefore, it can be claimed that the average growth rate of the perturbation vector is dominated by the dynamics due to the J_{11} element.

4.4.2 Continuous-time Systems

Lorenz System

The Lorenz system is a continuous-time nonlinear system which consists of three ordinary differential equations as given in Eq. 4.51.

$$\begin{cases} \dot{x} = \sigma\left(y - x\right) \\ \dot{y} = rx - y - xz \\ \dot{z} = -bz + xy \end{cases} \tag{4.51}$$

To extend the study on Lorenz system, three projection matrices, Eq. 4.52, Eq. 4.53, Eq. 4.54, are defined and their corresponded modified Lyapunov exponent are computed.

$$\mathbf{P}_x = \begin{bmatrix} 1 & 0 & 0 \\ 0 & 0 & 0 \\ 0 & 0 & 0 \end{bmatrix} \tag{4.52}$$

$$\mathbf{P}_{u'} = \begin{bmatrix} 0.3333 & 0.3333 & 0.3333 \\ 0.3333 & 0.3333 & 0.3333 \\ 0.3333 & 0.3333 & 0.3333 \end{bmatrix} \tag{4.53}$$

$$\mathbf{P}_{xy} = \begin{bmatrix} 1 & 0 & 0 \\ 0 & 1 & 0 \\ 0 & 0 & 0 \end{bmatrix} \tag{4.54}$$

Here, $\mathbf{P}_x$ projects to the direction along x state, $\mathbf{P}_{u'}$ projects to the $\mathbf{u}'$ given in Eq. 4.55, and $\mathbf{P}_{xy}$ projects to the $x - y$ plane.

$$\mathbf{u}' = \begin{bmatrix} 1 \\ 1 \\ 1 \end{bmatrix} \tag{4.55}$$

For the values of $r < 1$, the Lorenz system has only one stable fixed point in the origin. The Lorenz parameters are selected as $\sigma = 14$, $r = 0.5$, and $b = 3$. The trajectories of this Lorenz system for three different initial conditions are shown in Figure 4.11.

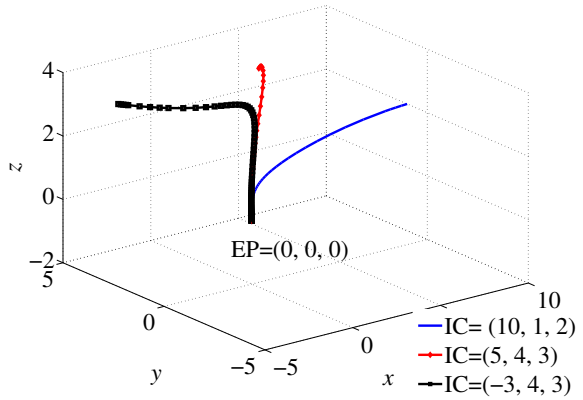

Figure 4.11: Phase portrait of Lorenz system in stable configuration, $\sigma = 14$, $r = 0.5$, and $b = 3$, for three different initial conditions

To find three modified Lyapunov exponents, λ_{Sx}, $\lambda_{Su'}$, and λ_{Sxy}, select an arbitrary initial condition such as $(10, 1, 2)$, set $\tau = 0.01$ s and run the algorithm. After

sufficiently long time (4096 seconds), the modified Lyapunov exponents are $\lambda_{Sx} = -14$, $\lambda_{Su'} = -1.1676$, and $\lambda_{Sxy} = -0.4824$.

The time history of λ_{Sx} has been plotted in Figure 4.12(a). It is notable that in this case, the corresponding modified Lyapunov exponent is simply the minus value of $\sigma = 14$. The reason is that for a perturbation vector in the tangent space along the x state, the dynamic equations of the projected system reduced to

$$\dot{\delta x'} = -\sigma \, \delta x' \tag{4.56}$$

Figure 4.12(b) illustrates the convergence trend for $\lambda_{Su'}$ and Figure 4.12(c) shows the time evolution of λ_{Sxy}.

These modified Lyapunov exponents were computed for the specific initial condition; however, as addressed before, they are independent from the selected initial conditions. To demonstrate this invariant property, the values of modified Lyapunov exponents for a large number of different initial conditions have been computed. Three sets of those initial conditions and their correspond modified Lyapunov exponents are given in Table 4.2. It can be seen that the modified Lyapunov exponents converge approximately to the same values.

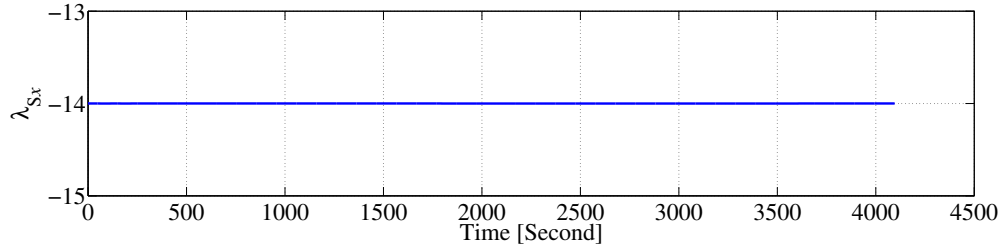

(a)

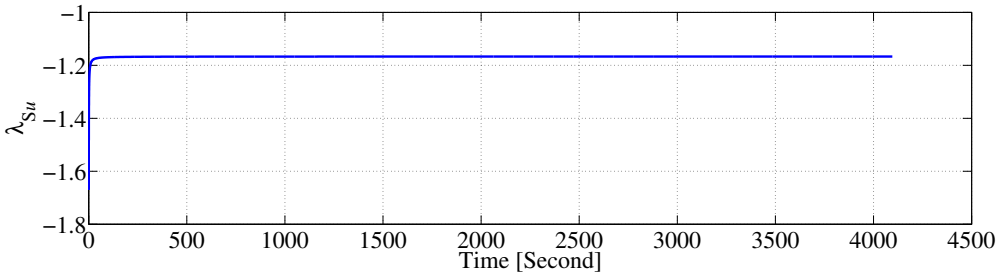

(b)

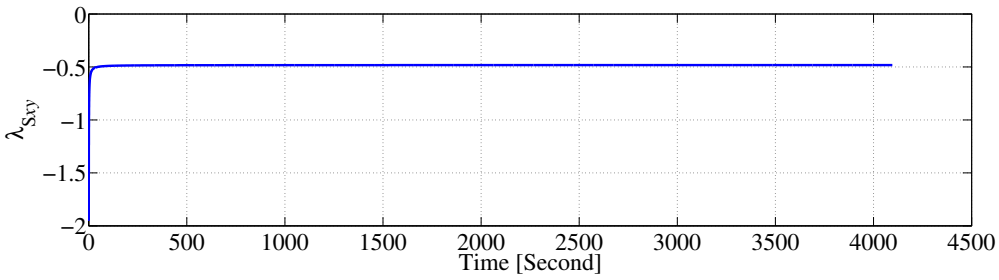

(c)

Figure 4.12: Evolution of the modified Lyapunov exponent for Lorenz system in stable configuration for (a) λ_{Sx}, (b) $\lambda_{Su'}$, and (c) λ_{Sxy}

To demonstrate the indication of the modified Lyapunov exponent as discussed in Example 2 (see Section 4.2.2) in Lorenz system, the largest Lyapunov exponent is computed and its time history for 4096 seconds is given in Figure 4.13. The largest Lyapunov exponent converges to the value of -0.4827 that is almost identical to the value of λ_{Sxy}. It suggests that the dynamics along the z direction have a negligible

Table 4.2: Modified Lyapunov exponents computed for three different initial conditions in Lorenz system with stable configuration

Initial conditions, $(x(0), y(0), z(0))$	λ_{Sx}	$\lambda_{Su'}$	λ_{Sxy}
$(10, 1, 2)$	-14	-1.16673	-0.48236
$(5, 4, 3)$	-14	-1.16668	-0.48269
$(-3, 4, 3)$	-14	-1.16661	-0.48269

effect on the asymptotic behaviour of the perturbation vector as it traverses the tangent space.

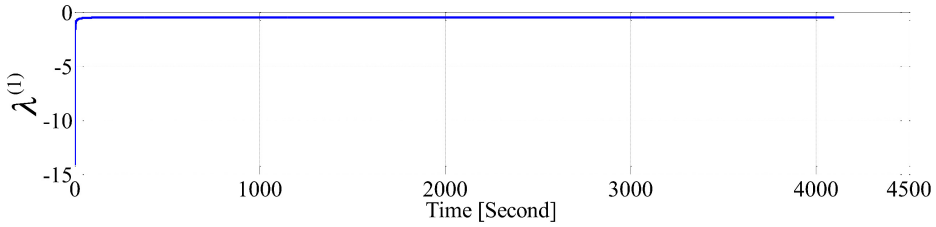

Figure 4.13: Evolution of the largest Lyapunov exponent for Lorenz system in the stable configuration

To justify this statement, the Jacobian matrix for Lorenz system is given in Eq. 4.57.

$$\mathbf{J}_{Lorenz} = \begin{bmatrix} -\sigma & \sigma & 0 \\ r - z & -1 & -x \\ y & x & -b \end{bmatrix} \tag{4.57}$$

When $t \to \infty$, the states are close to the equilibrium point at $(0,\ 0\ , 0)$ and J_{Lorenz} is

$$\mathbf{J}_{Lorenz} = \begin{bmatrix} -\sigma & \sigma & 0 \\ r & -1 & 0 \\ 0 & 0 & -b \end{bmatrix} \tag{4.58}$$

From Eq. 4.58, it can be seen that the dynamic along the z state only affects the z-component of the perturbation vector as $t \to \infty$. Moreover, the dynamics along the x state and the y state directions do not affect the z-component of the perturbation vector. Since b has the positive value of 3, the z-component of the perturbation vector is continuously shrinking and its effect on the value of the largest Lyapunov exponent is negligible.

Projection to the $x - y$ plane is equivalent to considering the dynamic subsystem that only includes the dynamics along the states x and y directions. In this special case, the modified Lyapunov exponent is the largest Lyapunov exponent of the xy subsystem computed by the method proposed in [4]. In fact, if the left projection, $\mathbf{\Pi}_l$, and right projection, $\mathbf{\Pi}_r$, in [4] are considered as given in Eq. 4.59 and Eq. 4.60,

$$\mathbf{\Pi}_l = \begin{bmatrix} 1 & 0 & 0 \\ \\ 0 & 1 & 0 \end{bmatrix} \tag{4.59}$$

$$\mathbf{\Pi}_r = \begin{bmatrix} 1 & 0 \\ \\ 0 & 1 \\ \\ 0 & 0 \end{bmatrix} \tag{4.60}$$

then the complete projection matrix, $\mathbf{\Pi}_c$, in [4] is

$$\mathbf{\Pi}_c = \mathbf{\Pi}_l \, \mathbf{\Pi}_r = \begin{bmatrix} 1 & 0 & 0 \\ 0 & 1 & 0 \\ 0 & 0 & 0 \end{bmatrix} \tag{4.61}$$

which is equivalent to the projection matrix $\mathbf{P}_{xy}$ in this study.

On the other hand, considering the definition of the conditional Lyapunov exponent in [36], the modified Lyapunov exponent in this special case is equivalent to the largest conditional Lyapunov exponent corresponding to the xy subsystem of the Lorenz system. It is notable to mention that the work in [36] or [4] is a special case of the work presented in this thesis when the vector $\mathbf{u}$ is considered along a state direction or the dynamics is projected into the subspace spanned by the state vectors.

Van der Pol System

The normalized form of the Van der Pol equation is given in Eq. 4.62.

$$\begin{cases} \dot{x} = y \\ \dot{y} = -x - (x^2 - \gamma)\, y \end{cases} \tag{4.62}$$

For positive parameters $\gamma > 0$ the Van der Pol equation produces attracting limit cycles. Figure 4.14 demonstrates the phase portrait of the Van der Pol equation when $\gamma = 0.5$ for three different initial conditions.

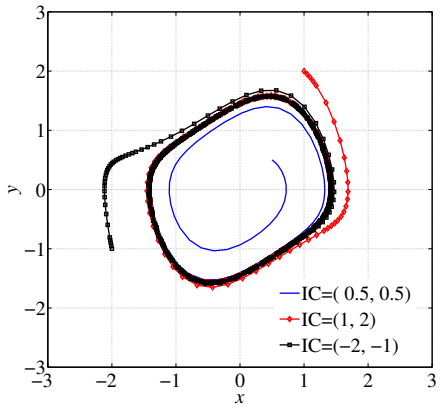

Figure 4.14: Phase portrait for Van der Pol system with an attracting limit cycle, $\gamma = 0.5$, for three different initial conditions

To prove that Van der Pol system has a stable limit cycle when $\gamma = 0.5$, the spectrum of the Lyapunov exponents, $\lambda^{(1)}$ and $\lambda^{(2)}$, are computed. The time histories for these two Lyapunov exponents are given in Figure 4.15. It can be seen that the largest Lyapunov exponent, $\lambda^{(1)}$, converges to zero and the second Lyapunov exponent converges to -0.7314. The zero exponent is the indication of the existence of the limit cycle.

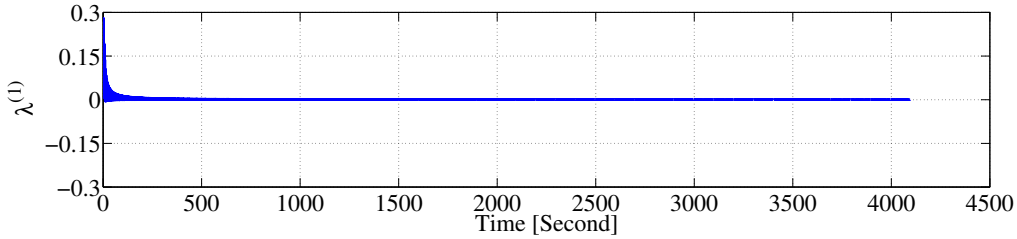

(a)

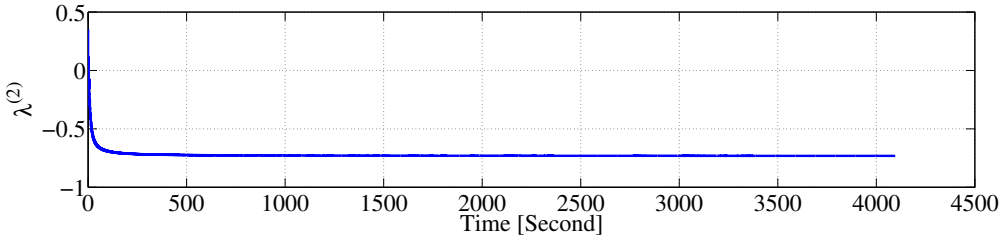

(b)

Figure 4.15: Evolution of the Lyapunov exponents, (a) $\lambda^{(1)}$ and (b) $\lambda^{(2)}$, for Van der Pol system with a attracting limit cycle, $\gamma = 0.5$

In following the modified Lyapunov exponent along the vector $\mathbf{u}''$ in Eq. 4.63 with corresponded orthogonal projection matrix $\mathbf{P}_{u''}$ in Eq. 4.64 will be computed.

$$\mathbf{u}'' = \begin{bmatrix} 1 \\ \\ 1 \end{bmatrix} \tag{4.63}$$

$$\mathbf{P}_{u''} = \begin{bmatrix} 0.5 & 0.5 \\ \\ 0.5 & 0.5 \end{bmatrix} \tag{4.64}$$

Running the algorithm for 4096 seconds with step size $\tau = 0.01s$ for the initial condition $(0.5, 0.5)$, the corresponding modified Lyapunov exponent turned out to be $\lambda_{Su''} = -0.2536$. The time evolution of this exponent is shown in Figure 4.16. Since the modified Lyapunov exponent has the negative value, it can be concluded that the

perturbation vector along the direction of the vector $\mathbf{u}''$ shrinks as it is evolved by the corresponding projected dynamics.

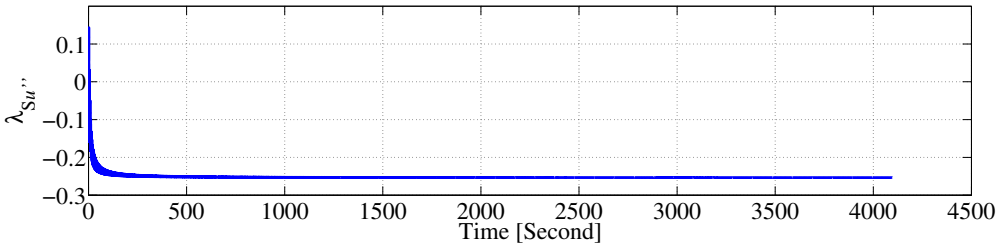

Figure 4.16: Evolution of the modified Lyapunov exponent for Van der Pol system with an attracting limit cycle, $\gamma = 0.5$

To demonstrate that the modified Lyapunov exponent is independent of initial conditions, $\lambda_{Su''}$ has been computed for different initial conditions. Table 4.3 reports the results for three of those that demonstrate the independency from the starting point.

Table 4.3: Modified Lyapunov exponent computed for three different initial conditions in Van der Pol system with an attracting limit cycle

Initial conditions, $(x(0), y(0))$	$\lambda_{Su''}$
$(0.5, 0.5)$	-0.25358
$(1, 2)$	-0.25397
$(-2, -1)$	-0.25389

Bicycle Vehicle Model

In this study, a bicycle vehicle model with nonlinear tires and constant longitudinal velocity in steady-state cornering is considered [43].

The final set of equations for the single-track vehicle model is given in Eq. 4.65.

$$\begin{cases} \dot{v}_y = \dfrac{-2C_{af}\cos\left(\delta_f\right)\left(\frac{v_y+l_f r}{v_x}-\delta_f\right)\left[1+k_f\left(\frac{v_y+l_f r}{v_x}-\delta_f\right)^2\right]}{m} \\ \qquad -\dfrac{2C_{ar}\left(\frac{v_y-l_r r}{v_x}\right)\left[1+k_r\left(\frac{v_y-l_r r}{v_x}\right)^2\right]}{m} - v_x r \\ \dot{r} = \dfrac{-2C_{af}l_f\cos\left(\delta_f\right)\left(\frac{v_y+l_f r}{v_x}-\delta_f\right)\left[1+k_f\left(\frac{v_y+l_f r}{v_x}-\delta_f\right)^2\right]}{I_z} \\ \qquad +\dfrac{2C_{ar}l_r\left(\frac{v_y-l_r r}{v_x}\right)\left[1+k_r\left(\frac{v_y-l_r r}{v_x}\right)^2\right]}{I_z} \end{cases} \tag{4.65}$$

The values of the model parameters as given in Table 4.4 are taken from [43].

Table 4.4: Single-track vehicle model data

Parameters	Nominal Values
$C_{\alpha f}$	57300 $[N/rad]$
$C_{\alpha r}$	57300 $[N/rad]$
k_f	4.87
k_r	4.87
l_f	1.37 $[m]$
l_r	1.86 $[m]$
I_z	6550 $[kg \cdot m^2]$
m	2527 $[kg]$
v_x	20 $[m/s]$
δ_f	5^o

In the steady-state cornering with $\delta_f = 5^o$, the vehicle model has an equilibrium point located at the point $(-0.729,\ 0.368)$ as shown in Figure 4.17. In this figure, the phase portraits for three different initial conditions are also plotted. It can be seen that the states attract asymptotically to the equilibrium point regardless of the started initial conditions. To prove that this equilibrium point is stable, the spectrum of the Lyapunov exponents, $\lambda^{(1)}$ and $\lambda^{(2)}$, are computed. The time histories for these

two Lyapunov exponents are given in Figure 4.18. It can be seen that both of them have the negative value -4.1269.

Since both Lyapunov exponents are negative, the equilibrium point is exponentially stable and all the disturbances initiated in its domain of attraction will be damped asymptotically.

To demonstrate the concept of the modified Lyapunov exponent in the single-track vehicle model, the modified Lyapunov exponents for the dynamics along different directions are computed. These directions include the v_y state direction, r state direction, $r = v_y$, and $r = -v_y$ directions with corresponded projection matrices given in Eq. 4.66 to Eq. 4.69.

$$\mathbf{P}_{v_y} = \begin{bmatrix} 1 & 0 \\ 0 & 0 \end{bmatrix} \tag{4.66}$$

$$\mathbf{P}_{r} = \begin{bmatrix} 0 & 0 \\ 0 & 1 \end{bmatrix} \tag{4.67}$$

$$\mathbf{P}_{r=v_y} = \begin{bmatrix} 0.5 & 0.5 \\ 0.5 & 0.5 \end{bmatrix} \tag{4.68}$$

$$\mathbf{P}_{r=-v_y} = \begin{bmatrix} 0.5 & -0.5 \\ -0.5 & 0.5 \end{bmatrix} \tag{4.69}$$

To compute the modified Lyapunov exponents, λ_{Sv_y}, λ_{Sr}, $\lambda_{Sr=v_y}$, and $\lambda_{Sr=-v_y}$, an arbitrary initial condition $(0.5, 0.1)$ is selected. By running the algorithm up to the 4096 seconds with the step size $\tau = 0.01\ s$, the modified Lyapunov exponents corresponding

to the selected directions converge to the values of $\lambda_{Sv_y} = -4.0425$, $\lambda_{Sr} = -4.2113$, $\lambda_{Sr=v_y} = -13.2578$, and $\lambda_{Sr=-v_y} = +5.0039$. The time histories of these modified Lyapunov exponents are shown in Figure 4.19.

Again, to show that the modified Lyapunov exponents are independent of the selected initial conditions, the values of the modified Lyapunov exponents for different initial conditions have been computed. Table 4.5 demonstrates three sets of those initial conditions. It can be seen that regardless of the starting point the corresponded modified Lyapunov exponents converge to the same values.

Table 4.5: Modified Lyapunov exponents computed for three different initial conditions of the single-track vehicle model in the steady-state cornering with $\delta_f = 5^o$ and $v_x = 20\ ^m/_s$

Initial conditions, $(v_y(0), r(0))$	λ_{Sv_y}	λ_{Sr}	$\lambda_{Sr=v_y}$	$\lambda_{Sr=-v_y}$
$(0.5, 0.1)$	-4.04250	-4.21129	-13.25776	$+5.00396$
$(1, -0.5)$	-4.04252	-4.21130	-13.25779	$+5.00397$
$(-0.5, 0.3)$	-4.04248	-4.21127	-13.25776	$+5.00398$

4.5 Summary

In this chapter, the conventional Lyapunov exponents have been modified, which can reveal the average exponential divergent or convergent rate in specific directions that are driven by the dynamics in the corresponding directions. The existence and invariance of the proposed exponents have been proven rigorously. Note that although the proof, i.e., defining an ergodic probability measure, is restricted to the system with

an equilibrium point or an attracting limit cycle, the Haar measure [58] can be used directly for the proof of systems with quasiperiodic attractors. However, to extend the proof to chaotic systems, a new ergodic probability measure must be proposed, which is a well-known challenging problem and is outside the scope of this work.

An algorithm for calculating the modified Lyapunov exponents has also been developed. Various case studies have been presented to demonstrate the modified exponents. Through the case studies, the indications of the modified Lyapunov exponents have been explored. It was also demonstrated that the previous work on conditional Lyapunov exponents of sub-dynamic systems [4, 36] are special cases of the modified Lyapunov exponents proposed here.

Although the research is in its infancy, it has great potential for nonlinear system analysis and stability control. The proposed modified Lyapunov exponents can provide insights into nonlinear dynamics additional to those from conventional exponents, such as the asymptotic behaviours along specific directions, which are driven by the dynamics in the corresponding directions. The modified exponents can contribute to the identification of the dominant sub-systems, as discussed in the case studies. The information about the dominant sub-systems can be crucial for stability or chaotic control design [36]. Successful identification of dominant sub-systems can also be used to reduce the computational load required for calculating Lyapunov exponents [4].

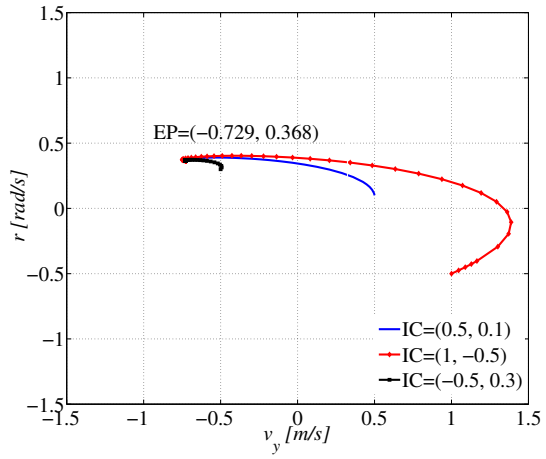

Figure 4.17: Phase portrait for the single-track vehicle model in steady-state cornering with $\delta_f = 5^o$ and $v_x = 20\ ^m/_s$, for four different initial conditions

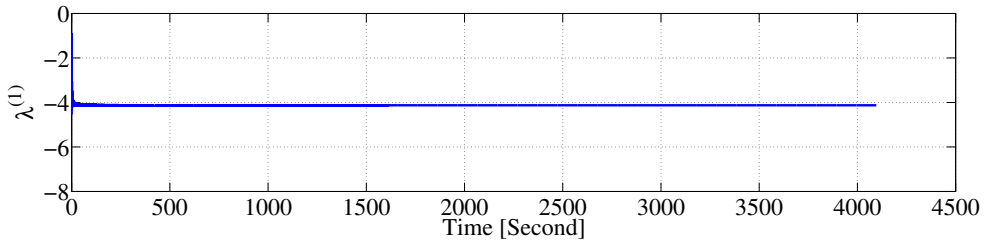

(a)

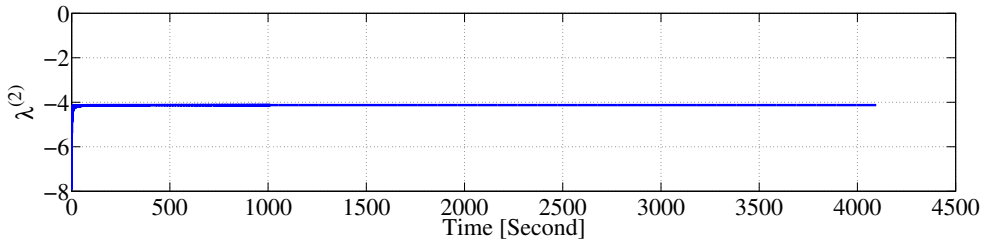

(b)

Figure 4.18: Evolution of the Lyapunov exponents, (a) $\lambda^{(1)}$ and (b) $\lambda^{(2)}$, for single-track vehicle model in the steady-state cornering with $\delta_f = 5^o$ and $v_x = 20\ ^m/_s$

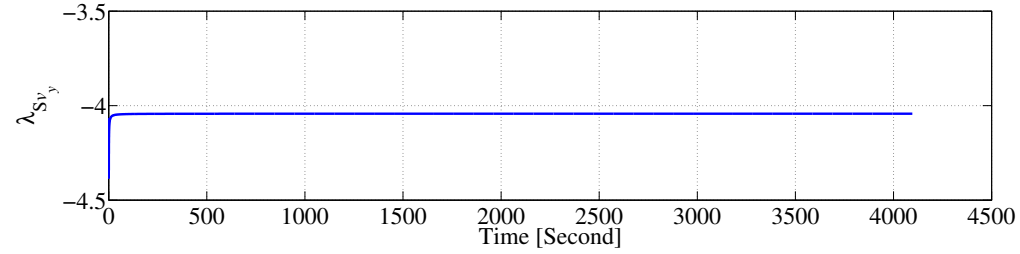

(a)

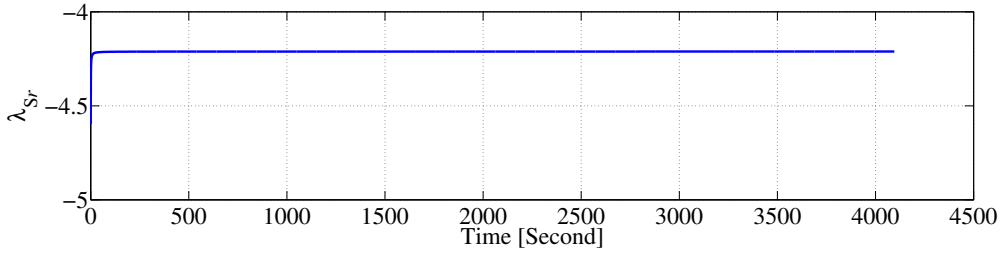

(b)

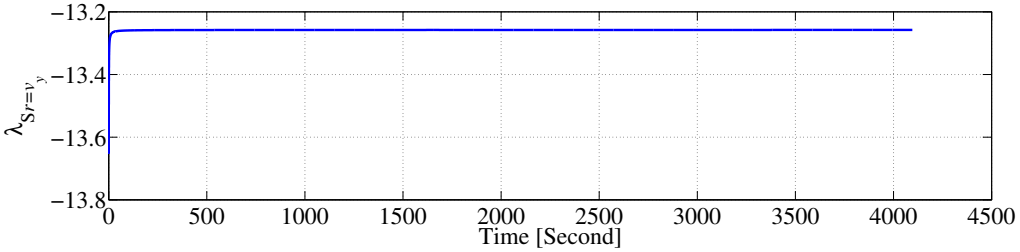

(c)

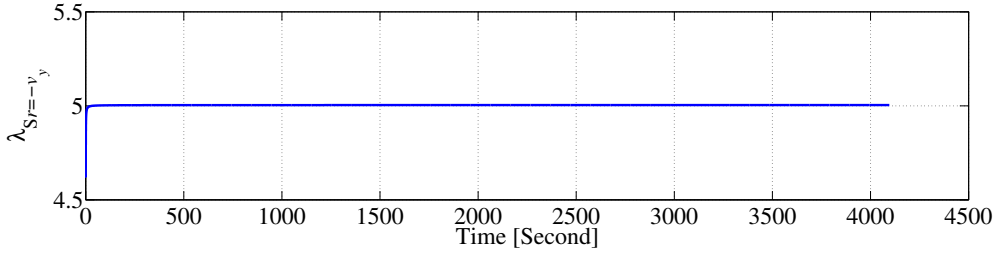

(d)

Figure 4.19: Evolution of the modified Lyapunov exponent for single-track vehicle model in the steady-state cornering with $\delta_f = 5^o$ and $v_x = 20\ ^m/_s$ for (a) λ_{Sv_y}, (b) λ_{Sr}, (c) $\lambda_{Sr=v_y}$, and (d) $\lambda_{Sr=-v_y}$

Chapter 5

Lyapunov Stability Analysis of the Vehicle Model in Plane Motion

5.1 Overview

In this chapter[1], by imposing the disturbance to the initial conditions, the concept of Lyapunov exponents is employed to investigate the system stability of the disturbed vehicle model reviewed in Section 3.3.2. After simplifying the vehicle model in Section 5.2, the stability of the vehicle model in the straight-line motion when $v_x = 20^{\mathrm{m}}/_{\mathrm{s}}$ is discussed in Section 5.3 followed by estimating the phase-space stability region in which the vehicle model remains stable by the Lyapunov's second method in Section 5.3.1 and the concept of Lyapunov exponents in Section 5.3.2. Then, in Section 5.4, the effects of driving conditions such as the longitudinal velocity, road friction coefficient, and steering angle on the stability regions are investigated.

[1]Results of this chapter are published in [63–65].

5.2 Bicycle Vehicle Model

In this study, the well-known bicycle vehicle model, introduced in Section 3.3.2, with 2-DOF (the yaw rate and the lateral velocity) and the nonlinear tire forces are considered. The dynamic equations based on the lateral speed, v_y, and the yaw rate, r, have been represented from Eq. 3.43 in Section 3.3.2 as

$$\begin{cases} \dot{v}_y = \frac{1}{m}\left(2\ F_{yf}\cos\delta_f + 2\ F_{yr}\right) - v_x r \\ \\ \dot{r} = \frac{1}{I_z}\left(2\ l_f F_{yf}\cos\delta_f - 2\ l_r F_{yr}\right) \end{cases} \tag{5.1}$$

The following assumptions are made to the vehicle model of this study:

- The vehicle lateral speed, v_y, and the yaw rate, r, are relatively small in comparison with the vehicle longitudinal velocity, v_x [8]. Thus, the linear relationship among the tire sideslip angles, lateral velocity, and yaw rate as given in Eq. 5.2 and Eq. 5.3 is valid for the front and the rear axels.

$$\alpha_f = \tan^{-1}\left(\frac{v_y + l_f r}{v_x}\right) - \delta_f \approx \frac{v_y + l_f r}{v_x} - \delta_f \tag{5.2}$$

$$\alpha_r = \tan^{-1}\left(\frac{v_y - l_r r}{v_x}\right) \approx \frac{v_y - l_r r}{v_x} \tag{5.3}$$

- The front and the rear sideslip angles, α_f and α_r , are small enough that the nonlinear behaviour of the tire lateral force can be expressed by the third-order polynomial tire model [43, 44]. Therefore, the tire lateral force for the front and the rear axles is related to the corresponding tire sideslips as given in Eq. 5.4 and Eq. 5.5 as

$$F_{yf} = -C_{\alpha f}\left(\alpha_f - k_f\alpha_f^3\right) \tag{5.4}$$

$$F_{yr} = -C_{\alpha r}\left(\alpha_r - k_r\alpha_r^3\right) \tag{5.5}$$

where k_f and k_r are parameters associated with the nonlinear dependence of the lateral force to the sideslip angle for the front and the rear tires [43, 44].

When Eq. 5.2 to Eq. 5.5 are combined with Eq. 5.1, the governing nonlinear equations of the vehicle model can be rewritten as

$$\begin{cases} \dot{v}_y = \dfrac{-2C_{\alpha f}\cos\left(\delta_f\right)\left[\left(v_y+l_f r\right)/v_x-\delta_f\right]\left(1+k_f\left[\left(v_y+l_f r\right)/v_x-\delta_f\right]^2\right)}{m} \\ \qquad\qquad -\dfrac{2C_{\alpha r}\left[\left(v_y-l_r r\right)/v_x\right]\left(1+k_r\left[\left(v_y-l_r r\right)/v_x\right]^2\right)}{m} - v_x r \\ \dot{r} = \dfrac{-2C_{\alpha f}l_f\cos\left(\delta_f\right)\left[\left(v_y+l_f r\right)/v_x-\delta_f\right]\left(1+k_f\left[\left(v_y+l_f r\right)/v_x-\delta_f\right]^2\right)}{I_z} \\ \qquad\qquad +\dfrac{2C_{\alpha r}l_r\left[\left(v_y-l_r r\right)/v_x\right]\left(1+k_r\left[\left(v_y-l_r r\right)/v_x\right]^2\right)}{m} \end{cases} \tag{5.6}$$

This vehicle model is a nonlinear system. The stability properties of the vehicle model governed by Eq. 5.6 with parameter values of a full-size American automobile [43, 44], given in Table 5.1, proceed in the following sections.

Table 5.1: Vehicle model parameters

Parameter	Value
$C_{\alpha f}$	57300 $^{\mathrm{N}}/_{\mathrm{rad}}$
$C_{\alpha r}$	57300 $^{\mathrm{N}}/_{\mathrm{rad}}$
k_f	4.87
k_r	4.87
I_z	6550 $kg.m^2$
m	2527 kg
l_f	1.37 m
l_r	1.86 m

5.3 Stability Analysis of the Vehicle Model in Straight-line Motion

Equations of the straight-line motion of the vehicle model, given in Eq. 5.7, can be attained by substituting $\delta_f = 0^o$ into Eq. 5.6.

$$\begin{cases} \dot{v}_y = \dfrac{-2C_{\alpha f}\left[\left(v_y+l_f r\right)/v_x\right]\left(1+k_f\left[\left(v_y+l_f r\right)/v_x\right]^2\right)}{m} \\ \qquad -\dfrac{2C_{\alpha r}\left[\left(v_y-l_r r\right)/v_x\right]\left(1+k_r\left[\left(v_y-l_r r\right)/v_x\right]^2\right)}{m} - v_x r \\ \dot{r} = \dfrac{-2C_{\alpha f} l_f\left[\left(v_y+l_f r\right)/v_x\right]\left(1+k_f\left[\left(v_y+l_f r\right)/v_x\right]^2\right)}{I_z} \\ \qquad +\dfrac{2C_{\alpha r} l_r\left[\left(v_y-l_r r\right)/v_x\right]\left(1+k_r\left[\left(v_y-l_r r\right)/v_x\right]^2\right)}{m} \end{cases} \tag{5.7}$$

The Lyapunov's stability analysis of a non-linear dynamic system should start with obtaining equilibrium points. Recalling the method from [43], in which the non-linear equations $\dot{v}_y = 0$ and $\dot{r} = 0$ have been solved simultaneously, five equilibrium points are given in Table 5.2. Since in the straight-line motion any non-zero steady-state

values for yaw rate and lateral velocity are meaningless, the stability analyses of the non-zero equilibrium points are omitted and only the stability of the equilibrium point located at the origin is discussed.

Table 5.2: Equilibrium points of the vehicle model

Equilibrium point	$(v_y,\, r)$
1	(0, 0)
2	(−6.02, 0.68)
3	(6.02, −0.68)
4	(−9.06, 0)
5	(9.06, 0)

5.3.1 Stability Analysis of the Vehicle Model in the Straight-line Motion by Lyapunov's Direct Method

The Lyapunov's direct method has a great potential to analyze non-linear systems. In this part, this method will be applied to analyze the vehicle lateral stability in a straight-line motion with constant longitudinal velocity. Finding a Lyapunov function is always a difficult task and sometimes impossible. To construct a new Lyapunov function, a modified kinetic energy function recalled from [44] is considered as an initial guess. For the vehicle model with parameters in Table 5.1, this function is expressed in Eq. 5.8.

$$V_1 = 0.0265v_y^2 + 1.1664r^2 \tag{5.8}$$

The largest possible stability boundary corresponding to Eq. 5.8 is depicted by the green ellipse in Figure 5.1. The position of the equilibrium points in the phase plane

is indicated by cross symbols. In Figure 5.1, since two equilibrium points (numbers 2 and 3) are close to the stability boundary, it seems impossible to find a bigger stability region based on the same form of the V_1 function. On the other hand, if the ellipse rotates counter clockwise to get far from these two equilibrium points, the expansion of the stable area appears to be possible. This rotation can be achieved by adding a factor of vr term in Eq. 5.8. After some trial and error on selecting the coefficients, the proposed Lyapunov function candidate, expressed in Eq. 5.9, is obtained.

$$V_2 = \frac{1}{16}v_y^2 - \frac{1}{4}v_y r + r^2 \tag{5.9}$$

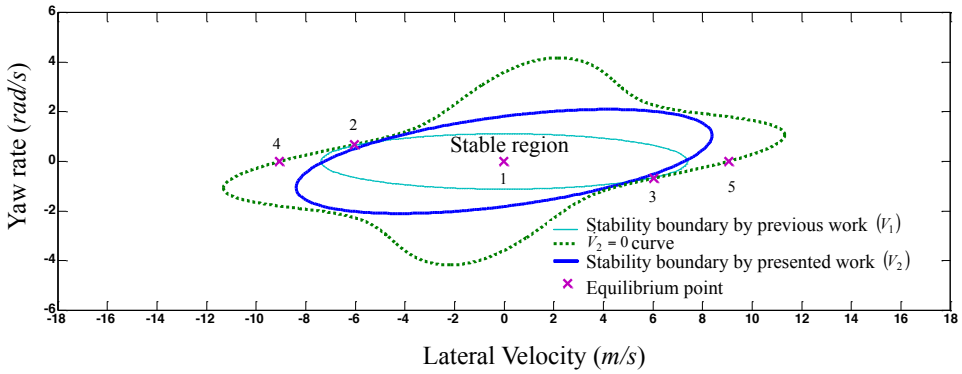

Figure 5.1: Comparison of stability region correspond to V_1 and V_2

Equation 5.10 presents a quadratic expression of Eq. 5.9. Since the coefficient matrix $\mathbf{P}$ is a positive definite, V_2 is positive definite and satisfies the first condition for a Lyapunov function.

$$V_2 = \mathbf{X}^T\mathbf{P}\mathbf{X} = \begin{bmatrix} v_y \\ r \end{bmatrix} \begin{bmatrix} \frac{1}{15} & -\frac{1}{8} \\ -\frac{1}{8} & 1 \end{bmatrix} \begin{bmatrix} v_y & r \end{bmatrix} \tag{5.10}$$

The time derivative of V_2 is given by

$$\dot{V}_2 = \dot{\mathbf{X}}^T\mathbf{P}\mathbf{X} + \mathbf{X}^T\mathbf{P}\dot{\mathbf{X}} \tag{5.11}$$

The method implemented in [43] is used here to find the border of the region in which $\dot{V}_2$ is negative definite. This border is shown by dotted line in Figure 5.1. It shows that the second condition for a Lyapunov function is satisfied inside the dotted border. Then, the largest stable region corresponding to proposed Lyapunov function in Eq. 5.9 can be found by fitting the largest $V_2 = cte$ inside the $\dot{V}_2 < 0$ area as illustrated by the blue ellipse in Figure 5.1.

The stability region associated with the proposed Lyapunov function is larger than those proposed in [43] and [44]. A larger stability region is achieved because the proposed Lyapunov function is not explicitly a function of the vehicle parameters. Thus, unlike previous works [43, 44], it is possible to estimate a larger stability region by modifying the Lyapunov function coefficients.

The interpretation of the stability region in Figure 5.1 is that if the states of the disturbed vehicle model remain inside this area, it will certainly return to the steady-state situation. If the disturbed vehicle model goes outside of the stability region, no conclusion can be made.

In fact, the exact vehicle stability region is ideally demanded for vehicle stability analysis. In this regard, the fundamental advantage of applying Lyapunov's direct method arises from the fact that the Lyapunov function is an 'invariant' measure of the stability. For example, it is independent of initial conditions, i.e., there is no need to solve the system equations. On the other hand, when Lyapunov's direct method is

applied to the stability analysis of a dynamical system, there is no guaranty to find a Lyapunov function. Furthermore, if a Lyapunov function is hopefully obtained, the size of the associated stability region is dominated by that Lyapunov function, and it is always just a fraction of the overall stability region. The absence of the constructive technique to find a Lyapunov function makes it extremely difficult to apply Lyapunov's direct method to complex vehicle models. Therefore, researchers are forced to simplify the models in order to derive a Lyapunov function. These simplifications restrict the validation of a model for some critical maneuvers. For examples, the constant longitudinal velocity is valid only for low-lateral acceleration maneuvers; during high-lateral acceleration maneuvers, due to the extreme yaw rate, the desired vehicle speed may not be achievable even with full throttle [39]. The tire sideslip approximation is only valid for high longitudinal velocity and the third-order tire polynomial model is not valid for the range of large tire slip [40]. Moreover, Lyapunov's direct method is only feasible for lateral stability analysis of the vehicle in a simple straight-line motion, but the lateral stability of the vehicle during cornering is more crucial. Therefore, a constructive 'invariant' measure of the stability for more realistic vehicle models and more critical maneuvers would be important and challenging and will be studied in future.

5.3.2 Stability Analysis of the Vehicle Model in Straight-line Motion by the Concept of Lyapunov Exponents

Since the nonlinear equations describing the vehicle model have two states, two Lyapunov exponents exist. For calculating these two Lyapunov exponents, the initial

conditions are chosen as $r_0 = 0.1^{\mathrm{rad}}/_{\mathrm{s}}$ and $v_{y_0} = 1^{\mathrm{m}}/_{\mathrm{s}}$. Selecting the time-step size τ to be $0.001s$ and iterating the standard method $100,000$ times, the first exponent converges to -6.616 and the second one converges to -6.661. Here, it is considered that the convergent exponent is achieved if the change in the numerical values of the exponent between the two subsequent steps is within 10^{-3}. The time history of these exponents is illustrated in Figure 5.2. All negative exponents indicate that the vehicle model is exponentially stable about the origin equilibrium. Figure 5.3 displays the system trajectory in the phase plane for the given initial conditions. It shows how the states of the vehicle model converge to the stable fixed point at the origin of the phase plane. The time evaluations of the system states are also shown in Figure 5.4. It can be seen that both states approach to zero since the system is stable.

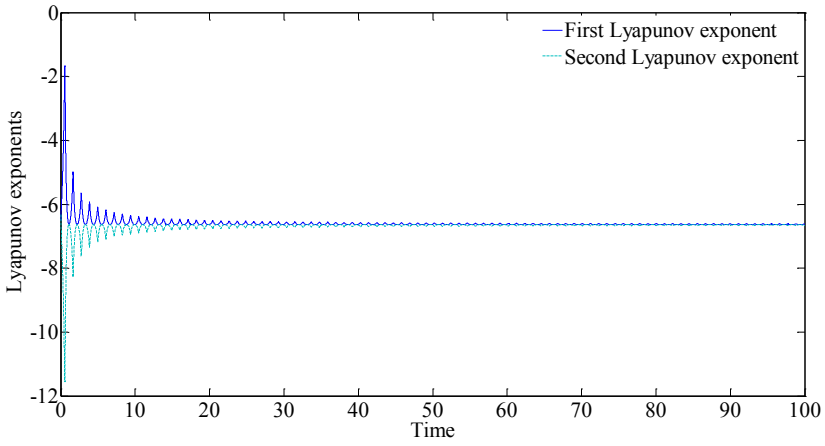

Figure 5.2: Vehicle model Lyapunov exponents in the straight-line motion

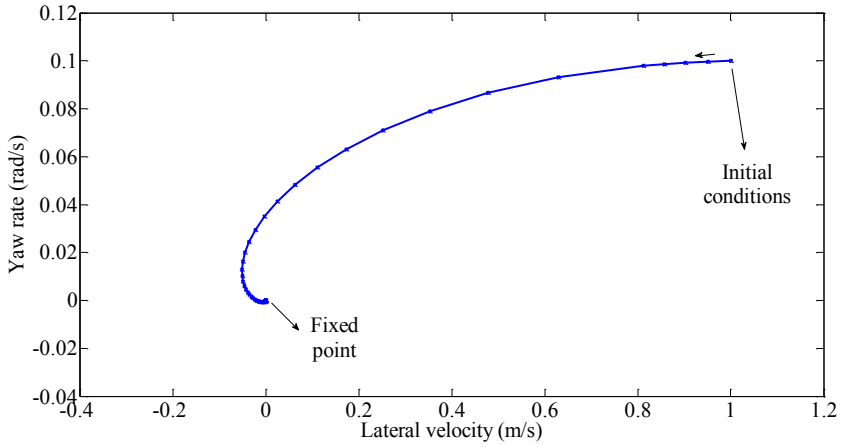

Figure 5.3: Vehicle model trajectory for initial conditions $r_0 = 0.1\,^{\mathrm{rad}}/_{\mathrm{s}}$ and $v_{y_0} = 1^{\mathrm{m}}/_{\mathrm{s}}$

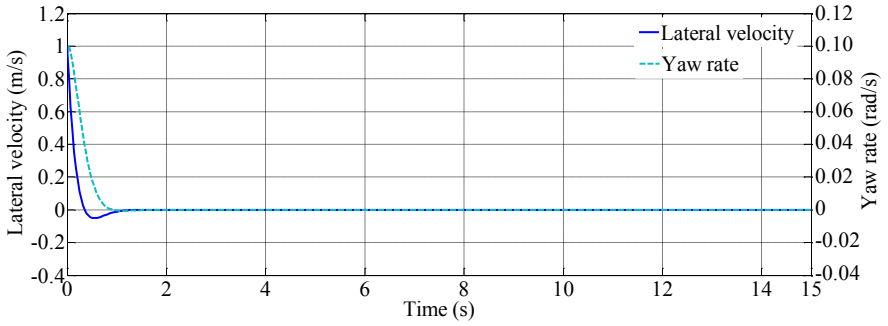

Figure 5.4: Time evolution of the states of the disturbed vehicle model in the straight-line motion

Lateral stability region of the vehicle model in a straight-line motion

For all trajectories starting from arbitrary initial conditions in the same stability domain, the Lyapunov exponents have the same values [29]. This property makes it possible to estimate the stability region. To estimate such a stability region, the $v_y - r$ phase-plane is meshed into small areas. The size of each area is $0.05^{\mathrm{m}}/_{\mathrm{s}} \times 0.05^{\mathrm{rad}}/_{\mathrm{s}}$. Then, the Lyapunov exponents of an arbitrary point in each segment are calculated. The union of those areas that have the same negative exponents constructs the lateral

stability region [66]. The boundary of the estimated stability region, found by this method, is illustrated by the blue curve in Figure 5.5. For each disturbance inside this border, the vehicle model is exponentially stable and will return to its stable fixed point. The boundary of the lateral stability region given by the proposed Lyapunov function in Section 5.3.1 is also shown by the green curve in Figure 5.5. This is the largest lateral stability region found by the Lyapunov's direct method for this particular vehicle model. In the case of Lyapunov's direct method, the size of the stability region is dictated by the specific Lyapunov function, and it is often just the fraction of the overall stability region. For this particular vehicle model, it is quite obvious that the stability boundary extracted by the Lyapunov function is only a portion of the stability region found by the concept of Lyapunov exponents. Here, the lateral stability region which has been obtained by the concept of Lyapunov exponents overlaps with the complete lateral stability region found by the simulation in [43]. For each initial condition outside this area, the calculation of the Lyapunov exponents failed since the solution of the equations approaches infinity. This is the interpretation of the fact that for disturbances outside of this region, the assumption of the constant longitudinal velocity cannot be satisfied even with full throttle as discussed in [39].

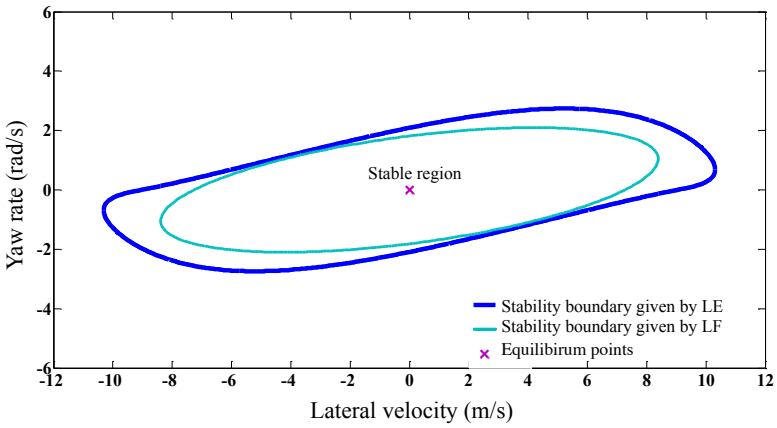

Figure 5.5: Lateral stability region of the vehicle model in the straight-line motion

5.4 Investigating the Effects of Driving Conditions on the Lateral Stability Region Using the Concept of Lyapunov Exponents

The lateral stability region of the vehicle model can be deformed due to the vehicle characteristics such as weight disturbance and driving conditions. Since the effect of driving conditions on the lateral stability region is significant [40], in this subsection the effects of these conditions on the lateral stability region are presented separately.

5.4.1 Effects of the Longitudinal Velocity on the Lateral Stability Region

To investigate the effect of the longitudinal velocity on the stability region, the vehicle model in (Eq. 5.6) is supposed to be driven on a straight-line on a dry road ($\mu = 1$)

at different constant longitudinal velocities. The lateral stability regions for different constant velocities are illustrated in Figure 5.6. The longitudinal velocities between $15^{m}/_{s}$ to $50^{m}/_{s}$ are marked on the vertical axis, and their associated lateral stability regions are shown by colourful regions from blue to green. For better demonstration, the projection of the lateral stability regions on planes A, B, and C are also illustrated (see Figure 5.6). As the value of the longitudinal velocity increases, the stability region starts to expand in the lateral velocity direction (see plane C) and to shrink in the direction of the yaw rate (see plane B). This means the vehicle model is less robust to the yaw rate if it is driven at a high constant longitudinal velocity. It can also be seen that the value of the longitudinal velocity does not affect the position of the equilibrium point in the phase plane of the vehicle model.

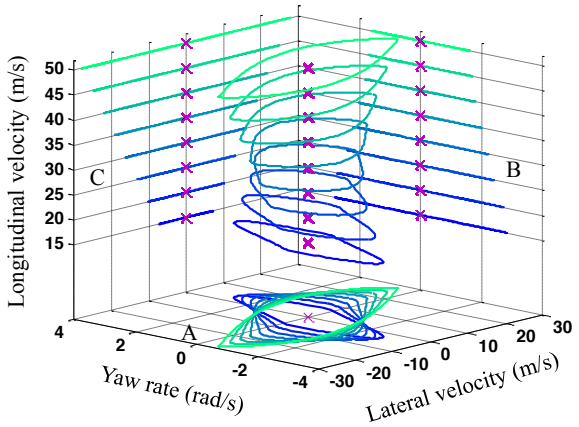

Figure 5.6: Effects of the longitudinal velocity, v_x, on the lateral stability region

5.4.2 Effects of the Road Friction Coefficient on the Lateral Stability Region

Since the vehicle moves due to the tractive force between the road and the tires, the friction coefficient of the ground contact point plays an important role in its lateral stability. The lateral force between the tires and the road can be formulated as the multiplication of the tire normal load and the coefficient of the friction ($F_y = \mu N$). Therefore, the coefficient of the friction has direct relation with the tire lateral force. To investigate how the coefficient of the friction can change the lateral stability region, the vehicle model is driven on a straight-line at the constant longitudinal velocity ($v_x = 20\,{}^{\mathrm{m}}\!/_{\mathrm{s}}$) with the friction coefficient in the range of 0.1 to 1.

In Figure 5.7, the lateral stability regions associated with different road friction coefficients, shown in the vertical direction, are depicted. The colour changes from blue to green as the road friction increases. The effects of the friction coefficient on lateral stability regions in the direction of the yaw-rate and the lateral velocity are shown by projections of the lateral stability regions on planes B and C, respectively. It can be found that the stability region mostly shrinks in the direction of the yaw rate (see the plane B) due to the decrease in the friction coefficient. On the other hand, the lateral stability region seems to be insensitive in the direction of the lateral velocity by the changes in the friction coefficient (see plane C). It can also be observed that like the longitudinal velocity case, the coefficient of the friction does not change the location of the stable equilibrium point on the vehicle model phase plane.

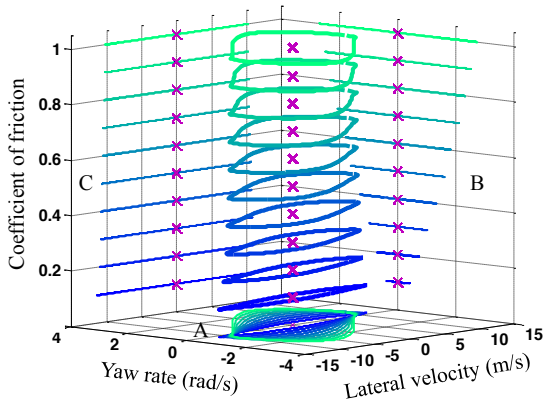

Figure 5.7: Effects of the friction coefficient between tires and ground, μ, on the lateral stability region

5.4.3 Effects of the Steering Angle on the Lateral Stability Region

In this case, the vehicle model is driven at the constant longitudinal velocity ($v_x = 20\,{}^{\mathrm{m}}/_{\mathrm{s}}$) around dry circular tracks ($\mu = 1$) with different curvatures. Since the vehicle model moves along a curve, at the steady-state condition, the lateral velocity and yaw rate are non-zero. Therefore, unlike the two other driving conditions, the steering angle input changes the position of the equilibrium point on the phase plane. In Figure 5.8, the lateral stability regions for positive and negative steering angles, indicated on the vertical axis, are shown. For better illustration, the projections of these lateral stability regions on planes A, B, and C are also demonstrated. It can be realized (see planes B and C) that the lateral stability regions start to shrink as the steering angle becomes larger. Furthermore, the stable equilibrium point moves to the boundary (see planes B and C) as the value of the steering angle increases. It means that the

vehicle model is generally less robust to the disturbance when it is driven on a sharp circular path.

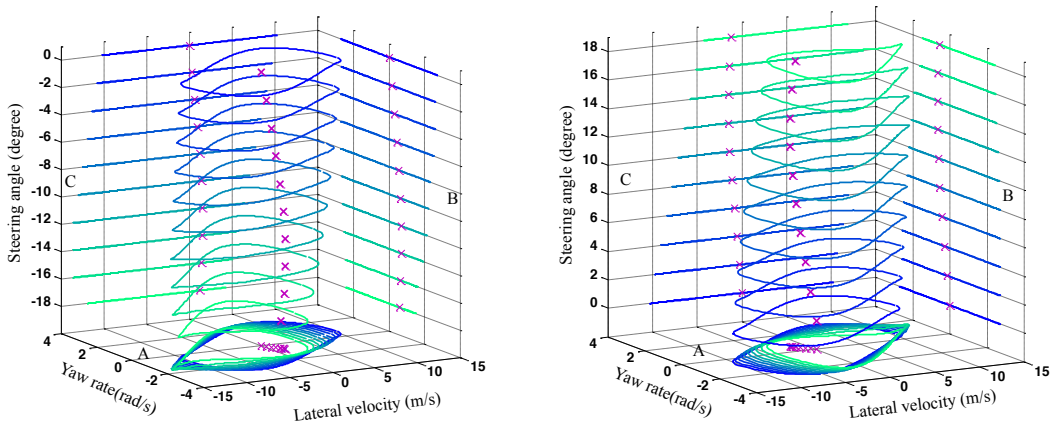

(a) (b)

Figure 5.8: Effects of the steering angle, δ_f, on the stability region, (a) negative steer angles, and (b) positive steer angles

5.5 Structural Stability Analysis of the Vehicle Model

Structural stability is another important property of a dynamic system. In this section, the above driving conditions are treated as system parameters and are disturbed. The stability region associated with the vehicle model parameters is given in Figure 5.5.1. In Section 5.5.2, the largest Lyapunov exponent of the vehicle model is used to investigating the convergence rate of the disturbed vehicle model to its stable condition.

5.5.1 Stability Region of the Vehicle Model

The stability region gives the ranges of the system parameters in which the stability of the vehicle model is guaranteed. As long as the largest Lyapunov exponent is negative, the system is exponentially stable. Therefore, the sign of the largest Lyapunov exponent is the key to investigate the structural stability of a system.

To find the ranges of the driving conditions in which the stability of the vehicle model is guaranteed, the largest Lyapunov exponent for different vehicle parameters is calculated. Figure 5.9 shows part of the stability region. Here, it is supposed that the steering angle, longitudinal velocity and road friction coefficient vary from -18^o to 18^o, $15\,\mathrm{m/s}$ to $50\,\mathrm{m/s}$, and 1 to 0.1, respectively. The step sizes are equal to 0.5^o for the steering angle, $1\,\mathrm{m/s}$ for the longitudinal velocity, and -0.05 for the coefficient of friction. From Figure 5.9, it can be found that if the vehicle is driven in conditions belong to this stability region, the largest Lyapunov exponent is negative and the vehicle model is exponentially stable. The colourful map in Figure 5.9 shows how the absolute value of the largest Lyapunov exponents decreases as the driving conditions approach to the edges. Figure 5.9 only shows part of the stability region. Determining the entire stability region is important, but beyond the scope of this work.

5.5.2 Largest Lyapunov Exponent as Convergence Rate of the Disturbed Vehicle Model to its Stable Fixed Point

The sum of the Lyapunov exponents indicates the time-averaged divergence of the phase space velocity for a dynamic system [30]. Thus, the value of the largest Lya-

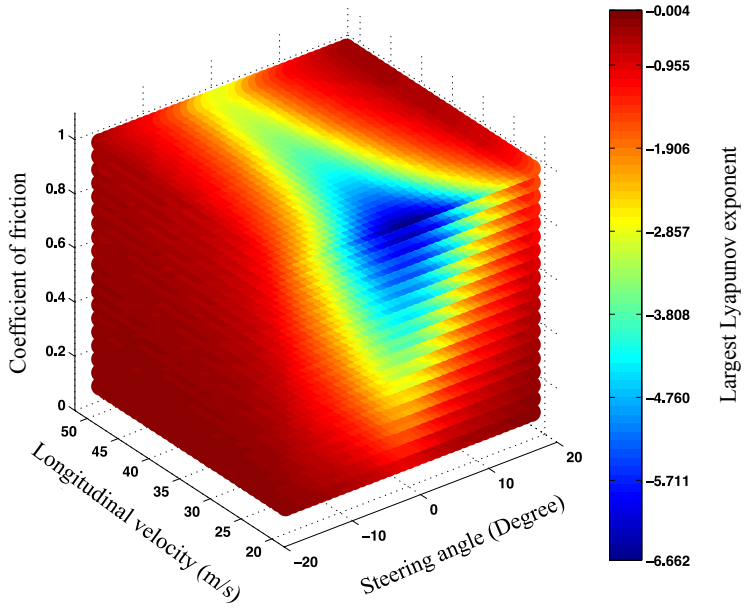

Figure 5.9: Stability region of the vehicle model

punov exponent for a dynamic system with all negative Lyapunov exponents is a qualitative measurement for the convergence rate in which the disturbed system returns to its stable fixed point in the phase plane. In this section, this idea is investigated for the vehicle model.

Example 1: Disturbed Vehicle Model Convergence Rate to its Stable Fixed Point for Particular Steering Angles

In the first example, for a particular value of the steering angle, the largest Lyapunov exponent of the vehicle model with different longitudinal velocities and road friction coefficients are calculated. Figure 5.10 illustrates the bifurcation diagram of the largest Lyapunov exponent for the steering angle equal to: a) $\delta_f = 0^o$, b) $\delta_f = \pm 5^o$,

c) $\delta_f = \pm 10^o$, and d) $\delta_f = \pm 15^o$. Here, the longitudinal velocity is in the range of $15\,\mathrm{m/s}$ to $50\,\mathrm{m/s}$ with an increment of $1\,\mathrm{m/s}$ at each step. The coefficient of friction starts from 0.1, increments 0.05 until it reaches the maximum value of 1. Comparing Figures 5.10(a) to Figure 5.10(d), it can be seen that for a particular pair of the longitudinal velocity and the coefficient of friction, e.g., $v_x = 15\,\mathrm{m/s}$ and $\mu = 1$, as the steering angle increases the absolute value of the largest Lyapunov exponent decreases and therefore, the convergence rate to the stable fixed point in the phase plane will decrease.

Example 2: Disturbed Vehicle Model Convergence Rate to its Stable Fixed Point for Particular Longitudinal Velocities

In this example, for particular values of the longitudinal velocity equal to a) $v_x = 20\,\mathrm{m/s}$, b) $v_x = 30\,\mathrm{m/s}$, c) $v_x = 40\,\mathrm{m/s}$, and d) $v_x = 50\,\mathrm{m/s}$ as shown in Figure 5.11, the largest Lyapunov exponents of the vehicle model for different steering angles and road friction coefficients are calculated. In this figure, the friction coefficient is changed from 0.1 to 1 with the step size of 0.05, and the steering angle is changed from -18^o to 18^o with the step size of 0.5^o. Each Figure from 5.11(a) to 5.11(d) separately shows how the largest Lyapunov exponent varies with the steering angle or/and road friction. Comparing Figures 5.11(a) to Figure 5.11(d), it can be realized that for the same steering angle and the road friction coefficient, the disturbed vehicle model has lower convergence rate to its stable fixed point when it is driven at a higher longitudinal velocity.

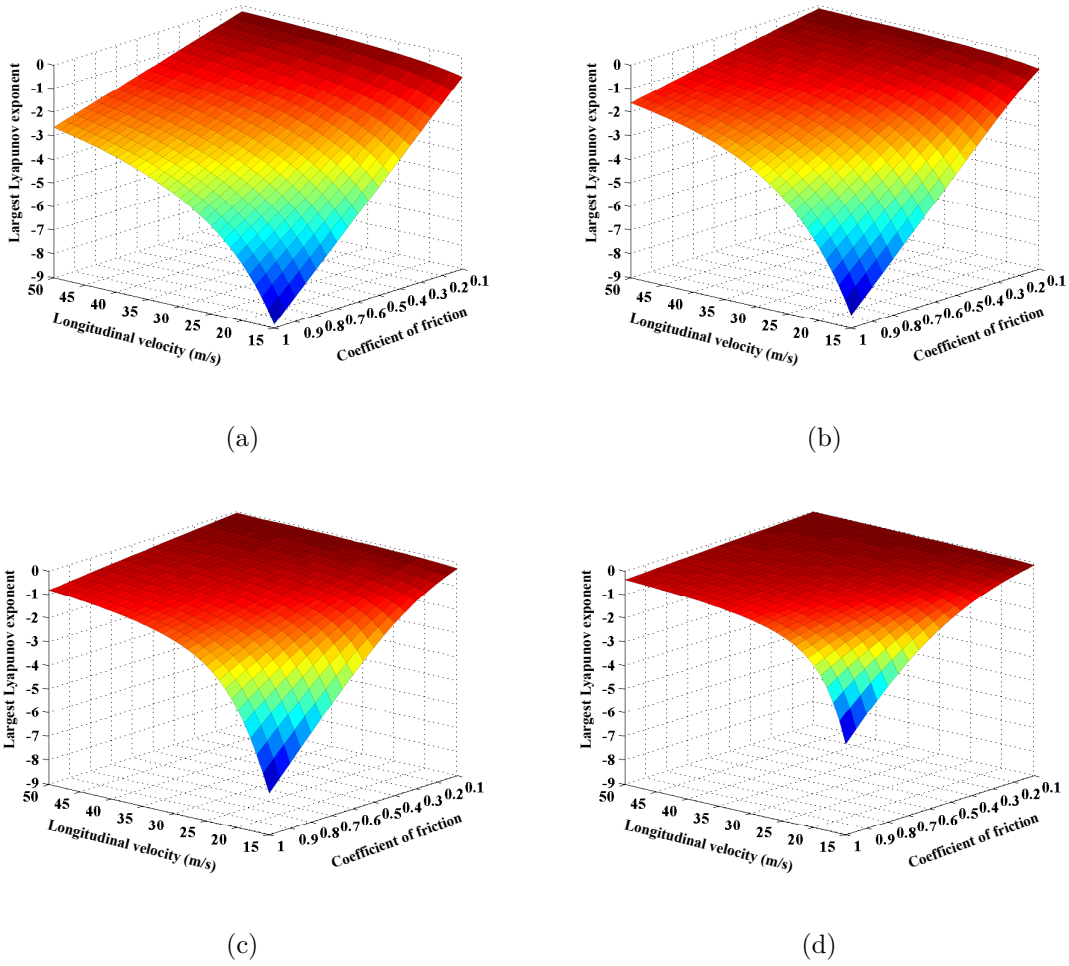

Figure 5.10: Ranges of longitudinal velocities, v_x, and friction coefficients, μ, in which the stability of the vehicle model is guaranteed while the steering angle, δ_f, is equal to (a) $\delta_f = 0^o$, (b) $\delta_f = \pm 5^o$, (c) $\delta_f = \pm 10^o$, and (d) $\delta_f = \pm 15^o$

Example 3: Disturbed Vehicle Model Convergence Rate to its Stable Fixed Point for Particular Road Friction Coefficients

To investigate the effects of the steering angle and the longitudinal velocity on the convergence rate, it is assumed that the vehicle model is driven on the road with different coefficients of friction as: a) $\mu = 1$, b) $\mu = 0.7$, c) $\mu = 0.5$, and d) $\mu = 0.3$. In Figure 5.12, the maps of the largest Lyapunov exponents in these conditions are

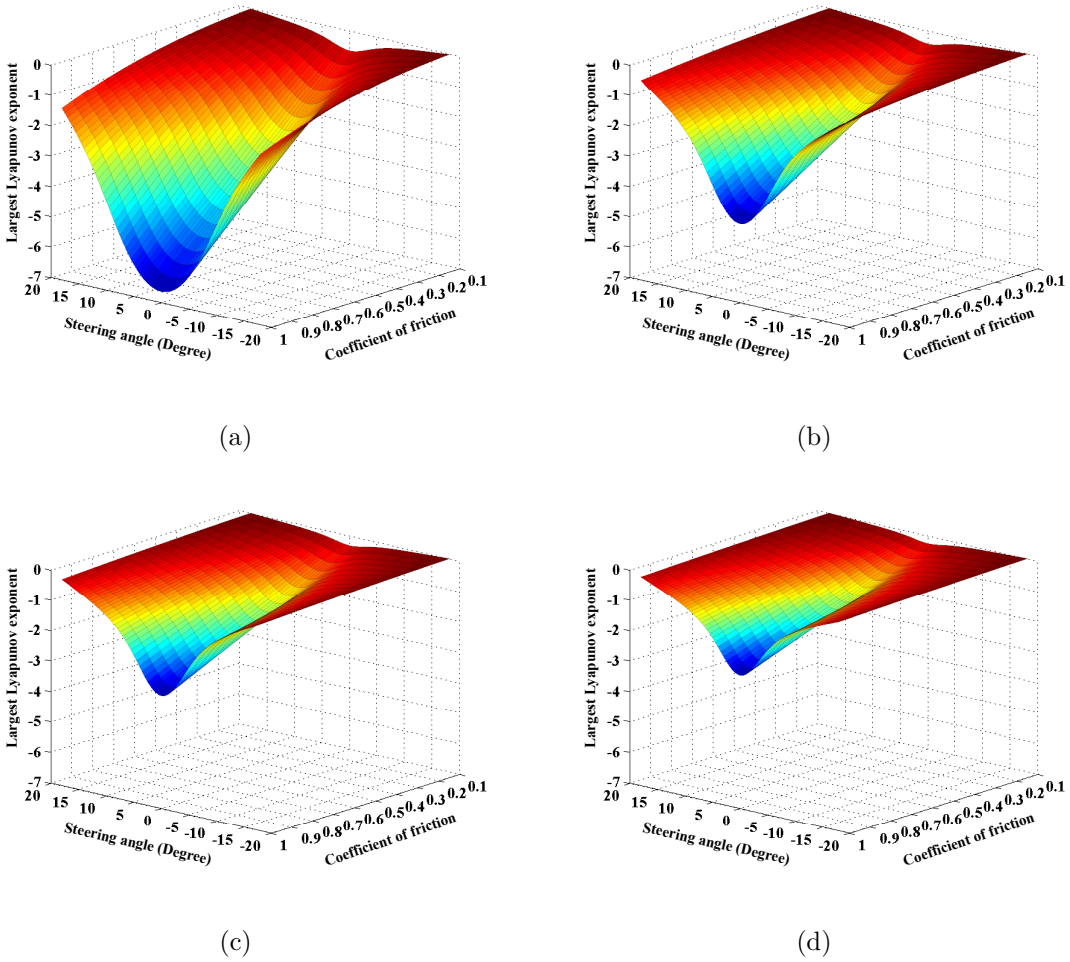

Figure 5.11: Ranges of steering angles, δ_f, and friction coefficients, μ, in which the stability of the vehicle model is guaranteed while the longitudinal velocity, v_x, is equal to: (a) $v_x = 20\,\mathrm{m/s}$, (b) $v_x = 30\,\mathrm{m/s}$, (c) $v_x = 40\,\mathrm{m/s}$, and (d) $v_x = 50\,\mathrm{m/s}$

depicted. In this figure, the steering angle and the longitudinal velocity vary from -18^o to 18^o and $15\,\mathrm{m/s}$ to $50\,\mathrm{m/s}$, respectively. The step size associated with the steering angle is 0.5^o and with the longitudinal velocity is $1\,\mathrm{m/s}$. It can be found that in each condition as the steering angle increases or longitudinal velocity increases, the absolute value of the largest Lyapunov exponents decreases and therefore, the convergence rate of the disturbed vehicle model to return to its stable fixed point will

decrease. The comparison among Figures 5.12(a) to 5.12(d) shows that for the same conditions of the steering angle and longitudinal velocity of the vehicle model, the absolute value of the largest Lyapunov exponent becomes smaller as the coefficient of friction decreases. This can be interpreted as the lower convergence rate of the disturbed vehicle model in slippery roads.

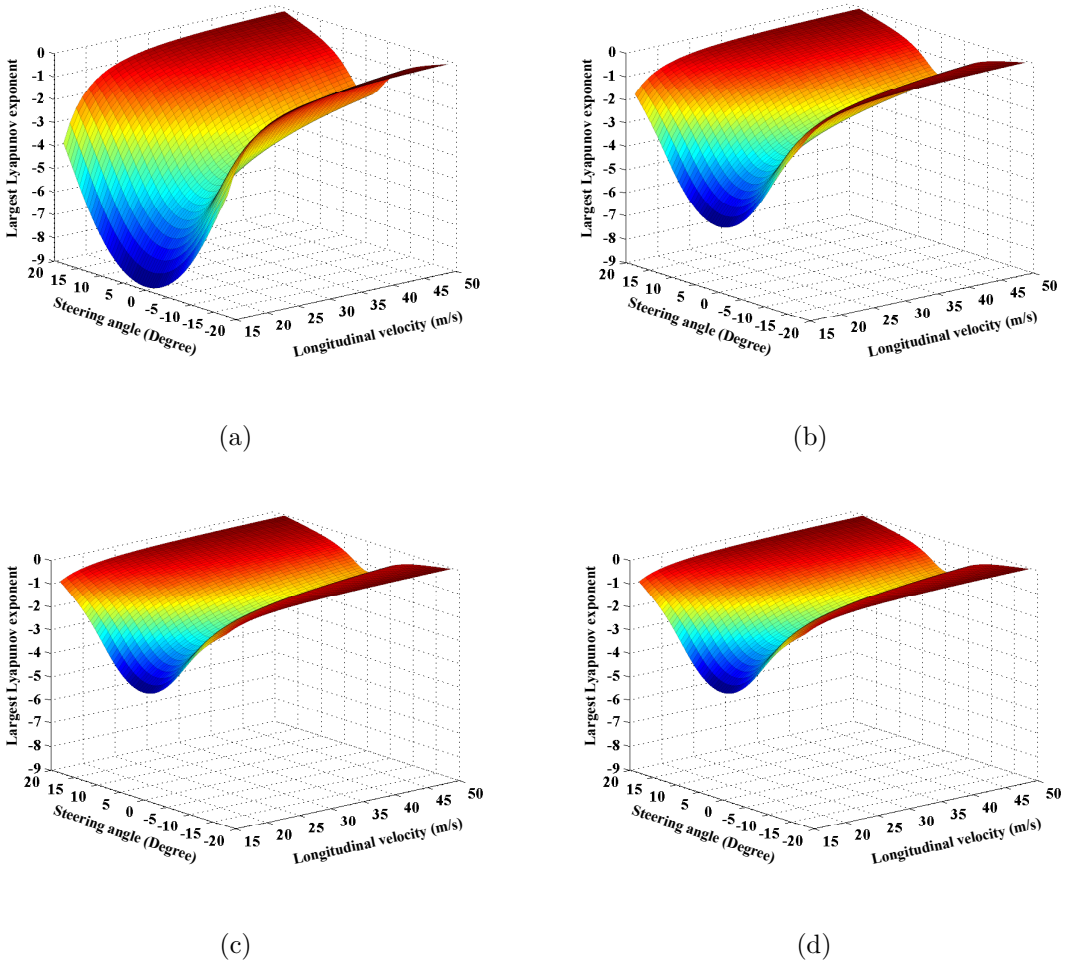

Figure 5.12: Ranges of steering angles, δ_f, and longitudinal velocity, v_x, in which the stability of the vehicle model is guaranteed while the coefficient of friction, μ, is equal to: (a) $\mu = 1$, (b) $\mu = 0.7$, (c) $\mu = 0.5$, and (d) $\mu = 0.3$

5.6 Summary

This chapter applied the concept of Lyapunov exponents for the first time to both system and structural stability analyses of a nonlinear 2-DOF vehicle model. In system stability analysis, (a) the stability of the vehicle model in the straight-line motion is investigated. (b) The lateral stability region of the vehicle model in the case of straight-line motion has been estimated. It has been shown that in this special case, the estimated lateral stability region was the largest one in comparison with those found by Lyapunov's direct method. (c) The effects of driving conditions on lateral stability regions of the vehicle model have been discussed. All results were in agreement with those in [40], which verifies the successful application of this concept in vehicle stability analysis.

In the case of structural stability analysis, the ranges of driving conditions in which the vehicle model stability is guaranteed have been found. Moreover, it has been shown that for a disturbed vehicle model, the largest Lyapunov exponent varies for different driving conditions. Therefore, the largest Lyapunov exponent can be used to investigate how fast the disturbed vehicle model in different driving conditions will return to its stable fixed point.

Chapter 6

Lyapunov Stability Analysis of a Newly Developed 4-DOF Vehicle Roll Model

6.1 Overview

In this chapter[1], the Lyapunov stability of a new nonlinear 4-degrees-of-freedom (4-DOF) roll vehicle model is analyzed. The proposed model is an adequate model for Lyapunov stability analysis with roll motion. The model is developed by decoupling the yaw and roll motions of the conventional nonlinear 14-DOF full vehicle model. The information from unmodeled yaw dynamics is fed to the nonlinear 4-DOF vehicle roll model through measured lateral acceleration. The new model benefits from less

[1]Results of this chapter are submitted for publication in [67].

dynamic complexity; however, it keeps the advantage of the roll prediction even after wheel lift-off occurs. The predicted roll behaviour by the 4-DOF vehicle roll model is compared against the nonlinear 14-DOF full vehicle model for different maneuvers. The results justify the accuracy of the new model. Moreover, the model is verified by a experimental test on a developed SETV. The results justify the accuracy of the new model.

After validation of the model, the nonlinear 4-DOF vehicle roll model is analyzed by Lyapunov's linearization and Lyapunov exponents methods. The Lyapunov's linearization method guarantees the stability of the new model for small values of the lateral acceleration while the Lyapunov exponents method detects the qualitative change in the type of the attractor for large values of the lateral acceleration. The lower dimensions, and the proven Lyapunov stability make the new model more appealing for real-world applications since the lateral acceleration can be measured through a sensor.

The remainder of this chapter is organized as follows. The dynamic equations for the nonlinear 4-DOF vehicle are derived in Section 6.2. In Section 6.3, a set of different maneuvers are designed and simulation results for the nonlinear 4-DOF vehicle roll model are compared with the nonlinear 14-DOF full vehicle model. The SETV and its different components are presented in Section 6.4. The experimental test results for a cornering maneuver are given in Section 6.5. Then, the stability analysis of the nonlinear 4-DOF vehicle model are discussed in Section 6.6. Finally, conclusions are made in Section 6.7.

6.2 Nonlinear 4-DOF Vehicle Roll Model

The dynamic equations for the nonlinear 4-DOF vehicle roll model are derived by considering the roll plane dynamics of the 14-DOF vehicle model [5]. Figure 6.1 demonstrates the schematic view of the nonlinear 4-DOF vehicle roll model. The 4 degrees of freedom are the roll rate ω_x and vertical velocity v_z of the sprung mass and the vertical velocities v_{zur} and v_{zul} of the unsprung masses on the right and left sides of the vehicle.

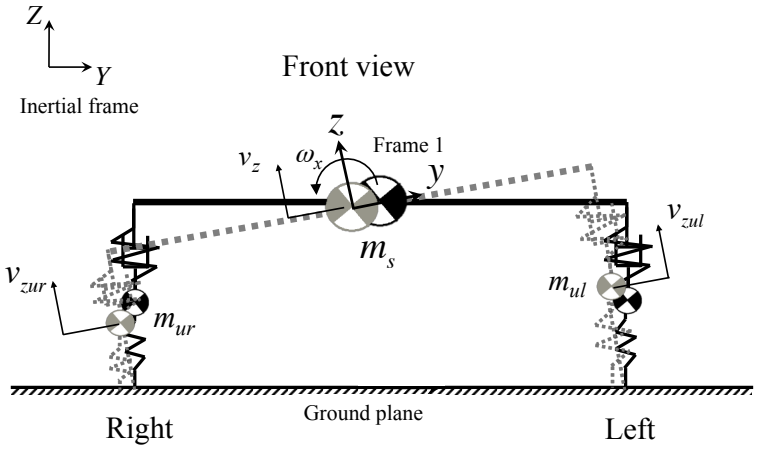

Figure 6.1: Schematic view of the nonlinear 4-DOF vehicle roll model

In order to derive the dynamic equations, in addition to the inertia frame (X, Y, Z), a fixed body coordinate located at the CG of the sprung mass (x, y, z), frame 1, is considered. Inheriting from the 14-DOF vehicle model [5], the suspensions and tires are assumed to remain at a fixed angle with respect to the sprung mass and the tire stiffnesses are considered to be perpendicular to the ground plane at all times. Moreover, without loss of generality, it is supposed that the vehicle has a

parallel horizontal link independent suspensions [7]. Therefore, the roll centre is in the ground plane when the vehicle is at rest.

Figure 6.2 illustrates the free body diagram for the unsprung mass in the right corner of the vehicle. The lateral force at the tire contact patch is F_{Yr} of the right side of the vehicle. The centrifugal force $W_{ur}a_y$ is acting on the CG of the unsprung mass as the result of the curvilinear motion.

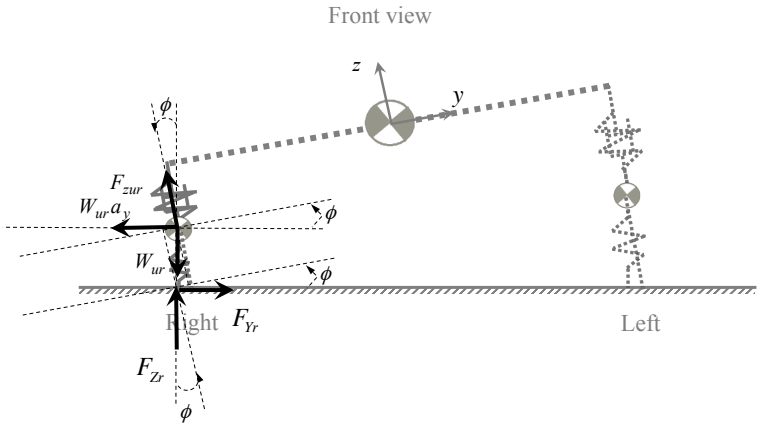

Figure 6.2: Free body diagram of the unsprung mass at the right corner of the vehicle

The dynamic equation governing the vertical motion of the unsprung mass at the right corner of the vehicle can be found as

$$\dot{v}_{zur} = \frac{1}{m_{ur}} \left(F_{zur} - W_{ur} a_y \sin(\phi) - W_{ur} \cos(\phi) + F_{Zr} \cos(\phi) - F_{Yr} \sin(\phi) \right) - \omega_x v_{yur} \tag{6.1}$$

The vertical force F_{zur} is in equilibrium with the right suspension force F_{zsr}, therefore

$$F_{zur} = -\left(b_{sr} \dot{x}_{sr} + k_{sr} x_{sr} \right) \tag{6.2}$$

The suspension deflection x_{sr} as shown in Figure 6.3 is measured from the sprung

mass level, and it is positive when the suspension is under compression.

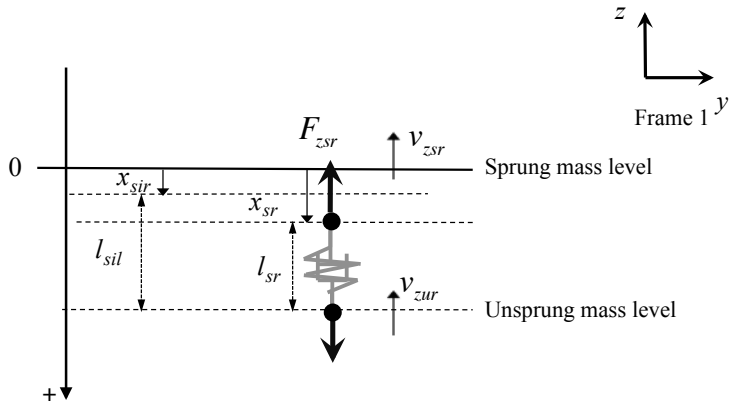

Figure 6.3: Suspension deflection measurement

The rate of the suspension deflection is governed by

$$\dot{x}_{sr} = -\left(v_{zsr} - v_{zur}\right) \tag{6.3}$$

The initial value of the suspension spring deflection x_{sir} depends on the vertical load on the suspension when the vehicle is in the rest position on the level ground. x_{sir} can be found by the static analysis as

$$x_{sir} = \frac{m_s g}{2k_{sr}} \tag{6.4}$$

The governing dynamic equation for the suspension spring deflection on the left-hand side can be found in a similar way as

$$\dot{x}_{sl} = -\left(v_{zsl} - v_{zul}\right) \tag{6.5}$$

The vertical velocity at the right corner strut, v_{zsr}, is equal to

$$v_{zsr} = \frac{-c}{2}\omega_x + v_z \tag{6.6}$$

The normal force F_{Zr} at the tire contact patch is balanced by the tire spring force F_{Ztr}, therefore

$$F_{Zr} = k_{tr} x_{tr} \tag{6.7}$$

The tire deflection x_{tr} shown in Figure 6.4 is measured from the line passing through the nominal wheel hub with height of r_0, and it is positive when the tire is under compression.

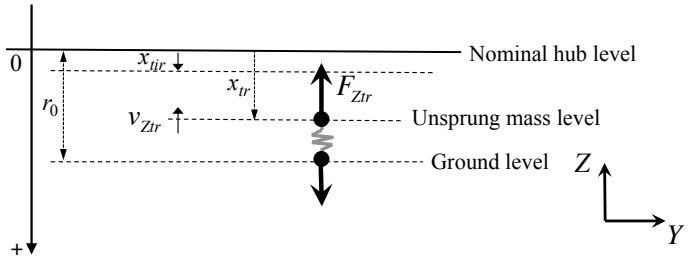

Figure 6.4: Tire deflection measurement

Considering ground to be smooth and level, the tire deflection rate $\dot{x}_{tr}$ is of the same amplitude as the unsprung vertical velocity v_{Zur} in the inertial frame

$$\dot{x}_{tr} = -v_{Zur} \tag{6.8}$$

where v_{Zur} is the transformation of the v_{zur} and v_{yur} from the coordinate frame 1 to the inertial frame.

$$v_{Zur} = v_{zur} \cos(\phi) - v_{yur} \sin(\phi) \tag{6.9}$$

The initial deflection of the tire x_{tir} can be written as

$$x_{tir} = \frac{(m_s + m_{ur} + m_{ul})\, g}{2k_{tr}} \tag{6.10}$$

In Eq. 6.1, v_{yur} is the lateral velocity of the unsprung mass at the right corner, and it is equivalent to

$$v_{yur} = l_{sr}\omega_x \tag{6.11}$$

and l_{sr} can be obtained by

$$l_{sr} = l_{sir} - (x_{sr} - x_{sir}) \tag{6.12}$$

The initial length of the suspension on the right corner of the vehicle, l_{sir}, can be determined by Eq. 6.13.

$$l_{sir} = h - (r_0 - x_{tir}) \tag{6.13}$$

Finally, the lateral force F_{Yr} can be approximated by Eq. 6.14 [13].

$$F_{Yr} = -a_y F_{Zr} \tag{6.14}$$

Analogous with the dynamics of the unsprung mass on the right side, the dynamics of the unsprung mass on the left side of the vehicle can be derived as

$$\dot{v}_{zul} = \frac{1}{m_{ul}} \left(F_{zul} - W_{ul} a_y \sin(\phi) - W_{ul} \cos(\phi) + F_{Zl} \cos(\phi) + F_{Yl} \sin(\phi)\right) - \omega_x v_{yul} \tag{6.15}$$

Figure 6.5 represents the free body diagram of the sprung mass. The lateral forces, F_{usr} and F_{usl}, are applied to the sprung mass at the roll centres RC_r and RC_l [7]. These forces can be found by

$$F_{usr} = F_{Yr}\cos(\phi) + F_{Zr}\sin(\phi) \tag{6.16}$$

and

$$F_{usl} = F_{Yl}\cos(\phi) + F_{Zl}\sin(\phi) \tag{6.17}$$

The forces, F_{zsr} and F_{zsl}, are acting on the right and the left side of the sprung mass, respectively. The centrifugal force $W_s a_y$ is applied to the CG of the sprung mass as the result of the lateral dynamics of the vehicle.

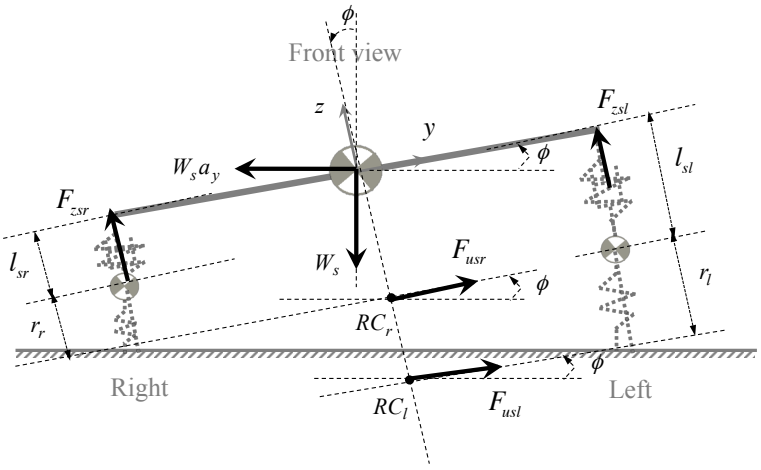

Figure 6.5: Free body diagram of the sprung mass

The dynamic equations governing the vertical motion and the roll motion of the sprung mass can be obtained as follows:

$$\dot{v}_z = \frac{1}{m_s}\left(F_{zsr} + F_{zsl} - W_s a_y \sin(\phi) - W_s \cos(\phi)\right) \tag{6.18}$$

$$\begin{aligned}\dot{\omega}_x = {} & \tfrac{1}{J_x}\Big(F_u sr\,(l_{sr} + r_r) + F_{usl}\,(l_{sl} + r_l)\Big) + \tfrac{1}{J_x}\,(F_{zsl} - F_{zsr})\,\tfrac{c}{2} \\ & + \tfrac{1}{J_x}\Big(\Big(W_{ur} a_y \cos(\phi) - W_{ur}\sin(\phi)\Big) l_{sr} + \Big(W_{ul} a_y \cos(\phi) - W_{ul}\sin(\phi)\Big) l_{sl}\Big)\end{aligned} \tag{6.19}$$

The last term in Eq. 6.19 is due to the effect of the unsprung weights and inertia forces on the roll motion. The instantaneous tire radius on the right-hand side, r_r, is

attained by

$$r_r = r_0 - \frac{x_{tr}}{\cos(\phi)} \tag{6.20}$$

Considering the geometry of the vehicle in Figure 6.5, the instantaneous tire deflection on the left-hand side, r_l, can be calculated by

$$r_l = (l_{sr} + r_r) + c\ \tan(\phi) - l_{sl} \tag{6.21}$$

where x_{tl} can be found by

$$x_{tl} = (r_0 - r_l)\cos(\phi) \tag{6.22}$$

Finally, the roll angle ϕ in preceding equations can be found by

$$\dot{\phi} = \omega_x \tag{6.23}$$

The whole nonlinear 4-DOF vehicle roll model differential equations can be given by

embedding aforementioned equations as

$$\begin{cases} \dot{\phi} = \omega_x \\ \dot{\omega}_x = \frac{1}{J_x}\Big(F_u sr\,(l_{sr}+r_r) + F_{usl}\,(l_{sl}+r_l)\Big) + \frac{1}{J_x}\,(F_{zsl}-F_{zsr})\,\frac{c}{2} \\ +\frac{1}{J_x}\Big(\big(W_{ur}a_y\cos(\phi) - W_{ur}\sin(\phi)\big)l_{sr} + \big(W_{ul}a_y\cos(\phi) - W_{ul}\sin(\phi)\big)l_{sl}\Big) \\ \dot{v}_z = \frac{1}{m_s}\,(F_{zsr}+F_{zsl} - W_s a_y\sin(\phi) - W_s\cos(\phi)) \\ \dot{v}_{zur} = \frac{1}{m_{ur}}\,(F_{zur} - W_{ur}a_y\sin(\phi) - W_{ur}\cos(\phi) + F_{Zr}\cos(\phi) - F_{Yr}\sin(\phi)) \\ -\omega_x v_{yur} \\ \dot{v}_{zul} = \frac{1}{m_{ul}}\,(F_{zul} - W_{ul}a_y\sin(\phi) - W_{ul}\cos(\phi) + F_{Zl}\cos(\phi) - F_{Yl}\sin(\phi)) \\ -\omega_x v_{yul} \\ \dot{x}_{sr} = -v_{zsr} + v_{zur} \\ \dot{x}_{sl} = -v_{zsl} + v_{zul} \\ \dot{x}_{tr} = -v_{zur}\cos(\phi) + v_{yur}\sin(\phi) \end{cases} \tag{6.24}$$

From Figure 6.4, it can be realized that the tire deflection changes into negative values when the tire leaves the ground. When lift-off happens for a particular tire, e.g., left-hand side tire, all the forces applied on the ground contact patch of that particular tire are zero, $F_{Yl} = 0$ and $F_{Zl} = 0$, and its instantaneous tire radius turns to the nominal tire radius, $r_l = r_0$.

Therefore, the governing set of differential equations when the left-hand side tire

leaves the ground is

$$\begin{cases} \dot{\phi} = \omega_x \\ \dot{\omega}_x = \frac{1}{J_x}\Big(F_u sr\,(l_{sr} + r_r)\Big) + \frac{1}{J_x}\,(F_{zsl} - F_{zsr})\,\frac{c}{2} \\ +\frac{1}{J_x}\Big(\big(W_{ur}a_y\cos(\phi) - W_{ur}\sin(\phi)\big)l_{sr} + \big(W_{ul}a_y\cos(\phi) - W_{ul}\sin(\phi)\big)l_{sl}\Big) \\ \dot{v}_z = \frac{1}{m_s}\,(F_{zsr} + F_{zsl} - W_s a_y\sin(\phi) - W_s\cos(\phi)) \\ \dot{v}_{zur} = \frac{1}{m_{ur}}\,(F_{zur} - W_{ur}a_y\sin(\phi) - W_{ur}\cos(\phi) + F_{Zr}\cos(\phi) - F_{Yr}\sin(\phi)) \\ -\omega_x v_{yur} \\ \dot{v}_{zul} = \frac{1}{m_{ul}}\,(F_{zul} - W_{ul}a_y\sin(\phi) - W_{ul}\cos(\phi)) - \omega_x v_{yul} \\ \dot{x}_{sr} = -v_{zsr} + v_{zur} \\ \dot{x}_{sl} = -v_{zsl} + v_{zul} \\ \dot{x}_{tr} = -v_{zur}\cos(\phi) + v_{yur}\sin(\phi) \end{cases} \tag{6.25}$$

However, when the tire in the right-hand side leaves the ground, $x_{tr} < 0$, Eqs. 6.21 and 6.22 are no longer valid. In this situation, the tire deflection on the left-hand side can be solved by corresponding differential equation given in Eq. 6.26.

$$\dot{x}_{tl} = -v_{zul}\cos(\phi) + v_{yul}\sin(\phi) \tag{6.26}$$

In consequence when the right-hand side tire leaves the ground, the set of deferential

equations which governs the behaviour of the nonlinear 4-DOF vehicle roll model is

$$\begin{cases} \dot{\phi} = \omega_x \\ \dot{\omega}_x = \frac{1}{J_x}\Big(F_u sr\,(l_{sr}+r_r) + F_{usl}\,(l_{sl}+r_l)\Big) + \frac{1}{J_x}\,(F_{zsl}-F_{zsr})\,\frac{c}{2} \\ +\frac{1}{J_x}\Big(\Big(W_{ur}a_y\cos(\phi) - W_{ur}\sin(\phi)\Big)l_{sr} + \Big(W_{ul}a_y\cos(\phi) - W_{ul}\sin(\phi)\Big)l_{sl}\Big) \\ \dot{v}_z = \frac{1}{m_s}\,(F_{zsr}+F_{zsl} - W_s a_y\sin(\phi) - W_s\cos(\phi)) \\ \dot{v}_{zur} = \frac{1}{m_{ur}}\,(F_{zur} - W_{ur}a_y\sin(\phi) - W_{ur}\cos(\phi)) - \omega_x v_{yur} \\ \dot{v}_{zul} = \frac{1}{m_{ul}}\,(F_{zul} - W_{ul}a_y\sin(\phi) - W_{ul}\cos(\phi) + F_{Zl}\cos(\phi) - F_{Yl}\sin(\phi)) \\ -\omega_x v_{yul} \\ \dot{x}_{sr} = -v_{zsr} + v_{zur} \\ \dot{x}_{sl} = -v_{zsl} + v_{zul} \\ \dot{x}_{tl} = -v_{zul}\cos(\phi) + v_{yul}\sin(\phi) \end{cases} \tag{6.27}$$

In this chapter, it is assumed that in all maneuvers, a tire on one side of the vehicle is in contact with ground. In the case that both left and right-hand side tires leave the ground, an extra state needs to be defined, which is beyond the scope of this thesis.

6.3 Validation of the Nonlinear 4-DOF Vehicle Roll Model

To justify the accuracy of the roll variables, roll angle ϕ and roll rate ω_x, predicted by the nonlinear 4-DOF vehicle roll model, a comparison between these variables and those predicted by the nonlinear 14-DOF full vehicle model is necessary. As a case study, a midsize sport utility vehicle (SUV) with parameter values given in Table 6.1

is considered [5]. The Magic Formula [10] tire model is employed to estimate the tire forces for the nonlinear 14-DOF full vehicle model.

The comparing procedure is to simulate the nonlinear 14-DOF full vehicle model for a typical maneuver, use the resulting lateral acceleration to feed the nonlinear 4-DOF vehicle roll model, and compare the roll variables predicted by both models. To stimulate the roll variables, four maneuvers are examined: (a) step steer input, (b) ramp steer input, (c) single-lane change steering input, and (d) NHTSA J-turn event input. In the first three maneuvers, the steer profiles are exported from ADAMS/Car software [68], and in the last one, the steer profiles are designed in MATLAB/SIMULINK based on the procedure described by NHTSA [3]. For solving the ordinary differential equations governing the behaviour of the nonlinear 4-DOF vehicle roll model and the nonlinear 14-DOF full vehicle model, the Runge-Kutta method in MATLAB software is employed.

6.3.1 Step Steer Input

A step change in the steer angle is the simplest test to prompt the roll motion of the vehicle. This maneuver is executed when the vehicle is driven in a straight-line motion at a constant speed by suddenly turning the steer wheel to the desired angle. The speed is kept constant during the maneuver. Figure 6.6(a) demonstrates the steer angle of the wheel for the step input. In this maneuver the wheels are steered up to 2.6 $^\circ$ in 0.5 s while the vehicle is at a constant longitudinal speed of 50 km/h. The lateral acceleration predicted by the nonlinear 14-DOF full vehicle model is shown in Figure 6.6(b). It shows that the vehicle experienced a steady-state lateral acceleration

Table 6.1: Vehicle parameters

Parameter	Notation	Value	Unit
Sprung mass	m_s	1440	kg
Sprung mass roll inertia	J_x	900	$kg\ m^2$
Sprung mass pitch inertia	J_y	2000	$kg\ m^2$
Sprung mass yaw inertia	J_z	2000	$kg\ m^2$
Distance of the front axle from sprung mass CG	a	1.016	m
Distance of the front axle from sprung mass CG	b	1.524	m
Sprung mass CG height	h	0.75	m
Front/rear track width	c_{fr}, c_{re}	1.5, 1.5	m
Front suspension stiffness	k_{sfr}	35000	N/m
Front suspension damping coefficient	b_{sfr}	2500	Ns/m
Rear suspension stiffness	k_{sre}	30000	N/m
Rear suspension damping coefficient	b_{sre}	2000	Ns/m
Front/rear unsprung mass	$m_{ufr} = m_{ure}$	80	kg
Front/rear tire stiffness	$k_{tfr} = k_{tre}$	200000	N/m
Nominal tire radius	r_0	0.285	m
Steering ratio	n_s	20 : 1	$-$

of 0.35 g. The roll angles and roll rates predicted by the nonlinear 4-DOF vehicle roll model and the 14-DOF full vehicle model are plotted in Figures 6.6(c) and 6.6(d). By comparing these plots, it can be seen that the nonlinear 4-DOF vehicle roll model predicts the roll angle and the roll rate of the nonlinear 14-DOF full vehicle model accurately.

6.3.2 Ramp Steer Input

Ramp steer is another maneuver to excite the roll behaviour. To execute this maneuver, first the vehicle is driven in a desire constant longitudinal speed. Then, while the speed is kept constant, the steer angle is increased with a constant desirable slope. In Figure 6.7(a), for the nonlinear 14-DOF full vehicle model in the constant speed of 50 km/h, the steer angle starts to increase at time 6 s with the slope of 1 $^\circ/s$.

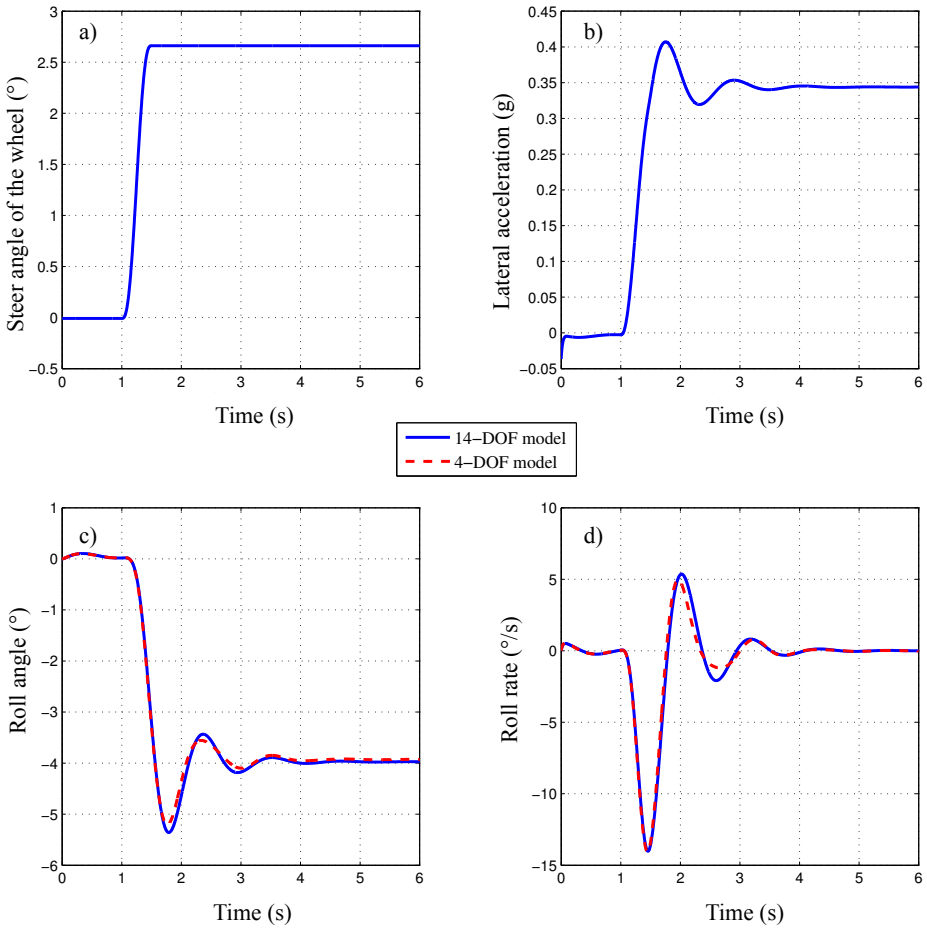

Figure 6.6: Comparison of the vehicle roll variables between models during the step steering at the speed of 50 km/h

The corresponding lateral acceleration predicted by the nonlinear 14-DOF full vehicle model is shown in Figure 6.7(b). Figures 6.7(c) and 6.7(d) illustrate the roll angles and roll rates for both models. As it can be seen, the roll angle and roll rate predicted by the nonlinear 4-DOF vehicle roll model follow the roll angle and roll rate predicted by the nonlinear 14-DOF full vehicle model.

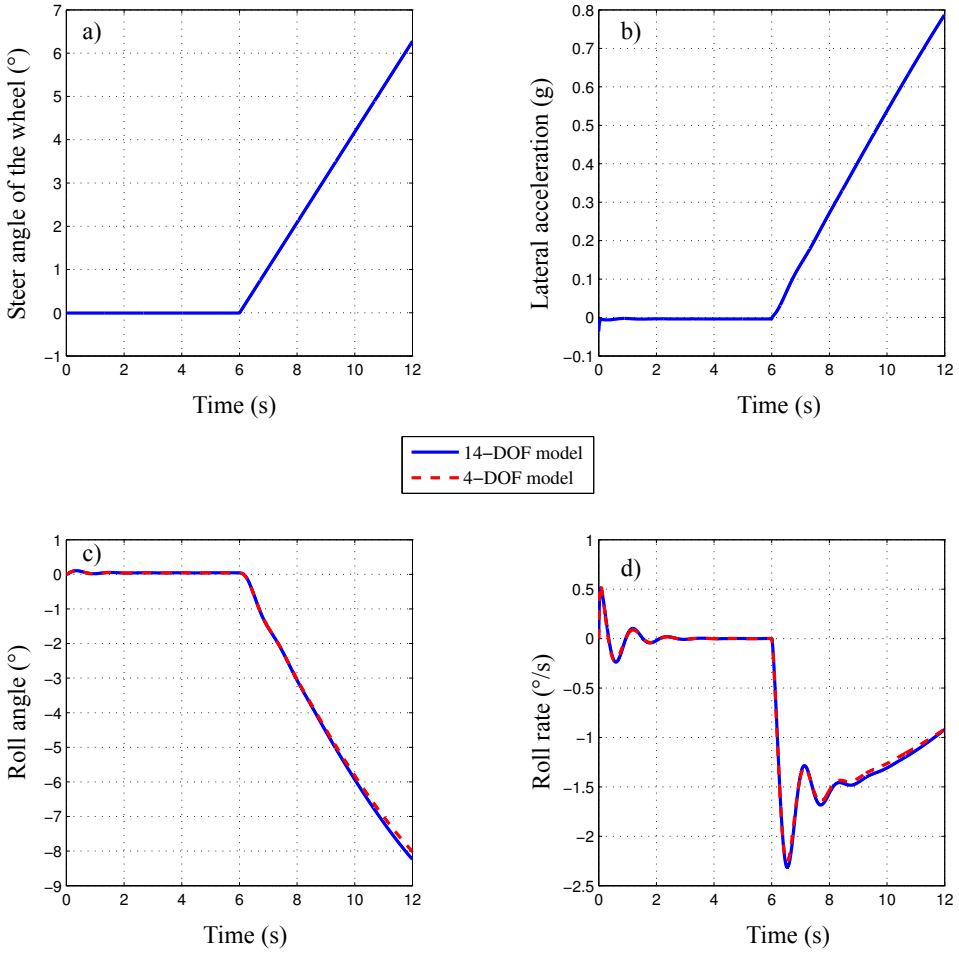

Figure 6.7: Comparison of the vehicle roll variables between models during the ramp steering at the speed of 50 km/h

6.3.3 Single-lane Change Steer Input

In a single-lane change maneuver, the vehicle exits from one lane and enters the nearby lane. The steer profile for the single-lane change is given in Figure 6.8(a). In this figure, the nonlinear 14-DOF full vehicle model is driven at a constant speed

of 50 km/h while the single-lane change maneuver occurs. As a result the lateral acceleration, shown in Figure 6.8(b), has a sinusoidal shape with positive peak of 0.62 g and the negative peak of 0.78 g. From the plot of roll angles, given in Figure 6.8(c), it can be seen that the predicted roll angle by the nonlinear 4-DOF vehicle roll model is almost the same as the predicted roll angle by the nonlinear 14-DOF full vehicle model. Comparing the roll rates in Figure 6.8(d), it can be recognized that the roll rate estimated by the nonlinear 4-DOF vehicle model has a negative peak value of $-58\ ^\circ/s$ while the negative peak of the roll rate estimated by the nonlinear 14-DOF is $-38\ ^\circ/s$. To understand why this difference originates, the normal forces at the left and right-hand side, F_{Zl} and F_{Zr}, are plotted in Figures 6.9(a) and 6.9(b). It should be noted that in the case of the nonlinear 14-DOF full vehicle model, the summation of the same side forces at front and rear axles is considered. From the plot for the left-hand side forces, Figure 6.9(a), it can be seen that the left-hand side force predicted by the nonlinear 4-DOF vehicle roll model, dashed red graph, reaches zero sooner than the force predicted by the nonlinear 14-DOF full vehicle model, and it endured longer. As discussed before, the zero normal force is the result of tire lift-off occurrence. Therefore, the tire lift-off occurrence for the nonlinear 4-DOF vehicle roll model in this maneuver is more serious than that happened for the nonlinear 14-DOF full vehicle model. In predicting the roll motion for this maneuver, the nonlinear 4-DOF vehicle roll model was more conservative, e.i., safer, than the nonlinear 14-DOF full vehicle model.

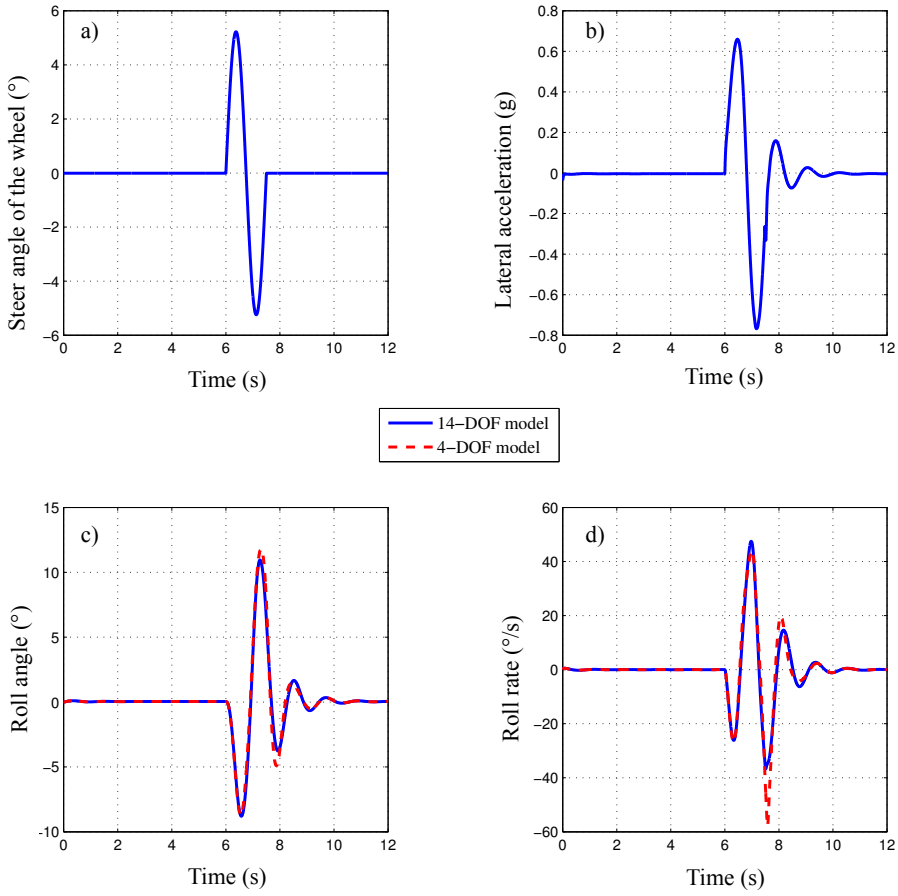

Figure 6.8: Comparison of the vehicle roll variables between models during the single-lane change profile at the speed of 50 km/h

6.3.4 NHTSA J-turn Steer Input

NHTSA J-turn is one of the most famous NHTSA rollover resistance maneuver [3]. The maneuver begins when the vehicle is in a straight-line motion at a speed slightly higher than the desired entrance speed. The throttle is released and when the vehicle reaches the desired entrance speed, the steer wheel ramps to a maximum of 8 times

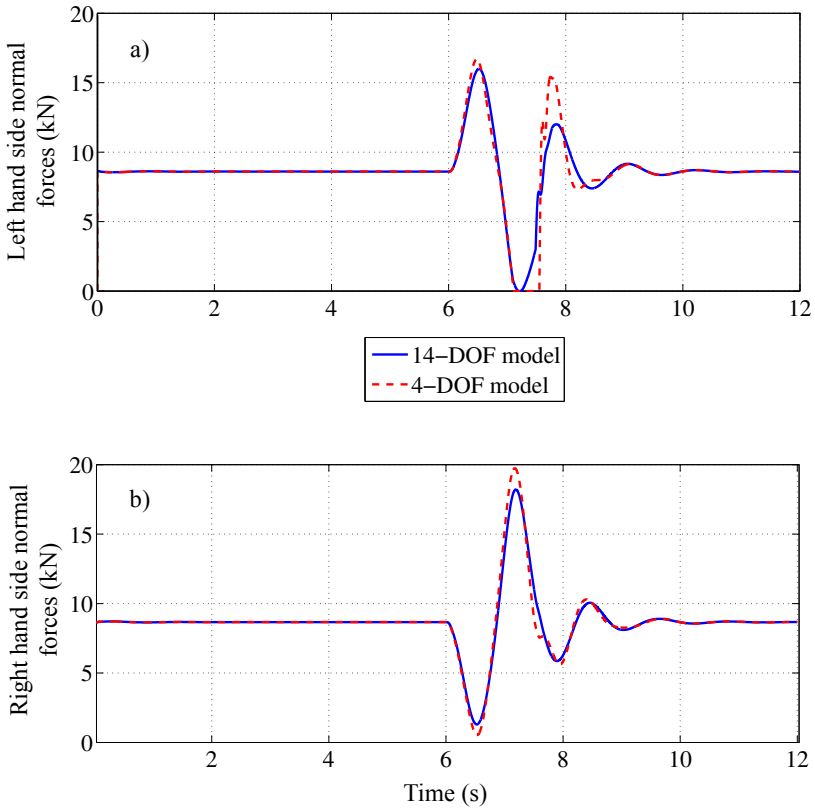

Figure 6.9: Comparison of the normal forces between models during the single-lane change profile at the speed of 50 km/h

of the steer wheel angle $\delta_{0.3g}$, where the vehicle experiences 0.3 g lateral acceleration, with the slope of 1000 $^\circ/s$. The vehicle is driven for 4 s and then the steer wheel returns to zero position during a 2 s time interval with constant slope. In following, the J-turn maneuver for three different speeds is discussed.

J-turn Maneuvre at Speed of 20 km/h

The steer profile for the J-turn maneuver at the speed of 20 km/h is shown in Figure 6.10(a). From the lateral acceleration plot in Figure 6.10(b), it can be seen that the

nonlinear 14-DOF full vehicle model predicted the peak value of 0.6 g for this maneuver. The roll variables estimated by both models in this maneuver are plotted in Figures 6.10(c) and 6.10(d). From these figures, it can be observed that the nonlinear 4-DOF vehicle roll model correlates very well with the nonlinear 14-DOF full vehicle model. The predicted left-hand and right-hand side forces by these models are given in Figures 6.11(a) and 6.11(b), respectively. Comparison between normal forces predicted by both models reveals that both models predicted that all tires were on the ground during this J-turn maneuver.

J-turn Maneuver at Speed of 25 km/h

As another trial, the J-turn maneuver with the previous steer profile, shown in Figure 6.12(a), has been examined at a speed of 25 km/h. The correspond lateral acceleration predicted by the nonlinear 14-DOF full vehicle model are shown in Figure 6.12(b). At this speed, the peak value of the lateral acceleration is over 0.7 g. From the roll variable plots for models given in Figures 6.12(c) and 6.12(d) it can be seen that at this speed, the nonlinear 4-DOF vehicle roll model produced larger peaks in the roll angle and the roll rate. The reason can be revealed by comparing the corresponding normal forces. The normal forces for both models are given in Figure 6.13(a) for the left-hand side and in Figure 6.13(b) for the right-hand side. From Figure 6.13(b), it can be seen that the tire lift-off happened on the right-hand side of the nonlinear 4-DOF vehicle roll model. However, the nonlinear 14-DOF full vehicle model did not predict that tire left-off occurred. Therefore, in this maneuver the nonlinear 4-DOF roll model was safer and predicted the worse behaviour. It should be noted that in

this maneuver, the state transfer from Eq. 6.24 to equation Eq. 6.27 occurs since the right-hand side tires left the ground.

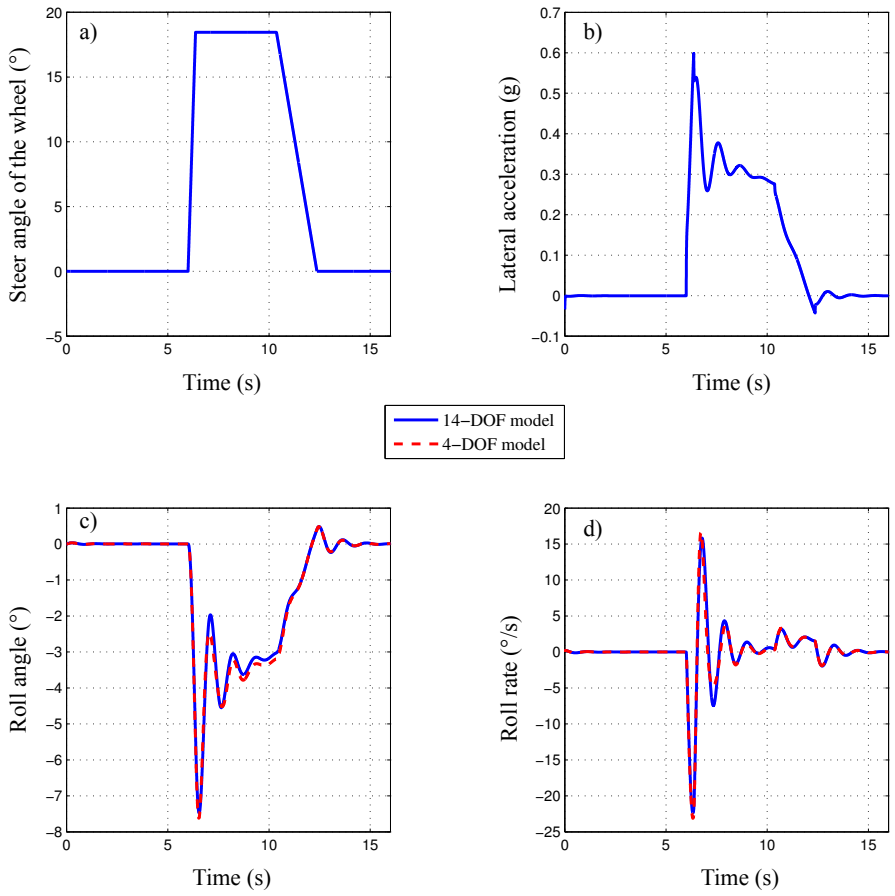

Figure 6.10: Comparison of the vehicle roll variables between models during the J-turn maneuver at the speed of 20 km/h

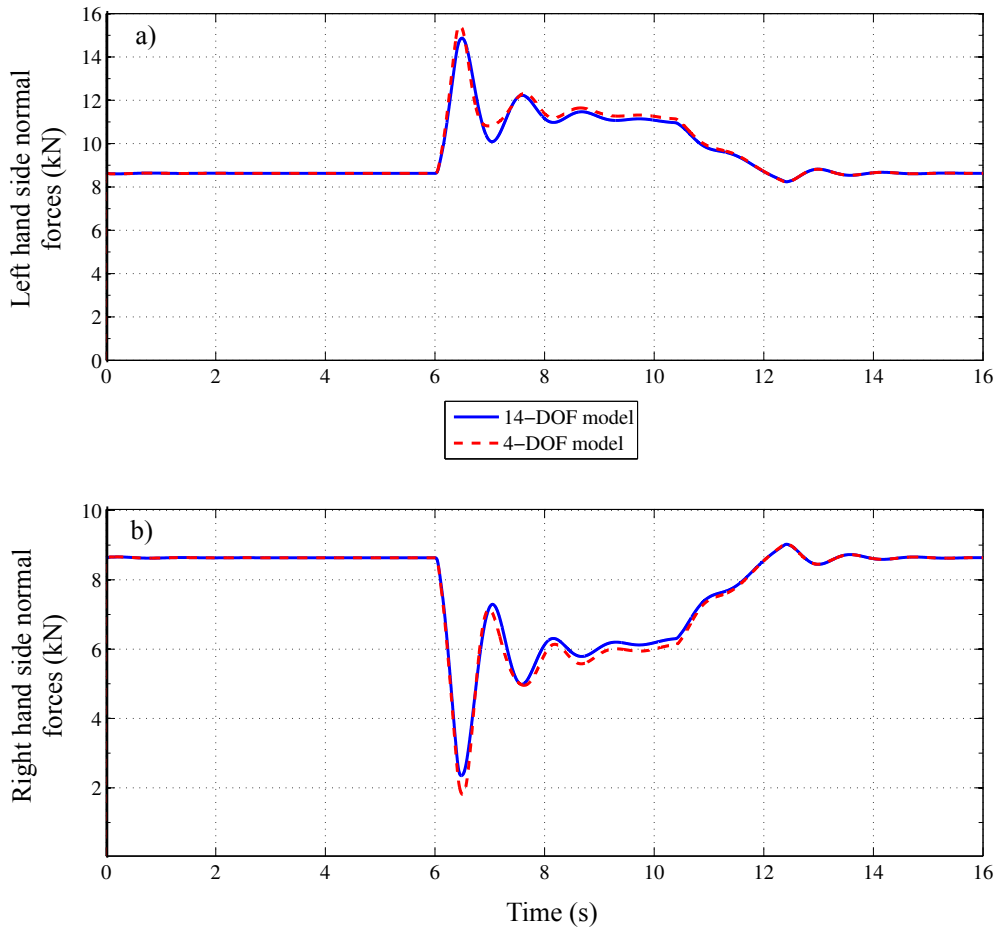

Figure 6.11: Comparison of the normal forces between models during the J-turn maneuver at the speed of 20 km/h

Prediction of the Rollover Accident in the J-turn Maneuver

In the J-turn maneuver at the speed of 25 km/h, the right-hand side tire left the ground for a moment. However, the rollover did not happen. In this part, the rollover speed – the minimum speed at which the rollover accident occurs – will be predicted. The procedure for finding the rollover speed is to increase the speed and

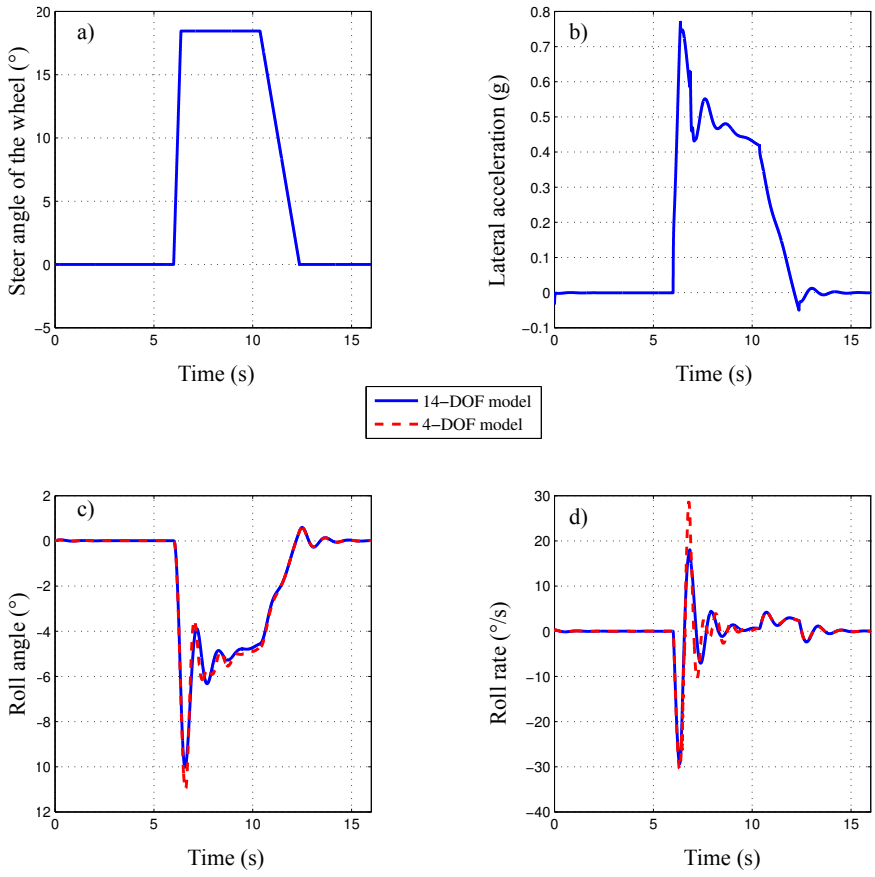

Figure 6.12: Comparison of the vehicle roll variables between models during the J-turn maneuver at the speed of 25 km/h

compare the predicted roll angles by the models. In Figure 6.14, the steer profile, lateral acceleration, roll angle, and roll rate plots when the speed is 29 km/h are given. Comparison between the plots for roll angles and the roll rates, Figures 6.14(c) and 6.14(d), reveal that at this speed, the roll variables predicted by the nonlinear 4-DOF vehicle roll model oscillates with larger magnitude than that corresponding to the nonlinear 14-DOF full vehicle model. The corresponding normal forces are illustrated

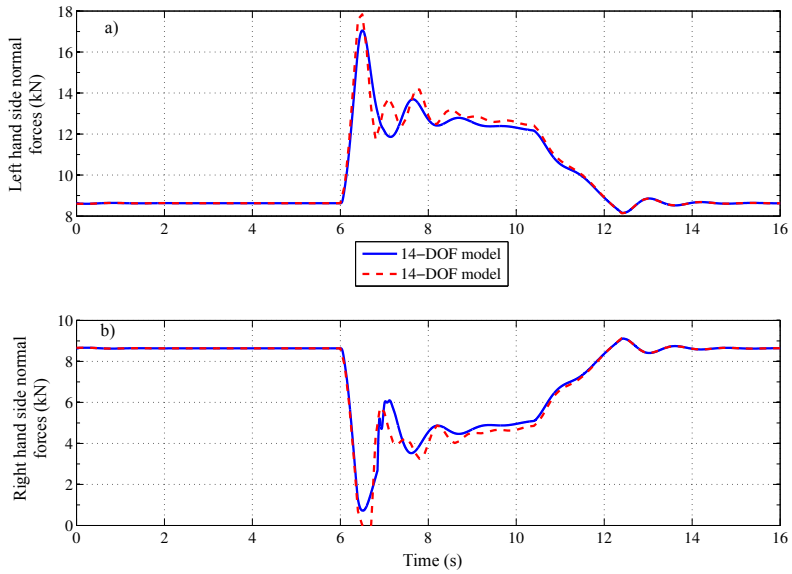

Figure 6.13: Comparison of the normal forces between models during the J-turn maneuver at the speed of 25 km/h

in Figures 6.15(a) and 6.15(b) for the left-hand and right-hand side, respectively. From the force plot for the right-hand side wheels in Figure 6.15(b), it can be seen that the tire lift-off occurred for both models. However, the nonlinear 14-DOF full vehicle model predicted the shorter time interval. The nonlinear 4-DOF vehicle roll model predicted oscillations with larger magnitude after the right-hand side tires touched the ground.

In the next step, the speed is increased to the larger values of 30 km/h and 32 km/h. The corresponding lateral accelerations for these speeds are given in Figures 6.16(a) and 6.16(b), and the predicted roll angles are shown in Figures 6.16(c) and 6.16(d). From Figures 6.16(c) and 6.16(d), it can be seen when the speed increases to the values more than 30 km/h, the nonlinear 4-DOF vehicle roll model predicts the

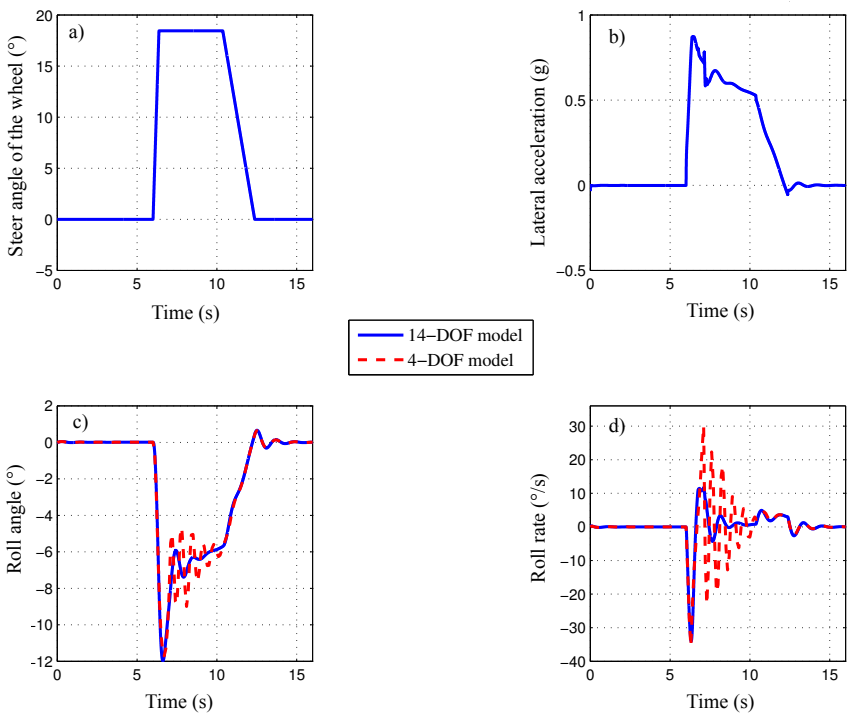

Figure 6.14: Comparison of the vehicle roll variables between models during the J-turn maneuver at the speed of 29 Km/h

rollover accident. However, Figure 6.16(c) shows that the nonlinear 14-DOF full vehicle model did not predict the rollover accident at the speed of 30 km/h. The rollover accident predicted by this model to occur at the speed of 32 km/h. The nonlinear 4-DOF vehicle roll model is more conservative, i.e., safer, than the nonlinear 14-DOF full vehicle model in prediction of the rollover speed.

Simulation results verify that the nonlinear 4-DOF vehicle roll model can predict the roll behaviour of the nonlinear 14-DOF full vehicle adequately. In the case of high-g maneuvers, where the tire lift-off prompts to occur, the nonlinear 4-DOF vehicle roll

model is safer and predicts the occurrence of the tire lift-off prior to the nonlinear 14-DOF full vehicle model. Moreover, in the J-turn maneuver, the nonlinear 4-DOF vehicle roll model predicts the smaller critical speed in which the rollover occurs.

The reason behind the difference in the roll behaviour predicted by the models is that the nonlinear 14-DOF full vehicle model slips laterally in high-g maneuvers, which reduces the roll motion of the vehicle. However, in the nonlinear 4-DOF vehicle roll model, all portions of the lateral forces produce torque to roll the vehicle since the side slip is not considered. It is worth mentioning that conservative prediction can make the nonlinear 4-DOF vehicle roll model a safer model since driving far from the rollover speed is always desirable.

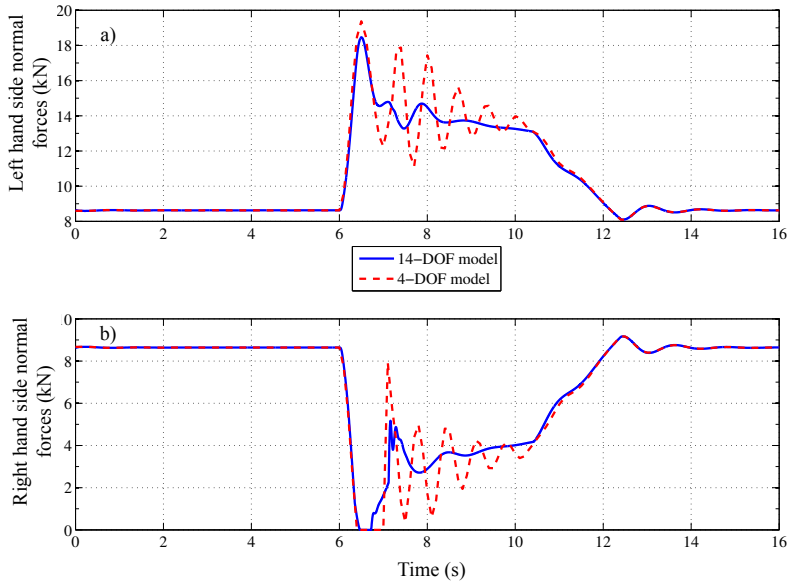

Figure 6.15: Comparison of the normal forces between models during the J-turn maneuver at the speed of 29 Km/h

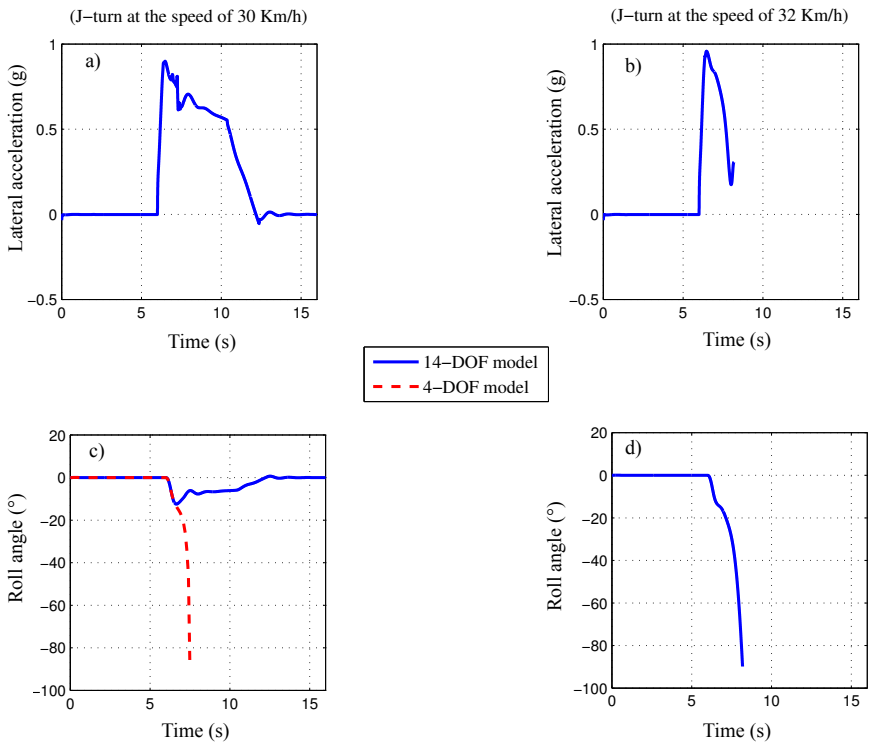

Figure 6.16: Prediction of the minimum speed for rollover accident in the J-turn maneuver

6.4 $1/5^{th}$ Scale Experimental Test Vehicle

The SETV was developed for the physical validation of the 4-DOF roll vehicle model[2]. A $1/5^{th}$ scale Baja electric vehicle supplied by HPI racing company (Kit version[3]) was considered as the platform. Then, it was modified to the SETV as shown in Figure 6.17 by a group of students at the University of Manitoba. The SETV was

[2]This section is published in [69].

[3]In Kit versions, the manufacture sells the set of parts separately, and then the buyer assembles them into a scale vehicle.

equipped with encoders and IMU[4] to measure real time motion parameters that were used in collecting motion-related data and closed loop control. A roll cage structure armed with outrigger wheels was mounted on the vehicle to protect the electronics and prevent the rollover accident. Some simple structures were also added to mount sensors in their places.

6.4.1 Roll Safety Structure

The roll safety structure was built by steel hardware supplied as a kit by VexRobotic company. The reasons for selecting the hardware kit were: reducing the cost of manufacturing, saving time, and providing versatile design. After some trial and error, the final steel structure (see Figure 6.17) was built. The electronics were installed on the middle of the structure for maximum safety. The roll safety structure has a versatile design to change the position of the battery pack in the case of necessary changes in the CG of the vehicle. Finally, two wheels were mounted on the sides of the structure to prevent the roof of the vehicle touching the ground.

The simplified Finite Element Model (FEM) of the roll safety structure was developed in Abaqus FEA software [70]. The stress distribution for the worst scenario when an outrigger wheel touch the ground was analyezd. The final assembled body structure and the stress distribution have been demonstrated in Figure 6.18. Then, the results of the FEM analysis were used to optimize the design of the structure. More details on finite element analysis of the roll safety structure can be found in [70].

[4]IMU stands for Inertial Measurement Unit.

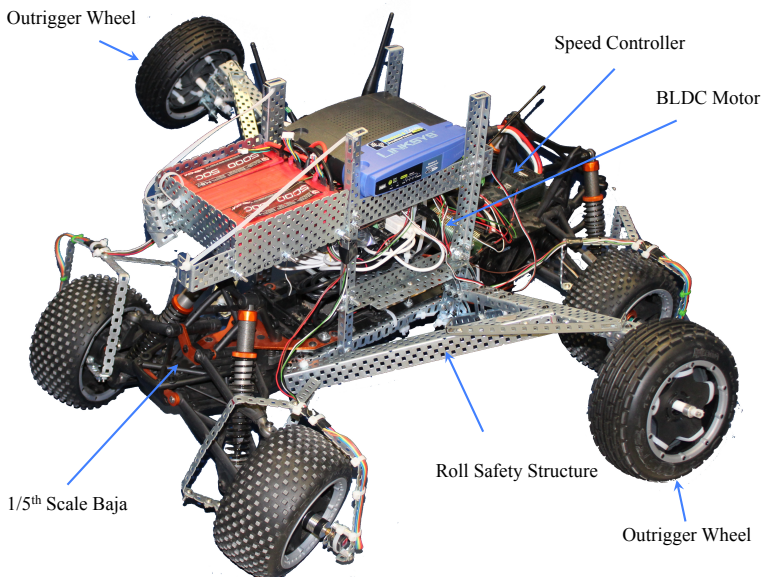

Figure 6.17: Completed prototype

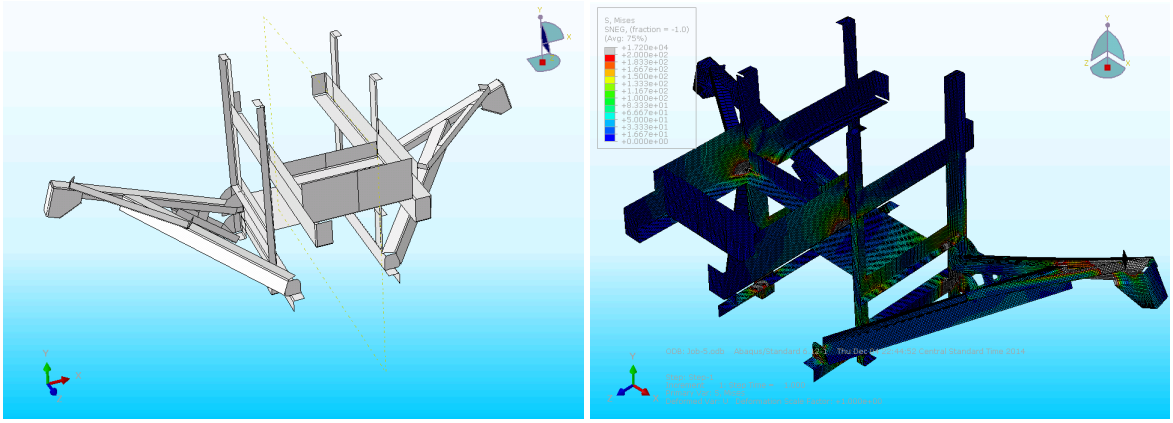

Figure 6.18: Simplified structure and its stress distribution in Abaqus FEA software.

6.4.2 Powertrain

The powertrain of the scale Baja includes a brushless direct current (BLDC) motor powered by eight cell Lithium Polymer (LiPo) batteries in a series configuration. The

motor has a 800 k_v rating[5], maximum power of 7 kw , and it can be driven up to 45,000 rpm. An Electric Speed Controller (ESC) module drives the motor and monitors its state. Both the motor and ESC are manufactured by the Castle company. The motor shaft is connected to the transmission by a spur gear with a fixed $8:1$ gear ratio. A $1:1$ differential gear box is installed at the rear of the vehicle to transfer the torque through dogbones to the rear wheels.

6.4.3 Vehicle Parameter Identification

In order to use the SETV for physical validation of the mathematical model, a variety of vehicle parameters should be derived. Table 6.2 lists the measured vehicle parameters. These parameters are measured through various experiments which are described in details in [71].

6.4.4 Electrical Design

The electrical design of the scale vehicle is composed of two parts. The first is the hardware for electric drive, sensors, and embedded computer, and the second one is the software that allows the modules to be monitored and controlled through a local network.

[5] k_v is the motor velocity constant and 800 k_v means if 1 v voltage is applied to the motor, it spins 800 rpm.

Table 6.2: SETV parameters

Parameter	Notation	Value	Unit
Sprung mass	m_s	12.132	kg
Sprung mass roll inertia	J_x	0.23	$kg\ m^2$
Sprung mass pitch inertia	J_y	0.58	$kg\ m^2$
Sprung mass yaw inertia	J_z	0.49	$kg\ m^2$
Sprung mass CG height	h	0.17	m
Distance of the front axle from sprung mass CG	a	0.326	m
Distance of the front axle from sprung mass CG	b	0.257	m
Front/rear track width	c_f, c_r	$0.38, 0.38$	m
Front suspension stiffness	k_{sf}	703	N/m
Front suspension damping coefficient	b_{sf}	26.5	Ns/m
Rear suspension stiffness	k_{sr}	750	N/m
Rear suspension damping coefficient	b_{sr}	26.5	Ns/m
Front/rear unsprung mass	m_{uf}, m_{ur}	$1.38, 1.59$	kg
Front/rear tire stiffness	$k_{tf} = k_{tr}$	25375	N/m
Nominal tire radius	r_0	0.0842	m

Hardware

The SETV has been set up on the basis of systems shown in Figure 6.19. It is possible to either control the vehicle manually using the transmitter (supplied by the factory) or automatically by the User Interface (UI). In the latter case, the user interacts with the system by means of web browser, uploads a desired steer profile as a text file, and sets the desired speed. Then, the given driving profile is executed automatically. In automatic driving, the SETV uses an open loop controller for steering the vehicle and a closed loop Proportional-Integral-Derivative (PID) controller for driving the vehicle at the desired speed [71]. The selection between manual drive or automatic drive is controlled by means of toggle switch already mounted on the transmitter. This toggle switch also can be used as a safety feature when the vehicle is out of control.

A USB[6] camera is mounted on the vehicle to capture video frames for realtime video streaming on the web user interface.

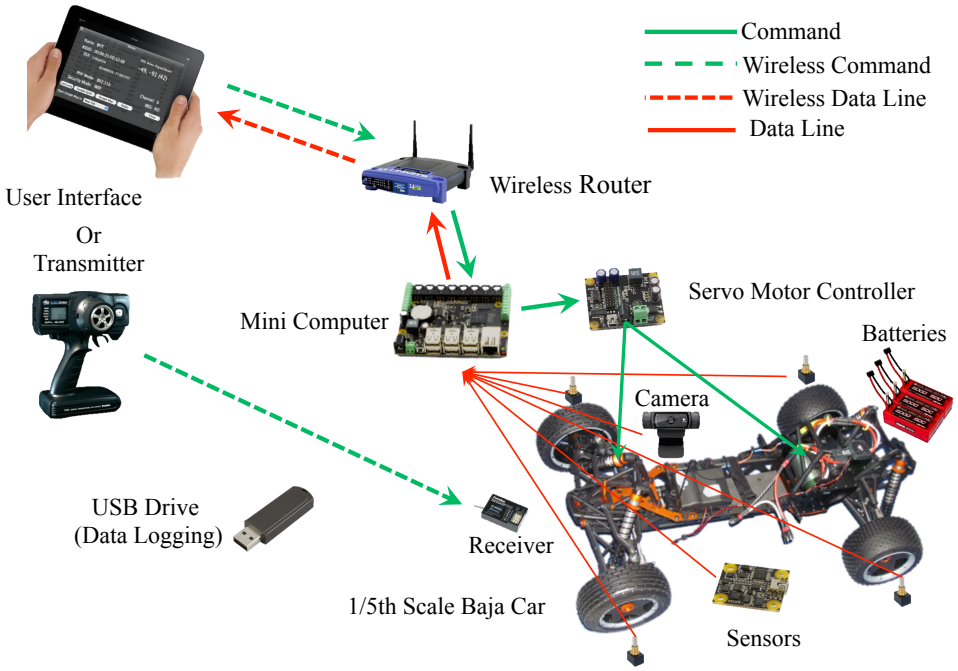

Figure 6.19: Schematic of the SETV set up

The linear accelerations and angular velocities of the sprung mass are measured by an IMU, mounted on the CG of the sprung mass. Magnetic incremental encoders assembled at the hub axes of all four wheels measure the wheel angular velocities. A mini computer collects the sensor data, stores the data on a USB memory drive and sends it through wireless router to the user interface. Then, a web browser plots the sensor data in real time graphs. The mini computer and IMU sensor are provided by Phidgets Inc. and the encoders are manufactured by Bourns Inc. A four cell LiPo

[6]USB stands for Universal Serial Bus.

battery powers all the electronics through a voltage regulator circuit.

Software

The software of the SETV, as shown in Figure 6.20, has two parts; a high level frontend that interact with the user, and the low level backend that communicates with the hardware. These parts are briefly described here. However, an interested reader can find more details in [72].

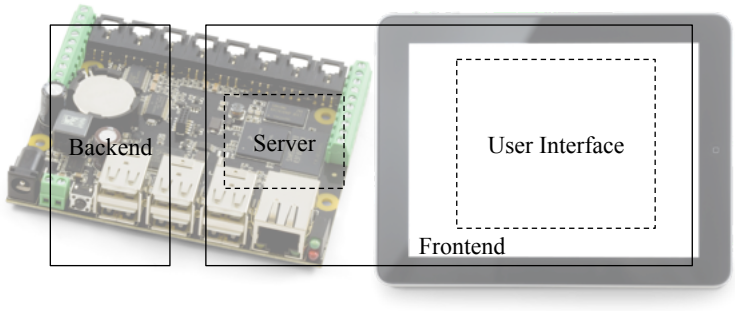

Figure 6.20: Software overview

Frontend Software

The frontend software has a web user interface developed in HTML5[7], Javascript, and CSS[8]. The server is another part of the frontend that connects the UI to the backend. The server that is developed with Java, sends data to the UI and vice versa. The protocol for this communication is known as websockets while the Messagepack protocol is used for packaging data.

[7]HTML stands for Hyper Text Markup Language.
[8]CSS stands for Cascading Style Sheet.

Backend Software

The backend consists of several blocks. The architecture of the backend software is shown in Figure 6.21. Each block is implemented as a Java class. These classes communicate with the hardware, send their data to the server or command the hardware as requested by the server.

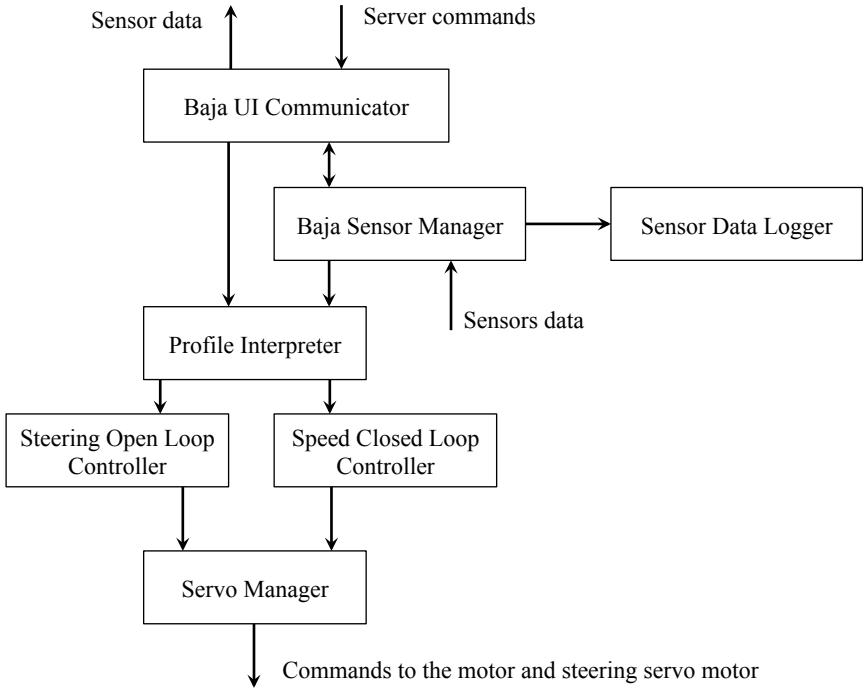

Figure 6.21: Backend software architecture

6.5 Experimental Validation

For the experimental validation of the nonlinear 4-DOF roll vehicle model, the presented SETV was developed. To prompt a rollover accident, the SETV was driven by

a user in a simple closed curve, cornering maneuver, and the corresponding data of the roll rate and lateral acceleration were logged. In Figure 6.22, the collected data for the roll rate and lateral acceleration are plotted in blue colour. These data are sampled at a rate of 20 Hz and filtered by a 8^{th} order zero-phase butterworth digital filter with cut off frequency of 4 Hz. Then, the measured lateral acceleration is fed to the nonlinear 4-DOF roll vehicle model. The roll rate predicted by the simulation is given with red dashed plot in Figure 6.22. From this figure, it can be said that considering the respective dynamics model and measurement accuracy, the roll rate is very well reproduced by the proposed model. Moreover, it can be seen that the model predicts the rollover accident 46 seconds into the maneuver. Figure 6.23 illustrates the SETV at the moment of the rollover. It is worth to mentioning that the outrigger wheel prevented that SETV from rolling more than 45 degrees. This explains the SETV roll rate behaviour after the moment that the rollover accident has been predicted by the simulation.

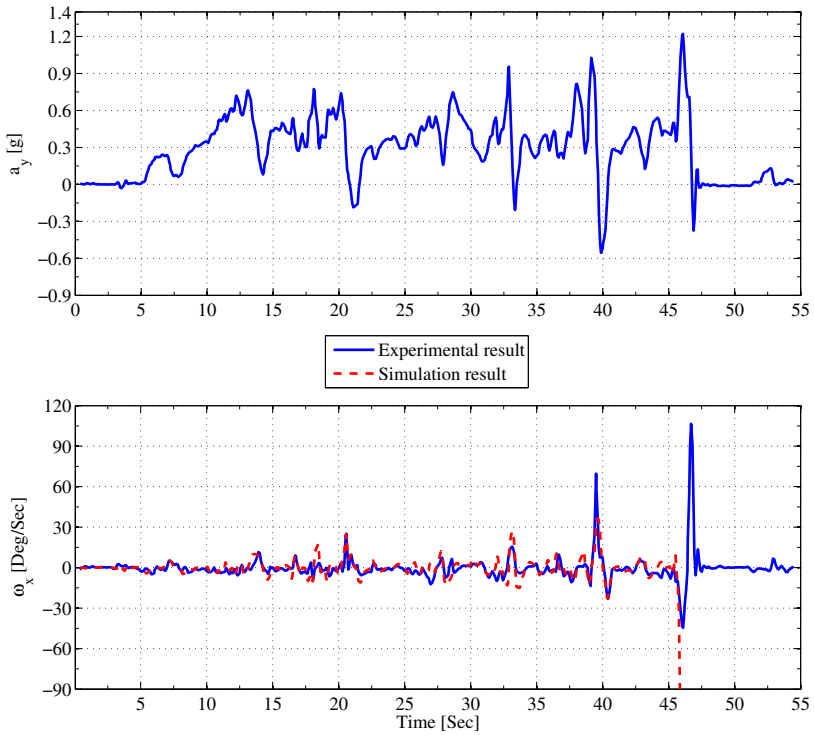

Figure 6.22: Experimental result versus simulation result in the maneuver

Figure 6.23: SETV at the moment of the rollover accident

6.6 Lyapunov Stability Analysis of the Nonlinear 4-DOF Vehicle Roll Model

As mentioned before, Lyapunov stability analysis is a critical subject that must be studied prior to employing the model for further study. In this section, the Lyapunov stability of the nonlinear 4-DOF vehicle roll model when the right-hand side tires are in touch with the ground will be discussed.

The nonlinear 4-DOF vehicle roll model given in Eq. 6.24 is a nonlinear system as a result of both geometric and system dynamic nonlinearities. In the state space, the nonlinear equation for 4-DOF vehicle roll model, Eq. 6.24, can be organized as the non-autonomous system given in Eq. 6.28.

$$\dot{\mathbf{x}} = \mathbf{f}\left(\mathbf{x}, a_y\left(t\right)\right) \tag{6.28}$$

where $\mathbf{x}$ is the 8×1 state vector as

$$\mathbf{x} = \begin{bmatrix} \phi & \omega_x & v_z & v_{zur} & v_{zul} & x_{sr} & x_{sl} & x_{tr} \end{bmatrix}^T \tag{6.29}$$

and $\mathbf{f}$ is the 8×1 nonlinear vector function.

To facilitate the stability analysis, the lateral acceleration a_y is assumed to be constant. Therefore, the non-autonomous system in Eq. 6.28 turns to the autonomous system given in

$$\dot{\mathbf{x}} = \mathbf{f}\left(\mathbf{x}\right) \tag{6.30}$$

The first step to analyze a nonlinear system is to linearize it around the nominal operating point and analyze the resulting linear system by available powerful tools for Lyapunov stability analysis of the linear systems.

6.6.1 Linearization of the Nonlinear 4-DOF Vehicle Roll Model and Local Stability Analysis in the Straight-line Motion

For the nonlinear 4-DOF vehicle roll model, the nominal operating point is the intended stable equilibrium point $\mathbf{x}_e$.

$$\mathbf{x}_e = \begin{bmatrix} \phi_e & \omega_{xe} & v_{ze} & v_{zure} & v_{zule} & x_{sre} & x_{sle} & x_{tre} \end{bmatrix}^T \tag{6.31}$$

Transferring this equilibrium point $\mathbf{x}_e$ to zero, Eq. 6.30 is redefined as

$$\dot{\mathbf{z}} = \mathbf{g}(\mathbf{z}) \tag{6.32}$$

with the intended equilibrium point $\mathbf{z}_e = \begin{bmatrix} 0 & 0 & 0 & 0 & 0 & 0 & 0 & 0 \end{bmatrix}^T$.

Now, the nonlinear state space in Eq. 6.32 can be written around the equilibrium $\mathbf{z}_e$ by Taylor's series as

$$\dot{\mathbf{z}} = \mathbf{J}\mathbf{z} + \mathbf{g}_{h.o.t.}(\mathbf{z}) \tag{6.33}$$

where $\mathbf{g}_{h.o.t.}(\mathbf{z})$ is the nonlinear dynamics near the equilibrium point $\mathbf{z}_e$, and $\mathbf{J}$ is the Jacobian matrix defined at the equilibrium point $\mathbf{z}_e$ by

$$\mathbf{J} = \left(\frac{\partial \mathbf{g}}{\partial \mathbf{z}} \right)_{\mathbf{z}=\mathbf{z_e}} \tag{6.34}$$

The nonlinear 4-DOF vehicle roll model in Eq. 6.32 essentially behaves the same as its linearized approximation, given in Eq. 6.35, around the equilibrium point $\mathbf{z}_e$.

$$\dot{\mathbf{z}} = \mathbf{J}\ \mathbf{z} \tag{6.35}$$

The Lyapunov asymptotical stability of the equilibrium point $\mathbf{x}_e$ for the nonlinear 4-DOF vehicle roll model in Eq. 6.30 is guaranteed if all eigenvalues of Jacobian matrix

in Eq. 6.35 are strictly in the left-half complex plane. This type of stability analysis is based on Lyapunov's linearization method [27], and it is a common practice in engineering.

In the case of straight-line motion on the smooth surface, the lateral acceleration a_y is zero. The equilibrium point for the nonlinear 4-DOF vehicle model is given in Eq. 6.36. It is trivial that in the absence of the lateral motion on the even surface, the equilibrium point has zero values for roll angle, roll rate, vertical sprung and unsprung velocities. Moreover, the steady-state values for the tire and suspensions deflections are equal to their initial values.

$$\mathbf{x}_{e_{a_y=0}} = \begin{bmatrix} 0 & 0 & 0 & 0 & 0 & x_{sir} & x_{tsil} & x_{tir} \end{bmatrix}^T \tag{6.36}$$

Table 6.3 reports the eigenvalues of the linearized model after transferring the equilibrium point $\mathbf{x}_{e_{a_y=0}}$ to the origin. It can be seen that the linearized model in straight-line motion has four conjugate eigenvalues which all are strictly in the left-half complex plane. Therefore, based on the Lyapunov's linearization method, the equilibrium point in the straight-line motion is asymptotically stable for the actual nonlinear 4-DOF vehicle model.

Table 6.3: Eigenvalues of the linearized 4-DOF vehicle roll model in the straight line motion

$\lambda_1 = -2.3442 + 7.7114i$	$\lambda_2 = -2.3442 - 7.7114i$
$\lambda_3 = -2.6076 + 8.9880i$	$\lambda_4 = -2.6076 - 8.9880i$
$\lambda_5 = -16.4058 + 50.2431i$	$\lambda_6 = -16.4058 - 50.2431i$
$\lambda_7 = -16.4897 + 50.0324i$	$\lambda_8 = -16.4897 - 50.0324i$

6.6.2 Movement of the Stable Equilibrium Point in the State Space in Presence of Lateral Acceleration

Another important aspect of stability analysis is to study the movements of the equilibria in the state space as a system parameter varies. For nonlinear autonomous vehicle model in Eq. 6.30, the location of the stable equilibrium point varies by the value of the lateral acceleration a_y. This model is complex, and it is not feasible to find the equilibrium explicitly. Therefore, the intended equilibrium points are computed numerically. In Figure 6.24, the location of the corresponding equilibrium point in the subspace $\phi - x_{tr} - x_{sr}$ has been plotted as the lateral acceleration a_y varies from 0.0 g to 0.85 g. For better illustration, the location of the each equilibrium point in $\phi - x_{tr}$, $\phi - x_{sr}$, and $x_{tr} - x_{sr}$ subspaces is also depicted. From this figure, it can be seen that the equilibrium point moves almost on a line. Therefore, someone may use a linear approximation to roughly predict the steady-state values of roll angle, tire, and suspension's spring deflections for a specific value of the lateral acceleration in the given range.

Moreover, it can be realized from Figure 6.24 that the value of the steady-state roll angle ϕ_e becomes larger as the lateral acceleration increases, and the steady-state right-hand side tire deflection x_{tre} decreases (see $\phi - x_{tr}$ plane). As soon as the steady-state roll angle ϕ_e becomes bigger than 8^o, the right-hand side suspension is no longer under compression (see $\phi - x_{sr}$). However, the right-hand side tire never leaves the ground while the lateral acceleration a_y varies between 0.0 g and 0.85 g (see $x_{tr} - x_{sr}$ plane).

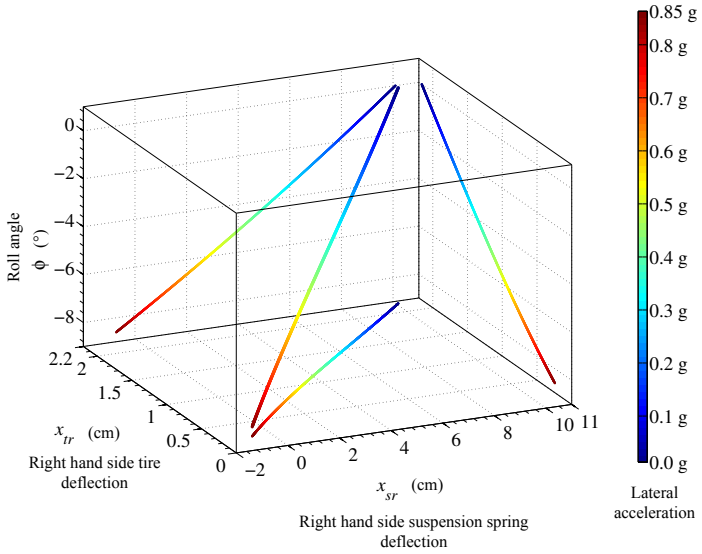

Figure 6.24: Movement of the stable equilibrium point in $x_{sr} - x_{tr} - \phi$ subspace and corresponding projections on $x_{sr} - x_{tr}$, $\phi - x_{sr}$, and $\phi - x_{tr}$ planes when a_y varies from 0.0 g to 0.85 g.

To investigate the Lyapunov stability of the equilibrium points corresponding to these different lateral accelerations, the trajectory of the largest conjugate eigenvalues as the lateral acceleration varies has been illustrated in Figure 6.25. It can be seen that the largest conjugate eigenvalues as long as the value of the lateral acceleration a_y is less than 0.85 g remain in the left-half complex plane. Therefore, the equilibrium point of the nonlinear 4-DOF vehicle model is asymptotically stable for lateral accelerations a_y less than $0.85g$. When the linearized system at least has one eigenvalue on the $j\omega$ axis, the Lyapunov's linearization method fails and the stability of the equilibrium point can not be concluded.

On the other hand, a nonlinear system behaviour is more complex than its equivalent locally linearized system. For example, while the Lyapunov stability of a linear

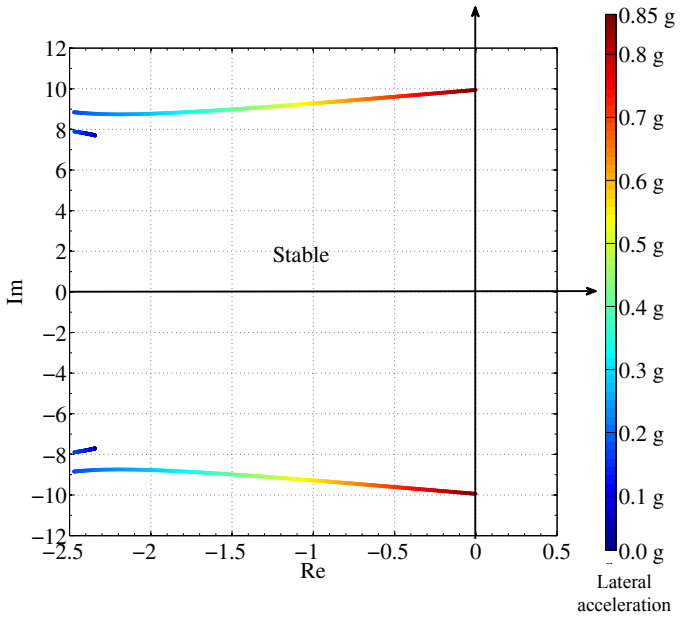

Figure 6.25: Movement of the largest conjugate eigenvalues in the complex plane while a_y varies from 0.0 g to 0.85 g.

system is uniquely defined by the nature of its equilibrium point, a nonlinear system may have more complex features such as periodic, quasi periodic or even chaotic motion. Understanding the limitations of Lyapunov's linearization method, the stability analysis of the nonlinear 4-DOF vehicle roll model follows in remainder of this thesis.

6.6.3 Stability Analysis of the Nonlinear 4-DOF Vehicle Roll Model

In the preceding section, using Lyapunov's linearization method, it has been shown that when the magnitude of the lateral acceleration a_y is less than 0.85 g, the nonlinear 4-DOF vehicle roll model has an asymptotically stable equilibrium point. In this

section, the behaviour of the nonlinear 4-DOF vehicle model for larger values of lateral acceleration, where Lyapunov's linearized method fails, will be discussed.

To demonstrate the nonlinear behaviour of the model, the projections of the attractors in $\phi - \omega_x$ subspace, when the lateral acceleration a_y varies from 0.849 g to 0.859 g with the step size 0.001 g, are plotted in Figure 6.26. As it can be seen, the attractor projection expands as the lateral acceleration increases. This expansion is the sign of a qualitative change in the steady-state behaviour, the type of attractor, for the nonlinear 4-DOF vehicle roll model. In simple words, it means that the attractor is not an equilibrium point any longer. This can be the explanation for the bouncing behaviour of the vehicle before tire-lift off occurs.

Among different methods to detect variations within the type of attractors, the concept of Lyapunov exponents is employed throughout the remaining part of this paper. The Lyapunov exponents are entities that measure the average rates of expansion or contraction of the nearby trajectories in the same basin of attraction, and they are independent of the initial conditions. The number of Lyapunov exponents is equal to the number of states that describe the dynamics in the state space. The sign of the Lyapunov exponents reveals the type of attractors for a dynamical system. If all the exponents are negative, the dynamics are exponentially stable and the attractor is an equilibrium point. A dynamic system with m zero exponents while the remaining exponents are negative, has an m-torus attractor. Finally, in a continuous time dynamic systems of the order larger than 3, a positive Lyapunov exponent is the sign of chaos. Monitoring the Lyapunov exponents makes it possible to distinguish between an equilibrium point or a periodic attractor as the lateral acceleration varies.

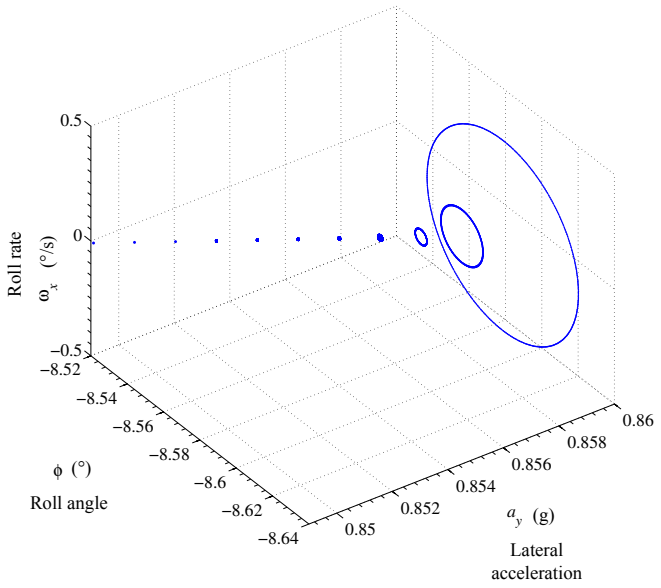

Figure 6.26: Qualitative change in the attractor projected in $\phi - \omega_x$ subspace while lateral acceleration a_y varies from 0.849 g to 0.859 g.

There are different algorithms to compute Lyapunov exponents. The method developed in [51] was used to calculate the spectrum of the Lyapunov exponents. This algorithm computes all Lyapunov exponents from the largest one to the smallest one. The number of Lyapunov exponents is equal to dimension of the dynamic system. The dimension of the nonlinear 4-DOF vehicle roll model in state space is eight; therefore, it has eight Lyapunov exponents. In the computation process of the Lyapunov exponents for the nonlinear 4-DOF vehicle model, the vehicle model was first accelerated laterally with a smooth ramp until it reached the desired constant lateral acceleration. This accelerating procedure is necessary to minimize the transient overshoot response and keeps the vehicle models stable. Then, the vehicle model states were disturbed by one percent of their steady-state values, and the Lyapunov exponents

computed for 4096 s with the step size of 0.01 s. To minimize the numerical error, the average value of each computed Lyapunov exponent for the last hundred steps were considered as the estimation of that individual Lyapunov exponent. Considering the above procedure, the spectrum of the Lyapunov exponents for different lateral acceleration from 0.800 g to 0.859 g with step size of 0.001 g were computed. For all of these lateral accelerations, the tires' deflection was monitored to make sure that the switching between models does not occur.

In Figure 6.27, the dynamic graphs for the fourth largest Lyapunov exponents are plotted. The diagram for the first and second Lyapunov exponents shows that these two Lyapunov exponents approach zero as the lateral acceleration increases. When the lateral acceleration is between 0.858 g to 0.859 g, first and second Lyapunov exponents are zero showing that the vehicle model attractor around these values of the lateral acceleration is a 2-torus.

6.7 Summary

The aim of this chapter was to analysis the Lyapunov stability of a new developed vehicle roll model. The model has 4-DOF, and it was developed as a proper nonlinear model for Lyapunov stability analysis with small dimensions and adequate realistic behaviour. The nonlinear 4-DOF vehicle roll model was developed by decoupling the yaw and roll motions of the conventional nonlinear 14-DOF full vehicle model. The new model captured the information of the neglected dynamics through the lateral acceleration, and it was capable of predicting the roll motion even after tire lift-off

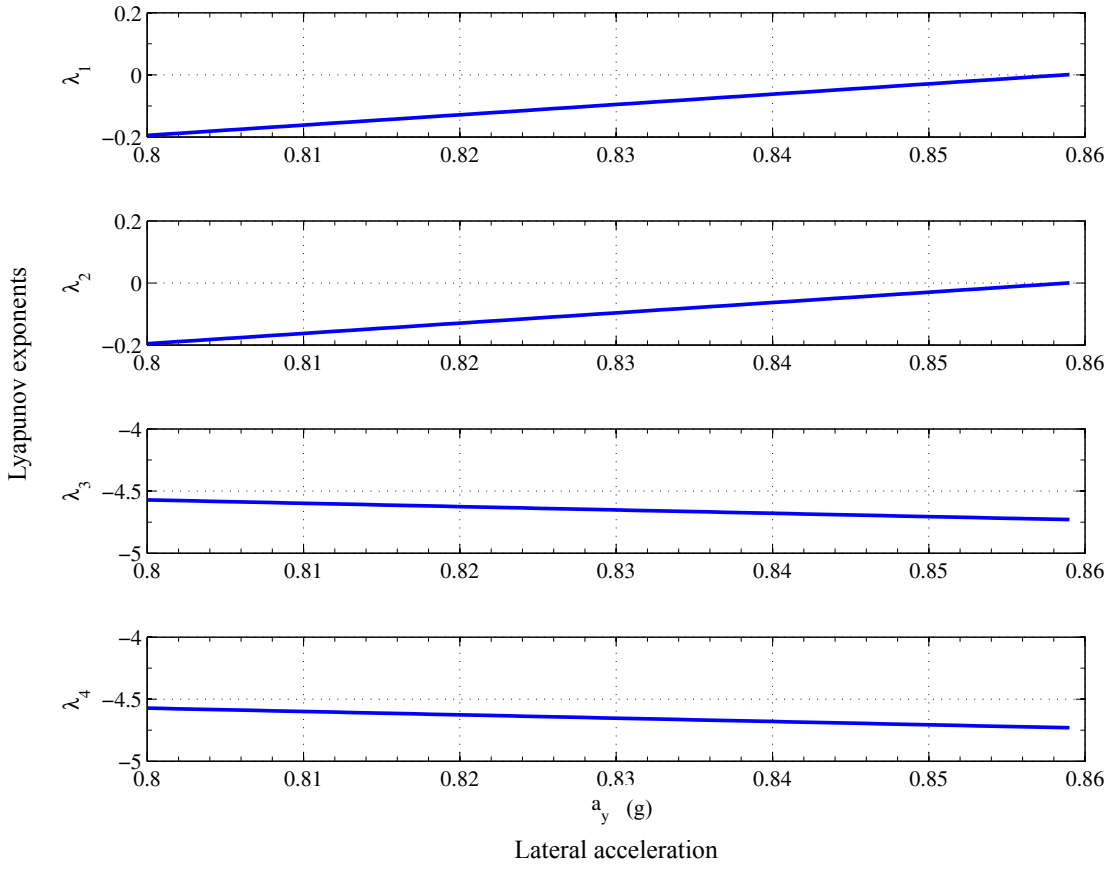

Figure 6.27: Dynamics of fourth largest Lyapunov exponents while the lateral acceleration a_y varies from 0.800 g to 0.859 g.

occurs. To verify the new model, the roll variable responses were compared with the nonlinear 14-DOF vehicle model for different maneuvers. The results prove the accuracy of the nonlinear 4-DOF vehicle roll model for predicting the roll motion. It was shown when the tires on the right-hand side of the model leave the ground, another set of nonlinear equations are replaced to predict the roll behaviour. However, it is possible to represent the model with only one set of equations after adding another state for the deflection of the tire at the left-hand side. The switching between equations

was necessary for minimum realization of the model to make the stability analysis easier. The nonlinear 4-DOF vehicle roll model was linearized, and the Lyapunov stability of the intended equilibrium point was studied. The trend of equilibrium point movement as the lateral acceleration varies were investigated. After discussion on limitation of the Lyapunov's linearization method, the concept of Lyapunov exponents was used to detect the qualitative change in type of attractors happens in large values of the lateral acceleration. Considering the dimensions of the nonlinear 4-DOF vehicle roll model and implemented stability analysis, it is reasonable to employ this model in developing roll active safety system for future study.

Chapter 7

Conclusions and Future Work

7.1 Conclusions

In this thesis: a) a new measure of dynamics called "modified Lyapunov exponents" has been defined that provides more insight into stability analysis of the nonlinear systems, b) the concept of Lyapunov exponents has been introduced to the vehicle dynamics community as a constructive method for stability analysis of nonlinear vehicle models, c) the nonlinear 4-DOF vehicle roll model as a proper nonlinear vehicle roll model for Lyapunov stability analysis has been developed, and d) the SETV has been developed as a vehicle test bed with unique features for rollover experiments. This thesis can be concluded in four-fold as follows.

The modified Lyapunov exponents were defined, and their existence and invariant property have been proven by theorem of the modified Lyapunov exponents. The concept of modified Lyapunov exponent have been demonstrated in various case studies.

It has been shown how these exponents can provide additional insight of nonlinear dynamics over the conventional Lyapunov exponents.

The concept of Lyapunov exponents has been applied to system and structure Lyapunov stability analysis of the well-known nonlinear bicycle vehicle model. The results verified the promised advantages of this concept over other available tools, including the Lyapunov direct method.

Considering the absence of a suitable realistic vehicle model for roll stability analysis, a nonlinear 4-DOF vehicle roll model with minimum realization has been developed. Through simulations and an experiment, It has been shown that this model is capable of modelling the realistic roll motion of vehicles. To avoid blind simulations and misunderstanding, the Lyapunov stability of the model has been analyzed by Lyapunov linearization and Lyapunov exponents methods. It has been shown that the concept of Lyapunov exponents can tackle the limitation of the Lyapunov linearization method and provide more information on behaviour of the vehicle model.

As an experimental test bed for rollover study, the SETV was designed and built. The electrical and mechanical components of the SETV have been introduced, and their functions have been discussed. The SETV was driven in a cornering maneuver such that the rollover occurred. The collected acceleration data was fed to the nonlinear 4-DOF vehicle model. It has been shown that the roll rate graph predicted by the vehicle model is close to the measured data; moreover, the model is capable of predict the rollover accident.

The thesis has a number of contributions. In the field of nonlinear dynamic analysis, the thesis contributed with the modified Lyapunov exponents. These exponents are

introduced as new measures of dynamics that can provide more information from nonlinear dynamics. The contribution of this thesis in the vehicle society includes: a) suggesting the concept of Lyapunov exponents as a powerful tool for stability analysis of the vehicle models, b) developing a proper vehicle roll model for Lyapunov stability analysis with adequate realistic behaviour, c) developing a scale experimental test vehicle with unique features for roll motion studies.

7.2 Future Work

The presented work in this thesis has the potential to be extended in both nonlinear system dynamics and vehicle dynamics area.

The concept of modified Lyapunov exponent may be employed to find the borders of the stability region. In the large dynamic systems, finding the edge of the stability region is very time-consuming and some algorithms are developed to speed up the searching process. The modified Lyapunov exponents may give some insight about the appropriate directions to search.

In stability analysis or chaos controller design, the information about the dominant sub-systems is important. The modified Lyapunov exponents can be considered to identify the dominant sub-systems.

Moreover, the identification of dominant sub-systems may also be used to reduce the computational load required for calculating Lyapunov exponents.

The nonlinear 4-DOF vehicle roll model can be considered as the plant for designing controllers or warning systems. This model is precise, and it benefits from the advan-

tages includes: a) the small dimension, and b) less complex dynamics in comparison with other realistic models. Additionally, this model can be used in real-world applications since it is reasonably fast, and it only needs one time series measured by an accelerometer.

Finally, the SETV is a versatile test bed to be used for other vehicle dynamics studies with minor development. However, improving the steering system with a closed-loop controller to guarantee the precise steering is commendable.

Appendix A

Vehicle Models Predicting Roll Motion

A.1 Overview

In the literature, a number of vehicle models have been introduced, which represent the roll motion of the vehicles [6, 7, 10, 18, 73–79]. Depending on the consideration of the roll acceleration, these models can be classified into two groups; a) those representing the quasi-static roll motion and b) those also including the transient roll motion. In another sense, regardless of the quasi-static or transient representation, someone can categorize the roll models into three types a) those considering only the roll motion of the sprung mass, b) those that assuming same roll motion for the sprung mass and the unsprung mass, and c) those that consider different roll motions for the sprung mass and the unsprung mass. In subsequent sections; well-known

models in quasi-static and transient categories will be introduced.

A.2 Quasi-Static Roll Models

In quasi-static models, it is assumed that the vehicle is in the steady turn, and the change in the lateral acceleration is reasonably low in comparison with the vehicle roll response. These models include: a) the rigid vehicle, b) the suspended vehicle, c) the compliant tire vehicle, and d) the suspended-compliant tire vehicle. In subsequent parts, these models are briefly presented, however; an interested reader may refer to [12] for more details.

A.3 Rigid Vehicle Model

Rigid vehicle model, shown in Figure A.1, is the simplest roll plane model which has no degree of freedom and gives the theoretical upper bound for both yaw and roll stabilities.

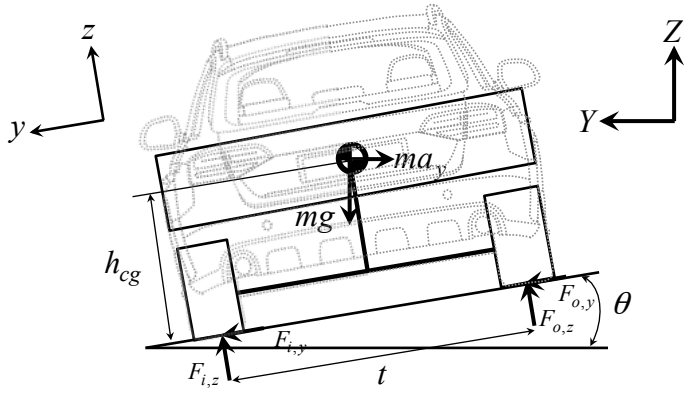

Figure A.1: Rigid vehicle model

Writing the force equilibriums in the y- and z-directions, the yaw stability limit in terms of lateral acceleration a_y can be derived as

$$\frac{a_y^{\psi}}{g} = \frac{\tan\theta + f}{1 - f\tan\theta} \tag{A.1}$$

where f is the coefficient of friction, and θ is the superelevation of the road. In above formula it has been assumed that the vehicle travels with a constant longitudinal speed where all the available friction is used for cornering. The yaw stability limit is always used for road geometry design purposes [80]. It is notable that the yaw stability limits for subsequent models are same as Eq. A.1.

The roll stability limit is defined in terms of lateral acceleration a_y and can be derived by writing the moment equilibrium about the outside tire contact point with road at the instance of lift-off of the inside where $F_{i,z} = 0$ and $a_y = a_y^{\phi}$ as

$$\frac{a_y^{\phi}}{g} = \frac{\tan\theta + \frac{t}{2h_{cg}}}{1 - \frac{t}{2h_{cg}}\tan\theta} \tag{A.2}$$

If the superelevation is neglected, the remaining terms will represent the vehicle contribution to the rollover as

$$\frac{a_y^{\phi}}{g} = \frac{t}{2h_{cg}} \tag{A.3}$$

Equation A.3 is known as Static Stability Factor (SSF) or Track Width Ratio (TWR) in the literature.

A.4 Suspended Vehicle Model

The suspended vehicle model, as shown in Figure A.2 [78] includes roll degree of freedom for the suspension which represents the rotation of the sprung mass about

the kinematic roll axis that is the line joining the front and rear roll centres [7] as shown in Figure A.3. In fact, this model includes the lateral load transfer where shift the centre of the gravity toward the outside of the turn. In this model, it is assumed that the unsprung mass is much stiffer than the suspension, and therefore, it never rotates and always stays parallel with the road surface. Another presumption is that the unsprung mass is negligible in comparison with the sprung mass.

The roll stability limit for this model can be derived from the moment equilibrium around the outer tire contact point at the moment of inner tire lift-off. Assuming the small angles, it is formulated as

$$\frac{a_y^{\phi}}{g} = \frac{\theta\left[h_{cg,s} + \left(h_{cg,s} - h_{rc}\right) R_{\phi}\right] + \frac{t}{2}}{h_{cg,s} + \left(h_{cg,s} - h_{rc}\right) R_{\phi} - \theta\frac{t}{2}} \tag{A.4}$$

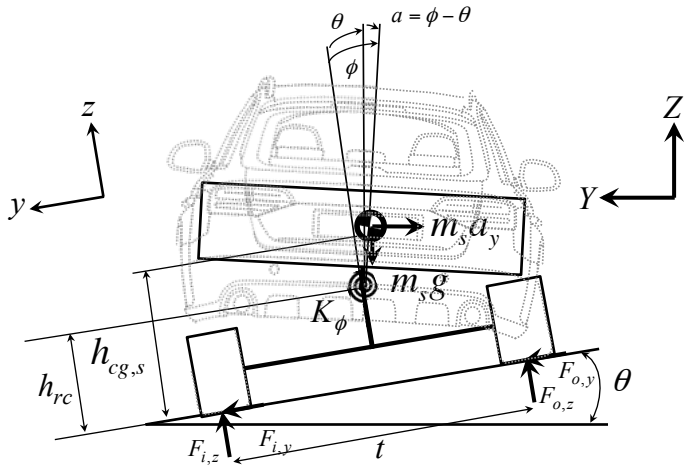

Figure A.2: Suspended vehicle model

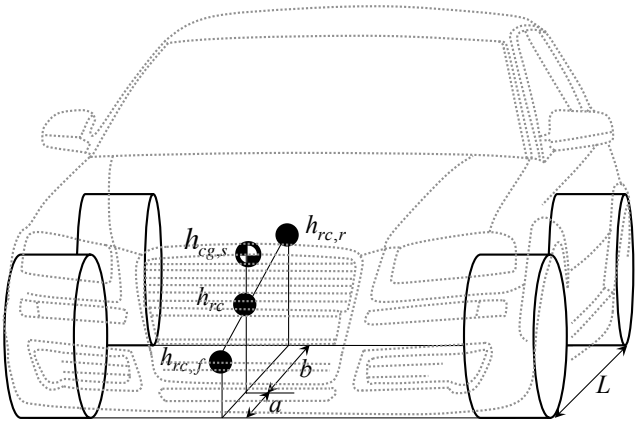

Figure A.3: Roll axis of the vehicle

where R_ϕ is the vehicle roll gain (roll rate or roll gradient) giving the amount of sprung mass body rolls per unit applied lateral acceleration. Writing the moment equilibrium around the roll centre for the sprung mass and considering small angles, roll gain can be derived as

$$R_\phi \equiv \frac{\phi}{a_y/g - \theta} = \frac{1}{\frac{K_\phi}{m_s g(h_{cg,s} - h_{rc})} - 1} \tag{A.5}$$

A.5 Compliant Tire Vehicle Model

Figure A.4 exhibits the compliant tire vehicle model. As it can be seen this model consists of a rigid vehicle with vertical tire compliance that allows the vehicle to roll about an axis. However, it is assumed that the tires are always normal to the road surface.

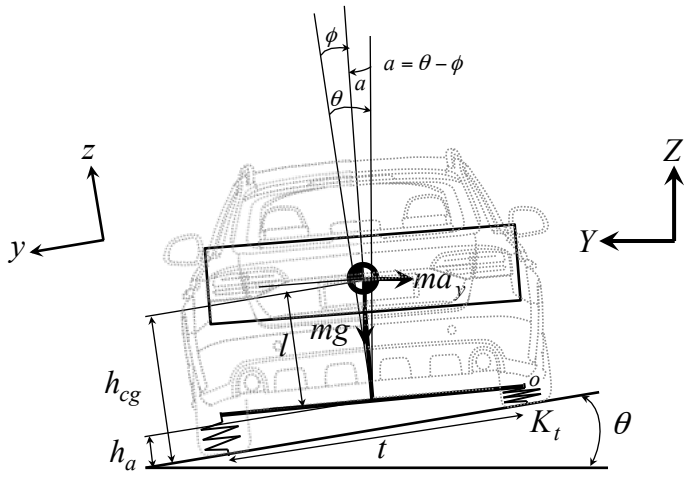

Figure A.4: Compliant tire vehicle model

The moment equilibrium about the outside axle spindle at the instance of inner tire lift-off leads to the roll stability limit as given in Eq. A.6.

$$\frac{a_y^{\phi}}{g} = \frac{-l\tan\alpha + \frac{t}{2}}{l + \frac{t}{2}\tan\alpha} \tag{A.6}$$

where l is

$$l = \frac{h_{cg} - h_a}{\cos\left(\phi^{\phi}\right)} \tag{A.7}$$

A.6 Suspended-Compliant Tire Vehicle Model

In suspended-compliant tire vehicle model [13] (see Figure A.5), both a roll degree of freedom of the suspension (connection between the sprung and unsprung mass) and tire vertical compliances are included.

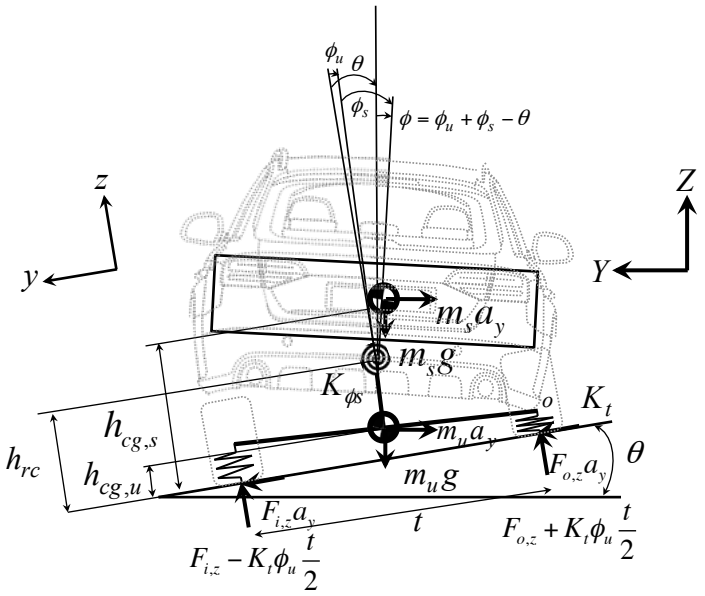

Figure A.5: Suspended-compliant tire vehicle model

A.7 Transient Roll Models

To demonstrate the vehicle roll response to the rapidly changing lateral acceleration, the model should be able to represent the roll varies with time. Such a model is known as the transient roll model. Transient roll models can be derived by considering the dynamics of the quasi-statics rollover models in Sections. A.4, A.5, and A.6. For example, if someone includes the roll moment of inertia I_{xx} of the sprung mass to the suspended vehicle roll model, this model can be used for examining the vehicle response to the suddenly applied lateral accelerations [7].

The dynamic equations of the suspended-compliant tire vehicle model (2-DOF, 4 states variable) can be seen in [13].

A.8 Vehicle Models Representing Coupled Yaw and Roll Motion

There are some comprehensive models that combine motions in the yaw and the roll planes. Depending on the applications, these models may consider the roll motion of the sprung mass or the roll motion of the combined sprung and unsprung masses.

A.9 Yaw-Roll Model Considering the Roll Motion of the Sprung Mass

This type of combined yaw-roll models neglects the roll motion of the unsprung mass. They can be used for studying vehicle handling in maneuvers that the tire lift-off does not occur [18]. Figure A.6 shows such a model in 3-DOF configuration (roll, yaw, side slip angle) and integrated unsprung mass where its dynamic equations can be found in [6, 9]. A full model (8-DOF) including wheel spins and un-concentrated unsprung masses [18] is given Figure A.7.

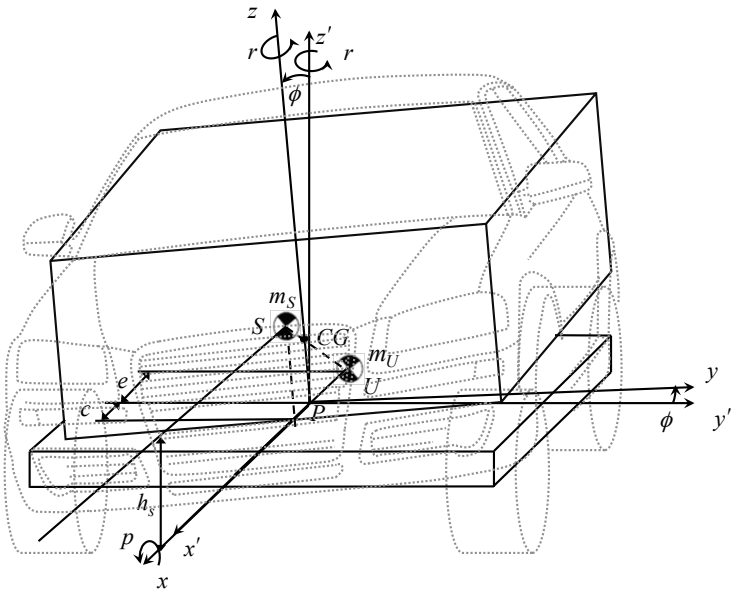

Figure A.6: 3-DOF yaw-roll vehicle model

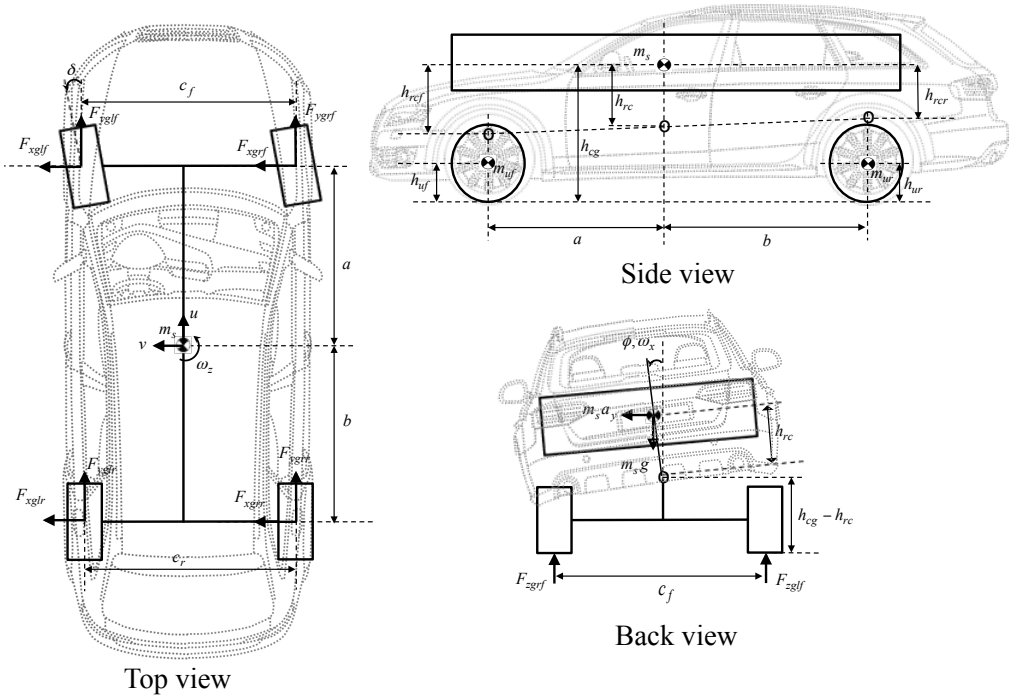

Figure A.7: 8-DOF yaw-roll full vehicle model

A.9. YAW-ROLL MODEL CONSIDERING THE ROLL MOTION OF THE SPRUNG MASS

The pitch and heave motion of the vehicle is not modelled in the 8-DOF vehicle model, however; in [18] it is noted that in the case of handling maneuvers, in which the vehicle does not experience significant longitudinal accelerations, the result from this model is reasonably matched with the 14-DOF full vehicle model.

Appendix B

Reconstruction of the 14-DOF Full Vehicle Model

B.1 Overview

In this Appendix, the 14-DOF full vehicle model which is introduced in Section 3.3.3 will be reconstructed. It will be used as the reference model for further study on the stability analysis of the roll motion of the vehicle model. To make the process of the modelling easier to understand, despite the original work, this chapter starts with expressing general equation of motions in 3D space, and followed by derivation of the velocities, forces and torques. It is notable that only the equations for the left rear corner of the vehicle (lr) is derived here. Since the dynamics of the other corners can be derived in the same manner, they are not presented.

B.2 Reconstruction of the 14-DOF Full Vehicle Model

The reconstruction of the 14-DOF full vehicle model [5] (see Figure B.1) starts by writing the 3D general equation of motions [81] in a frame (x, y, z) (body-fixed frame). This coordinate is attached to the CG of the sprung mass (rigid body), and the coordinate axes coincide with the principal axes of inertia (see Figure B.2).

Equation B.1 describes 6-DOF related to the sprung mass where F_x, F_y, and F_z are the external forces along x, y, z directions. τ_x, τ_y, and τ_z are the external moments around x, y, z axes. It should be noted that in the original work, some angular velocity products have been omitted in Euler's equations while they have been included in reconstruction those equations in this chapter.

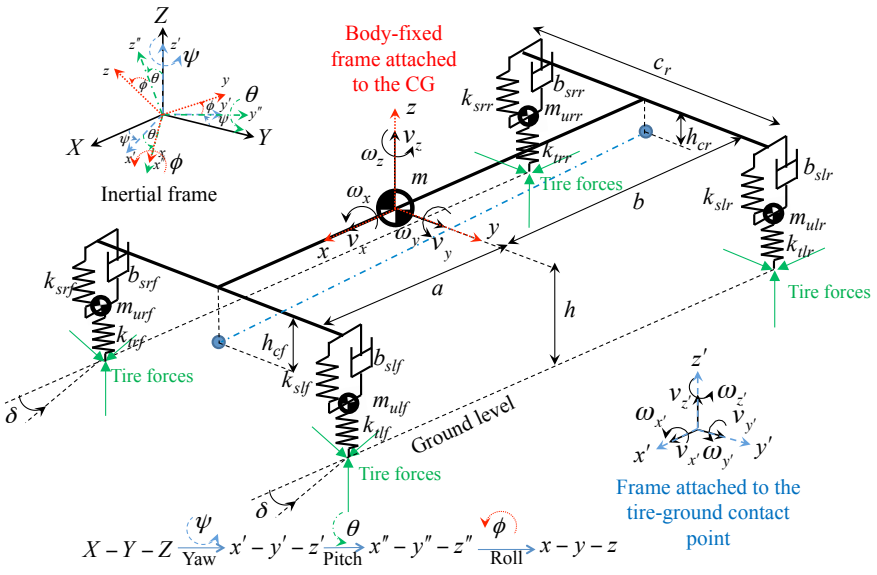

Figure B.1: Schematic view of the 14-DOF full vehicle model[1]

[1]Subscript ij denotes left front (lf), right front (rf), left rear (lr), and right rear (rr).

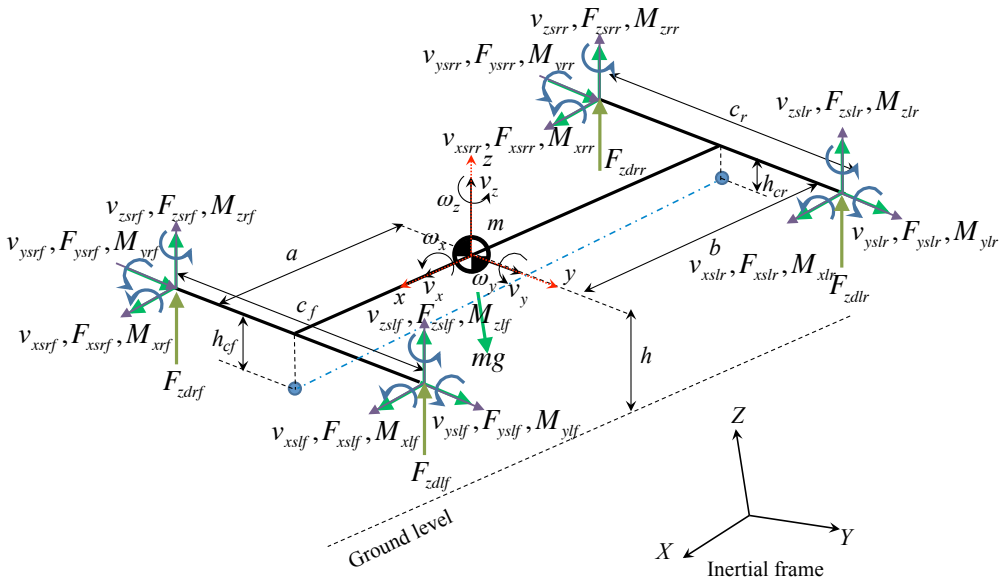

Figure B.2: Free body diagram of the sprung mass

$$
\begin{aligned}
F_x &= m\dot{v}_x + m\omega_y v_z - m\omega_z v_y \\
F_y &= m\dot{v}_y + m\omega_z v_x - m\omega_x v_z \\
F_z &= m\dot{v}_z + m\omega_x v_y - m\omega_y v_x \\
\tau_x &= J_x\dot{\omega}_x + \omega_y J_z \omega_z - \omega_z J_y \omega_y \\
\tau_y &= J_y\dot{\omega}_y + \omega_z J_x \omega_x - \omega_x J_z \omega_z \\
\tau_z &= J_z\dot{\omega}_z + \omega_x J_y \omega_y - \omega_z J_x \omega_x
\end{aligned}
\tag{B.1}
$$

By solving these equations, $v_x,\ v_y,\ v_z,\ \omega_x,\ \omega_y,\ \omega_z$ will be known with the respect to the body-fixed frame, which changes directions at every time instant. Moreover, the force and the torque components must be aligned with axes of this frame. To overcome above problems they will be transferred from body-fixed frame to the inertial frame $(X,\ Y,\ Z)$ through transformations. The body-fixed frame $(x,\ y,\ z)$ can be derived by first rotating the inertial frame about the Z through angle ψ (yaw), resulting in the frame $(x',\ y',\ z')$ attached to the ground at the tire-ground contact point. Next rotating the $(x',\ y',\ z')$ frame about the y' axis through angle θ (pitch) yields the frame $(x'',\ y'',\ z'')$ and finally rotating around x'' through the angle ϕ (roll) yields to the instantaneous body-fixed frame $(x,\ y,\ z)$. The equivalent transformation matrices are given in Eq. B.2.

$$\boldsymbol{\phi} = \begin{bmatrix} 1 & 0 & 0 \\ 0 & \cos\ \phi & -\sin\ \phi \\ 0 & \sin\ \phi & \cos\ \phi \end{bmatrix}$$

$$\boldsymbol{\theta} = \begin{bmatrix} \cos\ \theta & 0 & \sin\ \theta \\ 0 & 1 & 0 \\ -\sin\ \theta & 0 & \cos\ \theta \end{bmatrix} \tag{B.2}$$

$$\boldsymbol{\psi} = \begin{bmatrix} \cos\ \psi & -\sin\ \psi & 0 \\ \sin\ \psi & \cos\ \psi & 0 \\ 0 & 0 & 1 \end{bmatrix}$$

Therefore, the angular velocities can be represented in frames $(x'',\ y'',\ z'')$, $(x',\ y',\ z')$,

and $(X,\ Y,\ Z)$ as

$$\begin{bmatrix} \omega_{x''} \\ \omega_{y''} \\ \omega_{z''} \end{bmatrix} = \boldsymbol{\phi} \begin{bmatrix} \omega_x \\ \omega_y \\ \omega_z \end{bmatrix}$$

$$\begin{bmatrix} \omega_{xg} \\ \omega_{yg} \\ \omega_{zg} \end{bmatrix} \triangleq \begin{bmatrix} \omega_{x'} \\ \omega_{y'} \\ \omega_{z'} \end{bmatrix} = \boldsymbol{\theta}\ \boldsymbol{\phi} \begin{bmatrix} \omega_x \\ \omega_y \\ \omega_z \end{bmatrix} \tag{B.3}$$

$$\begin{bmatrix} \omega_X \\ \omega_Y \\ \omega_Z \end{bmatrix} = \boldsymbol{\psi}\ \boldsymbol{\theta}\ \boldsymbol{\phi} \begin{bmatrix} \omega_x \\ \omega_y \\ \omega_z \end{bmatrix}$$

For transforming velocity components the same relationship exists, therefore

$$\begin{bmatrix} v_X \\ v_Y \\ v_Z \end{bmatrix} = \boldsymbol{\psi}\ \boldsymbol{\theta}\ \boldsymbol{\phi} \begin{bmatrix} v_x \\ v_y \\ v_z \end{bmatrix} \tag{B.4}$$

The force and the torque components in different frames also have the same relationship; therefore, the force and the torque components can transfer from the inertial

frame ($X,\ Y,\ Z$) to the body-fixed frame ($x,\ y,\ z$) as

$$\begin{bmatrix} F_x \\ F_y \\ F_z \end{bmatrix} = \boldsymbol{\phi}^T\ \boldsymbol{\theta}^T\ \boldsymbol{\psi}^T \begin{bmatrix} F_X \\ F_Y \\ F_Z \end{bmatrix}$$

$$\begin{bmatrix} \tau_x \\ \tau_y \\ \tau_z \end{bmatrix} = \boldsymbol{\phi}^T\ \boldsymbol{\theta}^T\ \boldsymbol{\psi}^T \begin{bmatrix} \tau_X \\ \tau_Y \\ \tau_Z \end{bmatrix} \tag{B.5}$$

The angles ψ, θ, and ϕ change with time and their differential equations can be related to the body-fixed components ω_x, ω_y, and ω_z as

$$\dot{\psi} = \ \tfrac{\sin\ \phi}{\cos\ \theta}\ \omega_y\ +\ \tfrac{\cos\ \phi}{\cos\ \theta}\ \omega_z$$

$$\dot{\theta} = \ \cos\ \phi\ \omega_y\ -\ \sin\ \phi\ \omega_z \tag{B.6}$$

$$\dot{\phi} = \ \omega_x\ +\ \sin\ \phi\ \tfrac{\sin\ \theta}{\cos\ \theta}\ \omega_y\ +\ \cos\ \phi\ \tfrac{\sin\ \theta}{\cos\ \theta}\ \omega_z$$

The total external forces acting on the sprung mass in the x-direction is

$$F_x = \ F_{xsrf}\ +\ F_{xslf}\ +\ F_{xsrr}\ +\ F_{xsrr}\ +\ mg\sin\ \theta \tag{B.7}$$

and the total roll moments around the x-axis produced by the external forces acting on the sprung mass is

$$\tau_x = \ M_{xrf}\ +\ M_{xlf}\ +\ M_{xrr}\ +\ M_{xrl}\ +\ \frac{(F_{zslf} + F_{Fzslr} - F_{zsrf} - F_{zsrr})\,c}{2} \tag{B.8}$$

where it is assumed that $c = c_f = c_r$.

The total external forces acting on the sprung mass in the y-direction is

$$F_y = F_{ysrf} + F_{yslf} + F_{ysrr} + F_{ysrr} + mg \sin \phi \cos \theta \tag{B.9}$$

and the total pitch moments around the y-axis produced by the external forces acting on the sprung mass is

$$\tau_y = M_{yrf} + M_{ylf} + M_{yrr} + M_{yrl} + (F_{zslr} + F_{Fzsrr})\, b - (F_{zslf} + F_{zsrf})\, a \tag{B.10}$$

The total external forces acting on the sprung mass in the z-direction is

$$F_z = F_{zsrf} + F_{zslf} + F_{zsrr} + F_{zslr} \; F_{dzrf} + F_{dzlf} + F_{dzrr} + F_{dzlr} - mg \cos \phi \cos \theta \tag{B.11}$$

and the total roll moments around the z-axis produced by the external forces acting on the sprung mass is

$$\tau_z = M_{zrf} + M_{zlf} + M_{zrr} + M_{zrl} + (F_{yslf} + F_{Fysrf})\, a - (F_{yslr} + F_{zyrr})\, b + \frac{\left(-F_{xslf} + F_{xsrf} - F_{xslr} + F_{xsrr}\right) c}{2} \tag{B.12}$$

The procedure of finding the force and the velocity components acting on each side of the sprung mass are the same; therefore, only those acting on the left rear corner of the vehicle will be found; however, the equations for all sides and axles must be determined in the simulations.

The reconstruction process starts by finding the force equations and then determining the velocities used in them. Finally, the transformed moments to the sprung mass will be determined, and the tire lift-off condition will be applied.

B.2.1 Force Equations

Figure B.3 shows the free body diagram of the unsprung mass on the left rear corner of the vehicle.

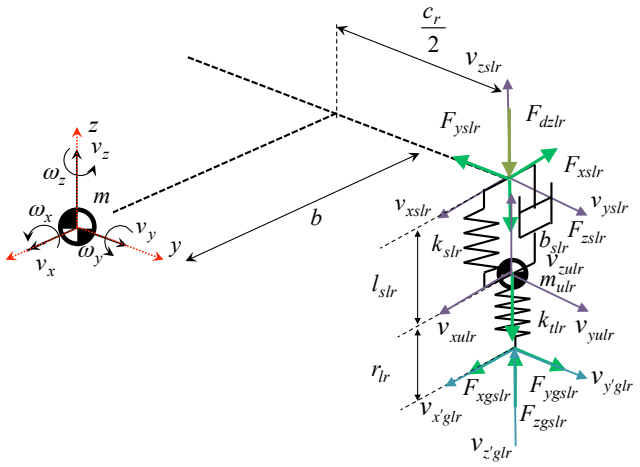

Figure B.3: Free body diagram of the unsprung mass on the left rear corner of the vehicle

By writing the Newton's equation of motions along x and y directions for the unsprung mass on the left rear corner of the vehicle

$$F_{xulr} = m_{ulr}\dot{v}_{xulr} + m_{ulr}\omega_y v_{zulr} - m_{ulr}\omega_z v_{yulr} \tag{B.13}$$

$$F_{yulr} = m_{ulr}\dot{v}_{yulr} + m_{ulr}\omega_z v_{xulr} - m_{ulr}\omega_x v_{zulr}$$

where

$$F_{xulr} = -F_{xslr} + F_{xgslr} + m_{ulr} g \sin\ \theta \tag{B.14}$$

$$F_{yulr} = -F_{yslr} + F_{ygslr} - m_{ulr} g \sin\ \phi\ \cos\ \theta$$

Therefore,

$$F_{xslr} = F_{xgslr} + m_{ulr} g \sin\ \theta - m_{ulr} \dot{v}_{xulr}\ -\ m_{ulr} \omega_y v_{zulr}\ +\ m_{ulr} \omega_z v_{yulr}$$

$$F_{yslr} = F_{ygslr} - m_{ulr} g \sin\ \phi\ \cos\ \theta - m_{ulr} \dot{v}_{yulr}\ -\ m_{ulr} \omega_z v_{xulr}\ +\ m_{ulr} \omega_x v_{zulr} \tag{B.15}$$

The vertical force F_{zslr} is

$$F_{zslr} = x_{slr} k_{slr}\ +\ \dot{x}_{slr} b_{slr} \tag{B.16}$$

where x_{slr} is the instantaneous suspension spring deflection. The ground forces F_{xgslr}, F_{ygslr}, and F_{zgslr} in the body-fixed frame (x, y, z) can be found by ground forces $F_{x'glr}$, $F_{y'glr}$, and $F_{z'glr}$ in the frame (x', y' , z') as

$$\begin{bmatrix} F_{xgslr} \\ F_{ygslr} \\ F_{zgslr} \end{bmatrix} = \boldsymbol{\phi}^T\ \boldsymbol{\theta}^T \begin{bmatrix} F_{x'glr} \\ F_{y'glr} \\ F_{z'glr} \end{bmatrix} \tag{B.17}$$

The ground forces $F_{x'glr}$, and $F_{y'glr}$ depend on the tire longitudinal and lateral forces and steering angle, δ, as shown in Figure B.4.

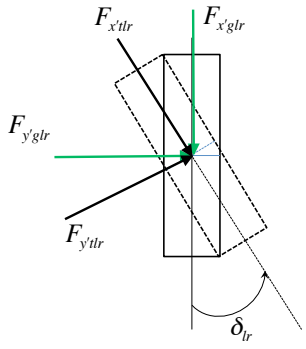

Figure B.4: Forces at the tire contact patch

$$F_{x'glr} = F_{x'tlr}\cos\ \delta - F_{y'tlr}\sin\ \delta_{lr}$$
$$F_{y'glr} = F_{y'tlr}\cos\ \delta + F_{x'tlr}\sin\ \delta_{lr} \tag{B.18}$$

where $\delta_{lr} = 0$ (no steering on the rear wheels).

The tire forces can be found by an empirical method known as the Magic Formula that fits experimental data to describe the relationship between the cornering force ($F_{y'tlr}$) and the sideslip angle, or the longitudinal force ($F_{x'tlr}$) and the longitudinal skid.

To calculate the cornering force, $F_{y'tlr}$, the side slip angle of the left rear tire in Equation B.19 must be inserted instead of x in the Magic Formula.

$$\alpha_{lr} = \arctan\ \left(\frac{v_{y'glr}}{v_{x'glr}}\right)\ -\ \delta_{lr} \tag{B.19}$$

To calculate the longitudinal skidding force, $F_{x'tlr}$, the x in Magic formula must be replaced by longitudinal skid of the left rear tire, s_{lr}, given in Equation B.20.

$$s_{lr} = \frac{(r_{lr}\omega_{lr}\ -\ (v_{x'glr}\ \cos\ \delta_{lr}\ +\ v_{y'glr}\sin\ \delta_{lr}))}{|(v_{x'glr}\cos\ \delta_{lr}\ +\ v_{y'glr}\sin\ \delta_{lr})|} \tag{B.20}$$

Assuming that the vertical stiffness of tire, k_{tlr}, remains normal to the ground, the vertical force $F_{z'glr}$ is equal to

$$F_{z'glr} = F_{z'tlr} = x_{tlr}k_{tlr} \tag{B.21}$$

where x_{tlr} is the instantaneous tire deflection in frame (x', y', z') or in the inertial frame (X, Y, Z).

The jacking force F_{dzlr} which is produced due to the lateral force F_{ygslr} depends on the type of independent suspension, which will be discussed in Section B.2.3.

B.2.2 Velocity Equations

The spring deflection x_{slr} in Eq. B.16 can be expressed as

$$\dot{x}_{slr} = v_{zulr} - v_{zslr} \tag{B.22}$$

The initial deflection of the suspension, x_{sir}, is determined from the static equation as

$$x_{sir} \;=\; \frac{mga}{2\,(a \;+\; b)\,(k_{slr} \;+\; k_{srr})} \tag{B.23}$$

The velocity v_{zulr} represents 1-DOF related to the vertical deflection of the suspension. It can be determined by applying the Newton's equation of motion for the vertical direction of the unsprung mass

$$F_{zulr} = \; m_{ulr}\dot{v}_{zulr} + m_{ulr}\omega_x v_{yulr} \;-\; m_{ulr}\omega_y v_{xulr} \tag{B.24}$$

F_{zulr} is the total external force along the z-axis (see Figure B.3)

$$F_{zulr} = \; -F_{zslr} \;+\; F_{zgslr} \;-\; F_{dzlr} \;-\; m_{ulr}g\cos\;\theta\cos\;\phi \tag{B.25}$$

and therefore, from Eq. B.24 and Eq. B.16

$$\begin{aligned} m_{ulr}\dot{v}_{zulr} = \; & -m_{ulr}\omega_x v_{yulr} \;+\; m_{ulr}\omega_y v_{xulr} \;+\; F_{zgslr} \;-\; F_{dzlr} \\ & - x_{slf}k_{slf} \;-\; \dot{x}_{slf}b_{slf} \;-\; m_{ulr}g\cos\;\theta\cos\;\phi \end{aligned} \tag{B.26}$$

where from Eq. B.17, F_zgslr is

$$F_{zgslr} = F_{x'glr}\cos\theta\cos\phi - F_{y'glr}\sin\phi + F_{z'glr}\cos\theta\cos\phi \tag{B.27}$$

The tire deflection x_{tlr} obeys Eq. B.28 as

$$\dot{x}_{tlr} = v_{z'glr} - v_{z'gulr} \tag{B.28}$$

where the initial deflection of the tires in the rear axle, x_{its}, is determined from the static equation as

$$x_{tir} = \frac{\left(\frac{mga}{2(a+b)}\right) + (m_{ulr}g + m_{urr}g)}{k_{tlr} + k_{trr}} \tag{B.29}$$

The velocity $v_{z'gulr}$ can be found by transferring $v_{xulr},\ v_{yulr},\ v_{zulr}$ from the body-fixed frame $(x,\ y,\ z)$ to the frame $(x',\ y',\ z')$ by

$$\begin{bmatrix} v_{x'gulr} \\ v_{y'gulr} \\ v_{z'gulr} \end{bmatrix} = \boldsymbol{\theta}\ \boldsymbol{\phi} \begin{bmatrix} v_{xulr} \\ v_{yulr} \\ v_{zulr} \end{bmatrix} \tag{B.30}$$

Therefore,

$$v_{z'gulr} = -v_{xulr}\sin\theta + v_{yulr}\cos\theta\sin\phi + v_{zulr}\cos\theta\cos\phi \tag{B.31}$$

Assuming that the vehicle is driven on a smooth road, $v_{z'glr} = 0$, Eq. B.28 will be reduced to

$$\dot{x}_{tlr} = v_{xulr}\sin\theta - \cos\theta\ (\ v_{yulr}\sin\phi + v_{zulr}\cos\phi) \tag{B.32}$$

The longitudinal velocity v_{xulr} of the unsprung mass as well as lateral velocity v_{yulr} of the unsprung mass (see Figure B.5) in the body-fixed frame $(x,\ y,\ z)$ can be found by

$$v_{xulr} = v_{xslr} - l_{slr}\,\omega_y \tag{B.33}$$

and

$$v_{yulr} = v_{yslr} \; + \; l_{slr}\, \omega_x \tag{B.34}$$

The $\dot{v}_{xulr}$ and $\dot{v}_{yulr}$ in Eq. B.15 are determined by

$$\dot{v}_{xulr} = \dot{v}_x \; - \; \frac{c_r}{2}\dot{\omega}_z \; + \; \dot{x}_{slr}\omega_y \; - \; \dot{\omega}_y l_{slr} \tag{B.35}$$

and

$$\dot{v}_{yulr} = \dot{v}_y \; - \; b\dot{\omega}_z \; - \; \dot{x}_{slr}\omega_x \tag{B.36}$$

respectively.

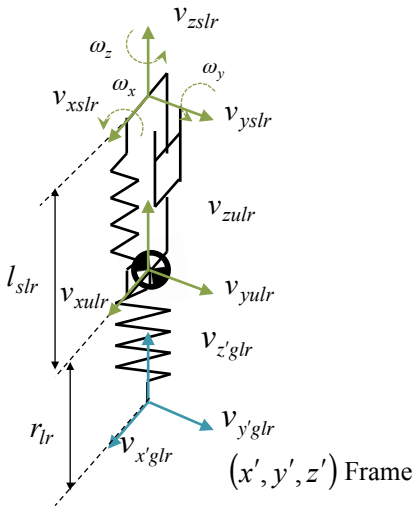

Figure B.5: Unsprung mass velocities

The velocities of the left rear strut mounting point in the body-fixed frame ($x,\ y,\ z$), v_{xslr}, v_{yslr}, and v_{zslr}, (see Figure B.3) can be determined by

$$\begin{bmatrix} v_{xslr} \\ v_{yslr} \\ v_{zslr} \end{bmatrix} = \begin{bmatrix} v_x \\ v_y \\ v_z \end{bmatrix} + \begin{bmatrix} 0 & 0 & \frac{-c_r}{2} \\ 0 & 0 & -b \\ \frac{c_r}{2} & b & 0 \end{bmatrix} \begin{bmatrix} \omega_x \\ \omega_y \\ \omega_z \end{bmatrix} \tag{B.37}$$

where it is assumed that $c = c_r = c_f$.

The longitudinal velocity $v_{x'glr}$, and the lateral velocity $v_{y'glr}$ at the tire contact patch in Eq. B.19 and Eq. B.20 are

$$\begin{bmatrix} v_{x'glr} \\ v_{y'glr} \\ v_{z'glr} \end{bmatrix} = \boldsymbol{\theta}\,\boldsymbol{\phi} \begin{bmatrix} v_{xglr} \\ v_{yglr} \\ v_{zglr} \end{bmatrix} \tag{B.38}$$

where

$$\begin{bmatrix} v_{xglr} \\ v_{yglr} \\ v_{zglr} \end{bmatrix} = \begin{bmatrix} v_{xulr} \\ v_{yulr} \\ v_{zulr} \end{bmatrix} + \begin{bmatrix} \omega_x \\ \omega_y \\ \omega_z \end{bmatrix} \times \begin{bmatrix} 0 \\ 0 \\ -r_{lr} \end{bmatrix} \tag{B.39}$$

Substituting Eq. B.39 into Eq. B.38, after some manipulation Eq. B.40 and Eq. B.41 can be derived.

$$v_{x'glr} = \cos\,\theta\,(v_{xulr} - \omega_y r_{lr}) + \sin\,\theta\,(v_{zulr}\cos\,\phi + \sin\,\phi\,(v_{yulr} + \omega_x r_{lr})) \tag{B.40}$$

$$v_{y'glr} = \cos\,\phi\,(v_{ulr} + \omega_x r_{lr}) - v_{zulr}\sin\,\phi \tag{B.41}$$

Finally, the instantaneous tire radius, r_{lr}, used in Eq. B.39, in the fixed-body frame $(x,\ y,\ z)$ can be calculated as

$$r_{lr} = r_0 - \frac{x_{tlr}}{\cos\,\theta\cos\,\phi} \tag{B.42}$$

and the instantaneous strut length, l_{slr} in Eq. B.33 and Eq. B.34 is

$$l_{slr} = l_{sif} - (x_{slr} - x_{sir}) \tag{B.43}$$

where the initial length of the strut is

$$l_{sir} = h - (r_0 - x_{tir}) \tag{B.44}$$

B.2.3 Transmitted Moments to the Sprung Mass

In this subsection, it is assumed that the vehicle has the independent suspension with parallel horizontal links in the front and the rear axles. Therefore, the front and the rear roll centres are located in the ground plane. Moreover, it is assumed that these centres are fixed. Since the roll centres are located in the ground plane, all the jacking forces, $F_{dzlr},\ F_{dzrr},\ F_{dzlf}$ and F_{dzrf}, are equal to zero.

The total roll moment, M_{xlr}, transmitted to the left rear strut of the vehicle depends directly on the height of the rear axle roll centre. The reason is that the roll centre is, in fact, the instantaneous point in which the lateral forces developed by the tires are transmitted to the sprung mass.

$$\begin{aligned} M_{xlr} = \ & F_{yglr}\,(l_{slr} \ + \ r_{lr}) \\ & - \ (m_{ulr} g \sin \ \phi \ \cos \ \theta \ + \ m_{ulr}\dot{v}_{yulr} \ - \ m_{ulr}\omega_x v_{zulr} \ + \ m_{ulr}\omega_z v_{xulr})\, l_{slr} \end{aligned} \tag{B.45}$$

The second parenthesis in Eq. B.45 is the force that is applied to the unsprung mass at the left rear corner of the vehicle (see Eq. B.13 to Eq. B.15); therefore, Eq. B.45 can be simplified as

$$M_{xlr} \ = \ F_{ygslr} r_{lr} \ + \ F_{yslr} l_{slr} \tag{B.46}$$

The moments M_{ylr} and M_{zlr} transmitted to the left rear strut are

$$M_{ylr} = -F_{xgslr}\left(l_{slr} + r_{lr}\right) +$$

$$\left(-m_{ulr}g\sin\theta + m_{ulr}\dot{v}_{xulr} - m_{ulr}\omega_z v_{yulr} + m_{ulr}\omega_y v_{zulr}\right) l_{slr}$$

$$= -F_{xgslr}\left(l_{slr} + r_{lr}\right) + \left(F_{xgslr} - F_{xslr}\right) l_{lr} \tag{B.47}$$

$$= -\left(F_{xgslr}r_{lr} + F_{xslr}l_{lr}\right)$$

and

$$M_{zlr} = 0 \tag{B.48}$$

B.2.4 Tire Lift-off Consideration

When the tire lifts off the ground, the tire deflection, x_{tlr}, becomes negative. Therefore, whenever $x_{tlr} < 0$ the tire forces $F_{x'glr}$, $F_{y'glr}$, and $F_{z'glr}$ must set to zero and the instantaneous tire radius must be set to the value of r_0.

Bibliography

[1] NHTSA. Initiative to address he mitigation of vehicle rollover. National Highway Traffic Safety Administration, June 2003. http://www.nhtsa.gov.

[2] J.N. Kanianthra. Advanced technologies: The pathway to total safety. Advanced Safety Technolgies of the Near Future International Technical Conference on the Enhanced Safety of Vehicles, 2003.

[3] G. J. Forkenbrock and W.R. Garrott. Vehicle dynamic rollover propensity. National Highway Traffic Safety Administration, August 2013. http://www.nhtsa.gov/Research/Vehicle+Dynamic+Rollover+Propensity.

[4] R.C. Gonzalez, S.S. Orstavik, J.J. Huke, D.S. Boormhead, and J. Stark. Scaling and interleaving of subsystem lyapunov exponents for spatio-temporal systems. *Chaos*, 9(2):466–482, 1999.

[5] T. Shim and C. Ghike. Understanding the limitations of different vehicle models for roll dynamics studies. *Vehicle System Dynamics*, 45(3):191–216, 2007.

[6] M. Abe and W. Manning. *Vehicle Handling Dynamics Theory and Application*. ELSEVIER, Great Britain, 2009.

[7] T. D. Gillespie. *Fundamental of Vehicle Dynamics*. Society of Automotive Engineers, Inc., United State of America, 1992.

[8] Types of rollovers. `http://www.safercar.gov/Vehicle+Shoppers/Rollover/Types+of+Rollovers`. Accessed: 2013-08-29.

[9] L. Segel. Theoretical prediction and experimental substantiation of the response of the automobile to steering control. *Proceedings of the Institution of Mechanical Engineers: Automobile Division*, 10(1):310–330, 1956.

[10] H.B. Pacejka. *Tire and Vehicle Dynamics*. Society of Automotive Engineering, Warrendale, PA, 2002.

[11] M. Abe. *Vehicle Handling Dynamics: Theory and Application*. Theory and Application Series. Elsevier Science, 2009.

[12] J. Gertsch and T. Shim. Interpolation of roll plane stability models. *International Journal of Vehicle Design*, 46(1):72–93, 2008.

[13] B.C. Chen and H. Peng. Rollover warning for articulated heavy vehicles based on a time-to-rollover metric. *Journal of Dynamic Systems, Measurement, and Control*, 127(3):406–414, 2004.

[14] N. Zhang, G.M. Dong, and H.P. Du. Investigation into untripped rollover of light vehicles in the modified fishhook and the sine maneuvers. part i: Vehicle modelling, roll and yaw instability. *Vehicle System Dynamics*, 46(4):271–293, 2008.

[15] H. Imine, A. Benallegue, T. Madani, and S. Srairi. Rollover risk prediction of an instrumented heavy vehicle using high order sliding mode observer. In *Robotics and Automation, 2009. ICRA '09. IEEE International Conference on*, pages 64–69, May 2009.

[16] J. Yoon and K. Yi. A rollover mitigation control scheme based on rollover index. In *American Control Conference, 2006*, pages 6 pp.–, June 2006.

[17] J. Kim. Identification of lateral tyre force dynamics using an extended kalman filter from experimental road test data. *Control Engineering Practice*, 17(3):357 – 367, 2009.

[18] T. Shim, D. Toomey, C. Ghike, and M. H. Sardar. Vehicle rollover recovery using active steering/wheel torque control. *International Journal of Vehicle Design*, 46(1):51 – 71, 2008.

[19] E. Buckingham. On physically similar systems; illustrations of the use of dimensional equations. *Phys. Rev.*, 4:345–376, Oct 1914.

[20] M. Sampei, T. Tamura, T. Kobayashi, and N. Shibui. Arbitrary path tracking control of articulated vehicles using nonlinear control theory. *Control Systems Technology, IEEE Transactions on*, 3(1):125–131, Mar 1995.

[21] N. Matsumoto and M. Tomizuka. Vehicle lateral velocity and yaw rate control with two independent control inputs. In *American Control Conference, 1990*, pages 1868–1875, May 1990.

[22] S. Brennan and A. Alleyne. The illinois roadway simulator: a mechatronic

testbed for vehicle dynamics and control. *Mechatronics, IEEE/ASME Transactions on*, 5(4):349–359, Dec 2000.

[23] J. O'Brien, R.T., J.A. Piepmeier, P.C. Hoblet, S.R. Burns, and C.E. George. Scale-model vehicle analysis using an off-the-shelf scale-model testing apparatus. In *American Control Conference, 2004. Proceedings of the 2004*, volume 4, pages 3387–3392 vol.4, June 2004.

[24] W.E. Travis, R.J. Whitehead, D.M. Bevly, and G.T. Flowers. Using scaled vehicles to investigate the influence of various properties on rollover propensity. In *American Control Conference, 2004. Proceedings of the 2004*, volume 4, pages 3381–3386 vol.4, 2004.

[25] R. Verma, D. Del Vecchio, and H.K. Fathy. Development of a scaled vehicle with longitudinal dynamics of an hmmwv for an its testbed. *Mechatronics, IEEE/ASME Transactions on*, 13(1):46–57, 2008.

[26] G. Phanomchoeng and R. Rajamani. New rollover index for detection of tripped and un-tripped rollovers. In *Decision and Control and European Control Conference (CDC-ECC), 2011 50th IEEE Conference on*, pages 7440–7445, 2011.

[27] J.J.E. Slotin and W. Li. *Applied Nonlinear Control*. Prentice Hall International Inc., Upper Saddle River, NJ, 1991.

[28] H.K. Khalil. *Nonlinear Systems*. Prentice Hall, 2002.

[29] V.I. Oseledec. A multiplicative ergodic theorem: Lyapunov characteristic numbers for dynamical system. *Trans. Moscow Math. Soc.*, 19:127–231, 1968.

[30] A. Wolf, J.B. Swift, L.H. Swinney, and J.A. Vastano. Determining lyapunov exponents from a time series. *Physica*, pages 285–317, 1985.

[31] K.T. Alligood, T.D. Saure, and J.K. Yorke. *Chaos, an Introduction to Dynamical Systems*. Springer, New York, 1997.

[32] C. Yang and Q. Wu. On stability analysis via lyapunov exponents calculated from a time series using nonlinear mappingâa case study. *Nonlinear Dynamics*, 59:239–257, 2010.

[33] K. Ramasubramanian and M. S. Sriram. A comparative study of computation of lyapunov spectra with different algorithms. *Phys. D*, 139(1-2):72–86, May 2000.

[34] Q. Wu, N. Sepehri, P. Sekhavat, and S. Peles. On design of continuous lyapunov's feedback control. *Journal of the Franklin Institute*, 342(6):702 – 723, 2005.

[35] P. Sekhavat, N. Sepehri, and Q. Wu. Impact control in hydraulic actuators with friction: theory and experiments. *IFAC Journal of Control Engineering Practice*, 14(12):1423–1433, 2006.

[36] L.M. Pecora and T.L. Carroll. Synchronization in chaotic systems. *Physical Review Letters*, 64(8):821–825, 1990.

[37] R.V. Mendes. Conditional exponents, entropies and a measure of dynamical self-organization. *Physics letter A*, 248:167–171, 1998.

[38] Y.E. Ko and C.K. Song. Vehicle modeling with nonlinear tires for vehicle stability analysis. *International Journal of Automotive Technology*, 11(3):339–344, 2010.

[39] J.I. Hernandez and C.Y. Kuo. Lateral control of higher order nonlinear vehicle model in emergency maneuvers using absolute positioning gps and magnetic markers. *Vehicular Technology, IEEE Transactions on*, 53(2):372–384, 2004.

[40] Y. E. Ko and J. M. Lee. Estimation of the stability region of a vehicle in plane motion using a topological approach. *International Journal of Vehicle Design*, 30(3):181–192, 2002.

[41] R. Genesio, M. Tartaglia, and A. Vicino. On the estimation of asymptotic stability regions: State of the art and new proposals. *Automatic Control, IEEE Transactions on*, 30(8):747–755, 1985.

[42] S. Inagaki, I. Kushiro, and M. Yamamoto. Analysis on vehicle stability in critical cornering using phase-plane method. *JSAE Review*, 16(2):216–216, 1995.

[43] J. Samsundar and J. Huston. Estimating lateral stability region of a nonlinear 2 degree-of-freedom vehicle. In *International Congress and Exposition, Detroit, Michigan, United States*, SAE Technical Paper Series, pages 1791–1797. Society of Automotive Engineers, February 1998. SAE 981172.

[44] D.B. Johnson and J.C. Huston. Estimating lateral stability region of a nonlinear 2 degree-of-freedom vehicle. In *International Off-Highway and Powerplant Congress and Exposition, Milwaukee, Wisconsin*, SAE Technical Paper Series, pages 798–805. Society of Automotive Engineers, September 1984. SAE 841057.

[45] G.M. Dong, N. Zhang, and H.P. Du. Investigation into untripped rollover of light vehicles in the modified fishhook and the sine manoeuvres, part ii: effects

of vehicle inertia property, suspension and tyre characteristics. *Vehicle System Dynamics*, 49(6):949–968, 2011.

[46] S. Shen, J. Wang, P. Shi, and G. Premier. Nonlinear dynamics and stability analysis of vehicle plane motions. *Vehicle System Dynamics*, 45(1):15–35, 2007.

[47] Z. Liu, G. Payre, and P. Bourassa. Nonlinear oscillations and chaotic motions in a road vehicle system with driver steering control. *Nonlinear Dynamics*, 9(3):281–304, 1996.

[48] H. Haken. At least one lyapunov exponent vanishes if the trajectory of an attractor does not contain a fixed point. *Physics Letters A*, 94(2):71 – 72, 1983.

[49] M. Kunze. *Non-smooth Dynamical Systems*. Springer, Berlin, 2000.

[50] X. Zeng, R. A. Pielke, and R. Eykholt. Extracting lyapunov exponents from short time series of low precision. *Modern Physics Letters B*, 6:55–75, 1992.

[51] I. Shimada and T. Nagashima. A numerical approach to ergodic problem of dissipative dynamical systems. *Progress of Theoretical Physics*, 61(6):1605–1616, 1979.

[52] D. Ruelle. Ergodic theory of differentiable dynamical systems. *Publications Math. IHES*, 50(1):27–58, 1979.

[53] G. Benettin, L. Galgani, A. Giorgilli, and J.M. Strelcyn. Lyapunov characteristic exponents for smooth dynamical systems and for hamiltonian systems; a method for computing all of them. part 1: Theory. *Meccanica*, 15:9–20, 1980.

[54] V.I. Bogachev. *Measure Theory*. Springer, Berlin, 2007.

[55] L.S. Young. Ergodic theory of differentiable dynamical systems. In *Real and Complex Dynamical Systems*, volume 464 of *NATO ASI Series*, pages 293–336. Springer, 1995.

[56] T. Eisner, B. Farkas, M. Haase, and R. Nagel. Operator theoretic aspects of ergodic theory. *Graduate Texts in Mathematics, Springer, to appear*, 2013.

[57] J.P. Eckmann and D. Ruelle. Ergodic theory of chaos and strange attractors. *Rev. Mod. Phys.*, 57:617–656, Jul 1985.

[58] D. Ruelle. *Chaotic evolution and strange attractors*. Cambridge University Press, Cambridge, 1989.

[59] I. P. Cornfeld, S. V. Fomin, and Ya. G. Sinai. *Ergodic Theory*. Springer-Verlag Berlin Heidelberg New York, New York, 1982.

[60] J.Y. Wong. *Theory of ground vehicles*. John Wiley and Sons, Inc., Hoboken, NJ, 2008.

[61] D.E. Smith and J.M. Starkey. Effects of model complexity on the performance of automated vehicle steering controllers: Model development, validation and comparison. *Vehicle System Dynamics*, 24(2):163–181, 1995.

[62] S. Sadri and C.Q. Wu. Modified lyapunov exponent, new measure of dynamics. *Nonlinear Dynamics*, 78(4):2731–2750, 2014.

[63] S. Sadri and C.Q. Wu. Lateral stability analysis of on-road vehicles using lyapunov's direct method. In *Intelligent Vehicles Symposium (IV), 2012 IEEE*, pages 821–826, June 2012.

[64] S. Sadri and C.Q. Wu. Lateral stability analysis of on-road vehicles using the concept of lyapunov exponents. In *Intelligent Vehicles Symposium (IV), 2012 IEEE*, pages 450–455, June 2012.

[65] S. Sadri and C. Wu. Stability analysis of a nonlinear vehicle model in plane motion using the concept of lyapunov exponents. *Vehicle System Dynamics*, 51(6):906–924, 2013.

[66] H. Nusse and J.A. York. *Dynamics: Numerical Explorations*. Springer, New York, 1998.

[67] S. Sadri and C. Wu. Lyapunov stability analysis of a new nonlinear 4-dof vehicle roll model. Manuscript submitted for publication, 2015.

[68] Msc software. `http://www.mscsoftware.com/product/adamscar`. Accessed: 2014-11-26.

[69] P. White, R. Maryniuk, S. Sadri, and C.Q. Wu. Scale experimental test vehicle for rollover study. In *25th Canadian Congress of Applied Mechanics*, May-June 2015.

[70] H. Giahi. Analysis the steel structure of baja 5b model. Technical report, 2014.

[71] R. Maryniuk. Vehicle parameter identification and speed controller design for baja 5b flux. Technical report, 2014.

[72] P. White. Baja 5b flux mobile laboratory. Technical report, 2014.

[73] N. Das, B. Suresh, and J. Wambold. Estimation of dynamic rollover threshold of commercial vehicles using low speed experimental data. *SAE*, (932949), 1993.

[74] D. Hyun and R. Langari. Modeling to predict rollover threat of tractor-semitrailers. *Vehicle System Dynamics*, 39(6):401–414, 2003.

[75] A. Hac. Rollover stability index including effects of suspension design. *SAE Technical Papers*, (2002-01-0965), 2002.

[76] A. Hac, T. Brown, and J. Martens. Detection of vehicle rollover. *SAE Technical Papers*, (2004-01-1757), 2004.

[77] J. Bernard, J. Shannan, and M. Vanderploeg. Vehicle rollover on smooth surfaces. *SAE Technical Papers*, (891991), 1989.

[78] J. C. Dixon. *Tire, suspension and handling.* Society of Automotive Engineers, Inc., Warrandale, PA, 1996.

[79] NHTSA. The National Highway Traffic Safety Administration's Rating System for Rollover Resistance An Assessment. Special report 265, National Highway Traffic Safety Administration, 2002.

[80] *A Policy on Geometry of Highways and Streets, 6th Edition.* American Association of State Highway and Transportation Officials, 2011.

[81] D. C. Karnopp, D. L. Margolis, and Rosenberg R. C. *System Dynamics Modeling and Simulation of Mechatronic Systems.* John Wiley and Sons, Inc., New York, 2000.